2012-03-27

Electric Field Sensing in a Railgun Using Slab Coupled Optical Fiber Sensors

Jonathan Robert Noren
Brigham Young University - Provo

Electric Field Sensing in a Railgun Using

Slab Coupled Optical Fiber Sensors

Jonathan Robert Noren

A thesis submitted to the faculty of
Brigham Young University

in partial fulfillment of the requirements for the degree of

Master of Science

Stephen M. Schultz, Chair
Richard H. Selfridge
Aaron R. Hawkins

Department of Electrical Engineering

Brigham Young University

June 2012

ABSTRACT

Electric Field Sensing in a Railgun using
Slab Coupled Optical Fiber Sensors

Jonathan Noren
Department of Electrical Engineering, BYU
Master of Science

This thesis discusses the application of Slab Coupled Optical Fiber Sensors (SCOS) in a railgun. The specific goal of these sensors is to create an electric field profile at a specific point in the gun as the armature passes. The thesis explores the theory that powers the railgun as well as the principles of the SCOS sensors. It also elaborates on the various noise sources found throughout the detection system and concludes with a summary of the various field tests that were performed throughout this project.

There are many benefits to using a railgun over traditional weapons in the field. These benefits not only include both safety and cost, but also greater overall defense capabilities. Unfortunately, the velocity skin effect (VSE) causes the current railgun designs to have limited life span through wear on the rails. In order to develop superior railguns and railgun armatures, the accurate detection of the VSE through measuring the electric field is of great interest. We used a SCOS, a small directionally precise dielectric sensor, as a small sensing area is required to be able to measure the electric fields inside of the rail gun.

The actual usage of the SCOS within the railgun produced an additional set of problems that are not commonly encountered in the lab. The chief amongst these was noise from strain, RF pickup, and phase noise. This thesis also reports various methods used to reduce each of these noise sources.

Keywords: optics, fiber optics, optical fiber sensors, slab coupled optical sensors, SCOS, electric field sensors, railgun

ACKNOWLEDGMENTS

Much work, time, dedication, perseverance, and expense has gone into reaching the conclusion of my research graduate work and the completion of my thesis.

I would like to specially thank my graduate committee whose advice, support and encouragement have been fundamental to the progress in my research. I would like to acknowledge Dr. Schultz and Dr. Selfridge who have spent many hours discussing, critiquing and expanding my ideas and projects, helping me to become a better scientist, researcher and engineer. Additionally, I am grateful for my association with the other BYU students in the Optics Lab.

I greatly appreciate the support of my family. They have encouraged me to peruse higher learning, and they have instilled within me the desire to work diligently and to have the faith to expect success. They have been a great example of the joy that comes from hard work and perseverance.

I would like to thank my fiancée who has been very supportive of my graduate studies. She has shown genuine interest in my work, and has been proud of my efforts. Her support and encouragement has made my graduate studies worthwhile and enjoyable.

Finally, my research would not have been possible without the support of our funders including IPITEK who has invested both time and money in my projects and KVH who has donated the D-fiber used extensively throughout the lab. GA Tech and GTRI have also both been invaluable in this research by making the resources available to actually test on a railgun. BYU itself has provided a great work and academic environment to foster creativity and aid the learning and engineering process.

TABLE OF CONTENTS

1 Introduction 1

1.1 Contributions 1

1.2 Thesis Outline 2

2 Railgun Background 5

2.1 Purpose & Motivation 5

2.2 Electromagnetic Principles 6

2.3 Form and Shape 11

2.4 Railgun Complications 14

2.5 Summary 18

3 SCOS Background 19

3.1 General Concept 19

3.2 The Physics of SCOS 20

3.3 Slab Materials 24

4 Signal Measurements 27

4.1 SCOS Signal 27

4.2 Theoretical Limit 31

4.2.1 Shot Noise 31

4.2.2 Thermal Noise 32

4.2.3 Detection Limit 33

4.3 Other Noise Sources 34

4.3.1 Laser Noise 35

4.3.2 Fiber Noise 36

4.3.3 SCOS Noise 37

4.3.4 Phase Noise 40
4.4 Noise Reduction & Compensation 41
4.4.1 Laser Noise 41
4.4.2 Phase Noise 41
4.4.3 Strain Noise 42
4.5 Actual Measurement Limit 43
5 Railgun Testing 47
5.1 GA Tech Setup 47
5.2 Test Chronology 53
5.2.1 February 2010 53
5.2.2 January 2011 55
5.2.3 May 2011 56
5.2.4 August 2011 58
5.2.5 December 2011 61
5.2.6 January 2012 64
5.3 Accomplishments 66
5.3.1 Oscilloscope Data Capture 66
5.3.2 SCOS Packaging 68
5.3.3 SCOS Calibration 70
5.3.4 SCOS Data Mining 73
6 Conclusion 77
6.1 Contributions 77
6.1.1 Noise Characterization 77
6.1.2 Oscilloscope Capture 78
6.1.3 SCOS Packaging and Mounting 78

6.1.4 SCOS Calibration 78
6.1.5 SCOS Data Mining 79
6.2 Future Work 79
6.2.1 X-Cut SCOS 79
6.2.2 SCOS Cartridges 79
6.2.3 Calibration 80
6.2.4 Data Mining 80
REFERENCES 81
Appendix A. Railgun Simulation, Matlab Code 83
Appendix B Wavelength AutoCalibration Manual 85
B.1 Setup & First Use 85
B.2 Panels Description 88
B.2.1. Graphs Panel 88
B.2.1. Laser Panel 90
B.2.3. Sample Panel 92
B.2.3. Analysis Panel 94
Appendix C. E-Field MappIng, Matlab Code 97
C.1 Plot Formatted Data 97
C.2 Armature Analysis 102
C.3 SCOS Voltage Calibration 104
C.4 Data Filter and Loading 106
C.5 B-Dot Data Loader 111
C.6 Parse Shot Information 112
C.7 Parse Microsoft Excel File 115

LIST OF TABLES

Table 1: Measurement parameters 34

LIST OF FIGURES

Figure 2-1: A time-lapse shot of a projectile launched by the NSWC Railgun at Dahlgren, VA [5] 6

Figure 2-2: A side view of the railgun without insulators, including the fields and current. 7

Figure 2-3: Cross-section of the wires used in the simplified analysis....8

Figure 2-4: Railgun current with a capacitance of $8mF$, inductance of $77\mu H$, resistance of $100m\Omega$, and charging voltage of $5.1kV$. 9

Figure 2-5: Railgun power supply schematic 10

Figure 2-6: A simplified simulation of the current supplied to a railgun. 11

Figure 2-7: A simplified illustration of the cross section of the GA Tech railgun. 12

Figure 2-8: A side view of the railgun without the insulators. 13

Figure 2-9: A picture of the NSWC Railgun at Dahlgren, VA (left) [5] and the railgun at GA Tech [5]. 14

Figure 2-10: A before (left) and after (right) picture of an armature. (Notice the missing section of the leg.)....15

Figure 2-11: The wear on two copper rails after 8 consecutive shots at $4.3kV$ in the GA Tech railgun. 15

Figure 2-12: A comparison of the expected electric fields in the $\hat{z}$ (rail to rail) and $\hat{x}$ (launch direction) directions [9]....17

Figure 2-13: The remains of the steel bar backing used for one of the sensors....18

Figure 3-1: A SCOS compared to a standard ¼ watt resistor. 20

Figure 3-2: An end view of a D-fiber (left) and a cross-sectional profile illustration of the D-fiber (right)....21

Figure 3-3: An illustration of the side profile of a SCOS that consists of a nonlinear optical crystal placed atop the etched region of a D-fiber. 21

Figure 3-4: The spectral response of SCOS with a broadband source. 22

Figure 4-1: A graph of the transmission coefficient of a SCOS 27

Figure 4-2: A block diagram of a simple detection system with the theoretical signal level at each point. 28

Figure 4-3: The source signal (top) applied to a SCOS and the resulting SCOS signal (bottom)....30

Figure 4-4: A simplified schematic of a transimpedance amplifier.....33

Figure 4-5: A block diagram of a simple detection system with numbered noise sources.....35

Figure 4-6: Illustrates the mode dependence of the SCOS spectral response.....36

Figure 4-7: The setup (a) and results (b) of an experiment showing temperature effects on the SCOS [1].....38

Figure 4-8: A graph that compares the effects of strain on a SCOS and a FBG. 39

Figure 4-9: An illustration of phase noise on a fiber. The fiber is flicked at time T=0. 40

Figure 4-10: The recorded signal from a 10% laser tap during a railgun shot. 42

Figure 4-11: A suspension mounted SCOS in an FR4 cartridge. 43

Figure 4-12: SCOS calibration signal (top), the noise deviation (middle), and the reference e-field (bottom). 43

Figure 5-1: A picture of the railgun room at GA Tech. 48

Figure 5-2: Lab personnel changing the rags between shots. 48

Figure 5-3: The interface between the capacitor bank and the gun rails. 49

Figure 5-4: Two of the three capacitor banks (a) that power the railgun and single capacitor (b). 50

Figure 5-5: An insulator with a SCOS and one of its fiber leads secured in the bottom containment half.....51

Figure 5-6: A completed sensor setup that is ready for the upper containment half to be placed atop. 51

Figure 5-7: A picture of the secured rail containment unit. 52

Figure 5-8: The room where the measurement electronics are kept. 53

Figure 5-9: A sensor glued into the back of an insulator. 54

Figure 5-10: A sample of shot data. (Green: w/o filter; Red: filtered DC-7MHz; Blue: filtered 10kHz-7MHz) 55

Figure 5-11: A SCOS sensor placed inside of an insulator using foam. 55

Figure 5-12: Data sample collected from the January 2010 trip. 56

Figure 5-13: A plot showing both the simulated and detected field (note that they appear to be inverted). 58

Figure 5-14: The results of a FBG mounted on FR4 placed surround with foam. 59

Figure 5-15: The calibration data for one of the SCOS sensors. 60

Figure 5-16: A captured, filtered SCOS plot with the electric filed calibration displayed. 61

Figure 5-17: A SCOS inside of a three sided cartridge. 62

Figure 5-18: The results of two FBGs hard mounted and suspended in a cartridge. 63

Figure 5-19: The spectral content of the same FBGs hard mounted in the gun using a suspension cartridge. 64

Figure 5-20: A dual sensor mounted into a rail for testing. 64

Figure 5-21: A plot of the SCOS (blue) and the normalized FBG (magenta) and laser source (red). 65

Figure 5-22: A current DC block with a corner frequency of approximately 100Hz. 68

Figure 5-23: Simulated frequency response of the DC block. 68

Figure 5-24: A pair of electrodes used for calibrating SCOS. 71

Figure 5-25: The front panel of the automatic calibrator displaying the results of a scan of a SCOS. 72

Figure 5-26: Three plots of the same shot using different filters to retrieve data. 74

Figure 5-27: SCOS response with useful information about the armature times and field strengths. 75

Figure B-1: A setup diagram for the auto calibration program 85

Figure B-2: The graphs panel of the auto-calibrator after a successful calibration. 86

Figure B-3: A screenshot of the graphs panel. 88

Figure B-4: A screenshot of the laser panel. 90

Figure B-5: A screenshot of the sample panel. 92

Figure B-6: A screenshot of the analysis panel. 94

Figure C-1: An example Excel file describing the B-Dot setup and times for use with the MATLAB program 111

Figure C-2: An example Excel file the plotting program expects to see detailing the shot information.....114

1 INTRODUCTION

There are several sensing applications in which a small dielectric sensor is the most appropriate sensor. These applications typically occur in environments where there is either an extremely high electric field, which would interfere with a metallic sensor, or where the metallic sensor itself would interfere with the desired field in an unacceptable manner. A Slab Coupled Optical Sensor (SCOS) is one such dielectric sensor that is formed by placing an appropriately sensitive crystal on an optical fiber. A SCOS is not only completely dielectric but it also has an advantage over typical sensors as the fiber is impervious to outside electrical and optical interference and it is extremely small (about the size of a ¼ watt resistor) The SCOS has been shown to work effectively in both controlled lab conditions and in static environments [1]. However, when the SCOS is used in dynamic environments, such as the inside of a rail gun, mechanical noise from the environment combined with noise inherent in the interrogation system swamps the desired signal preventing accurate measurements.

1.1 Contributions

My principle contributions have been in the application of SCOS sensing to railgun testing, and understanding and overcoming the challenges associated with that.

- Transition from ESA to oscilloscope data collection
- A greater understanding of noise sources within the SCOS system.
- Packaging SCOS into railgun

    - Fiber routing out of containment
    - Cartridges for sensor replacement and moving
    - Effects of packaging changes
- Field calibration of polymer SCOS
    - Labview wavelength tuning
    - Applied field to railgun, oscilloscope capture, calibration data
- Data filtering
    - Low pass filtering at 100 kHz to block electronic noise
    - RF pickup reduction

1.2 Thesis Outline

This thesis is organized into four main chapters that cover topics ranging from railgun operation to the use of SCOS to detect electric fields in the railgun.

Chapter 2 discusses the purpose and motivation behind the railgun project. It also details railgun operation on a physical level as well as the various shapes and forms it takes. Additionally, this chapter explores the problems facing the railgun project, the motivation behind the desire to detect the electric fields within the gun, and the requirements on the sensors that are to go inside the gun.

Chapter 3 summarizes one approach to a solution, SCOS, to the sensing problems discussed in Chapter 2. This chapter also explains how the SCOS operates as well as the different kinds of SCOS that are available.

Chapter 4 covers in greater detail how the SCOS can be used to sense electric fields. It also contains an important derivation of the theoretical limits on the sensing abilities of the

SCOS. It concludes with a discussion of the principle noise sources that have and are now currently inhibiting our ability to reach the theoretical detection limit.

Chapter 5 examines the application of the SCOS to the railgun. Specifically, it recounts the current railgun setup at Georgia Institute of Technology (GA Tech), and how the sensors are inserted and calibrated. Additionally, Chapter 5 contains a chronology of all of the tests that we have been performed at GA Tech over the past two years. This chronology covers the accomplishments and improvements learned or discovered at each test.

2 RAILGUN BACKGROUND

2.1 Purpose & Motivation

The principles of electromagnetic propulsion that power a railgun have several militaristic and scientific applications that make perfecting the railgun appealing. Scientific applications include using a specially shaped railgun to slow or even stop a beam of paramagnetic atoms for study. Additionally, railgun technologies are being adapted to launch probes and satellites into space, as well as to slow and stop other materials acting as magnetic breaks [2]. Militaristic applications, however, are a bit more prominent due to funding and potential applications. Currently, the major thrust of railgun research targets placing a railgun on large electrically driven naval warships.

As a military weapon, the rail gun has many advantages over traditional missile and projectile based weaponry. The most obvious of all the advantages is the ability of the railgun to achieve higher velocities than is achievable by chemical guns and rockets. Additionally, there is greater control of the launch process and higher firing efficiency [3]. The railgun has the ability to accelerate and launch projectiles at hypersonic velocities of up to Mach 10 for multi-kilogram loads. With enough energy, projectiles can be launched over 200 nautical miles at considerably lower cost than comparable short-range missiles [4]. Figure 2-1 contains a few frames from a high speed camera showing a view of the projectile as it is fired from the railgun at Dahlgren, VA.

Figure 2-1: A time-lapse shot of a projectile launched by the NSWC Railgun at Dahlgren, VA [5]

The lack of projectile propellant leads to overall greater safety for ship personnel due to decreased risk of secondary explosions in the event that a stock of projectiles is hit with enemy fire. The use of the inert projectiles also reduces the need for propellant production, storage, loading, and transport, which can lead to both reduced costs and reduced personnel requirements aboard ships. The projectiles fired from a railgun are not only without propellant, but they are also smaller than regular missiles. This allows for an increased magazine capacity for the gun and an overall greater carrying capacity for the ship—thousands of rounds can replace tens of missiles [6]. Lastly, it has no shell extraction requirements and therefore has the prospect for faster firing rates than more traditional projectile weapons [4].

2.2 Electromagnetic Principles

Figure 2-2 shows that a railgun is a simple circuit that consists of two conducting rails with an armature that connects the two rails together along with a source of direct current. The current travels along one rail, across the armature, and then down the second rail. The current traveling through the rails creates a magnetic field. This induced magnetic field then creates a force on the armature described by the Lorentz force equation.

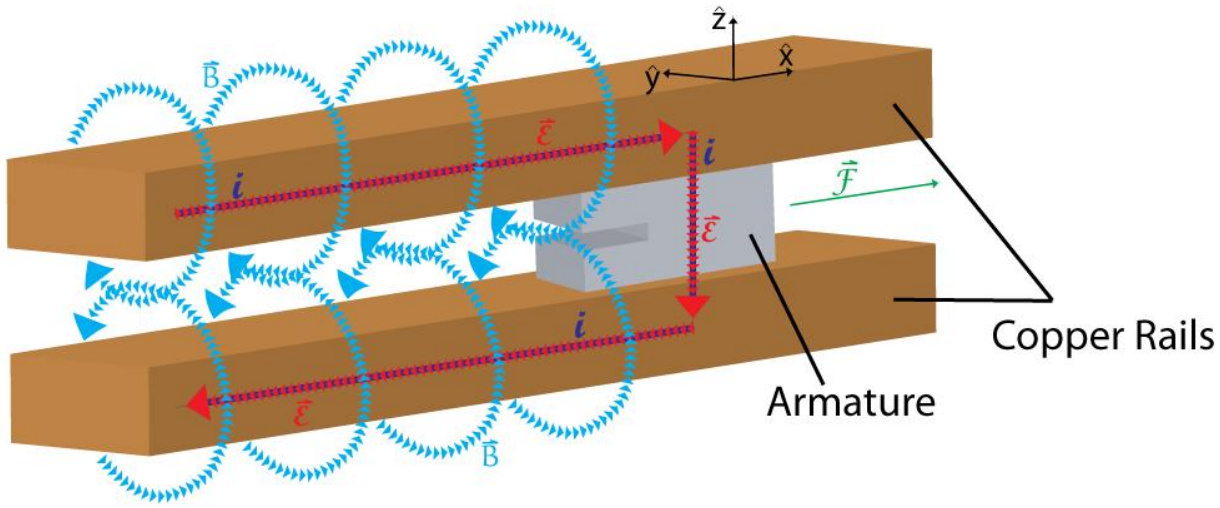

Figure 2-2: A side view of the railgun without insulators, including the fields and current.

For a simplified analysis of the force on the armature, it is appropriate to model the rails as infinitely long wires. The current traveling down a semi-infinite long wire creates a magnetic flux density given by

$$\vec{B}(r) = \frac{\mu_0 I}{2\pi r}\hat{\phi}, \qquad [2\text{-}1]$$

where I is the total current in the wire, μ_0 is the permeability of air, and r is the distance from the wire. The current is traveling in opposite directions in the rails (represented by the wires) resulting in an addition of the magnetic flux density in the region between the wires. Figure 2-3 shows that the amplitude of the magnetic flux density between the wires which is given by

$$\vec{B}(r) = \frac{\mu_0 I}{2\pi}\left(\frac{1}{x} + \frac{1}{d-x}\right), \qquad [2\text{-}2]$$

where d is the separation of the rails, and x is the distance from the center of one of the wires.

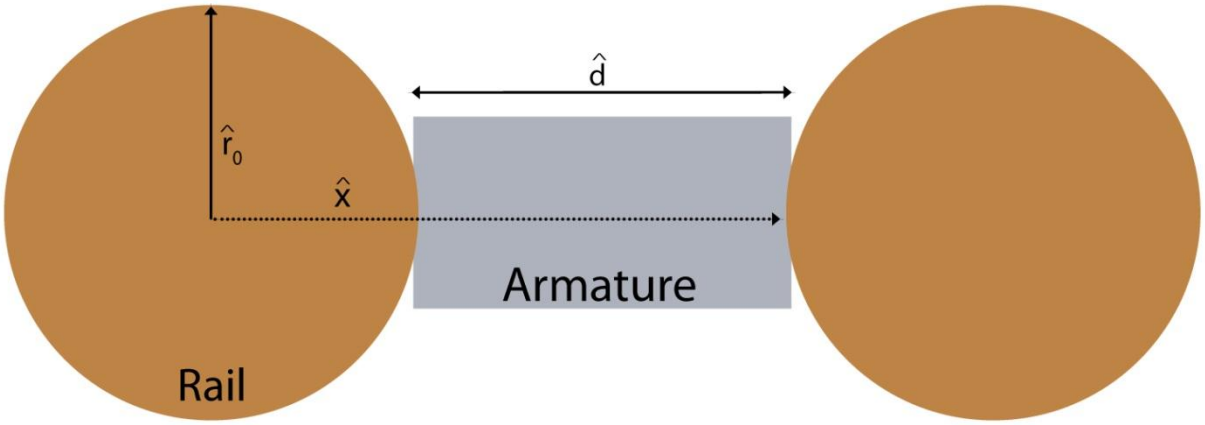

Figure 2-3: Cross-section of the wires used in the simplified analysis.

The armature is also modeled as a wire that connects the two infinitely long wires together. The force on the wire is given by

$$\vec{F} = IdB. \qquad [2\text{-}3]$$

The average force on the armature is calculated by integrating the force between the two rails as given by

$$\vec{F}_{\text{av}} = \frac{1}{d}\int_{r_0}^{d+r_0} \frac{\mu_0 I}{4\pi}\left(\frac{1}{x} + \frac{1}{d+2r_0-x}\right) Id\ dx, \qquad [2\text{-}4]$$

resulting in

$$\vec{F}_{\text{av}} = \frac{\mu_0 I^2}{4\pi}\ln\left(\frac{d+r_0}{r_0}\right). \qquad [2\text{-}5]$$

When we take into account the actual rail geometry, the average force can be fit to

$$\vec{F}_{\text{av}} = \frac{1}{2}L'I^2, \qquad [2\text{-}6]$$

where L' is the inductance per unit length of the rails.

The approximate velocity of the armature can then be calculated from the force as given by

$$v = \int_0^{t_0} \frac{1}{2m}L'I^2\ dt. \qquad [2\text{-}7]$$

The DC current is typically supplied by a capacitor bank. However, the total impedance of the rails and armature is typically very small (on the order of $m\Omega$). With just a capacitor discharged into the railgun, the current supply would be too high and the discharge rate would be too fast. For example, if a railgun has a total capacitance of C=8mF and a resistance of 10 $m\Omega$, then the maximum current would be $9MA$ and the discharge time would be 80 μs.

In order to produce a more steady current supply, an inductor is added into the supply. However, with the small resistance of the rails, the supply becomes an underdamped RLC circuit that will oscillate resulting in inefficient energy delivery to the armature. Figure 2-4, generated by the MATLAB code given in Appendix A, shows a representative discharge curve.

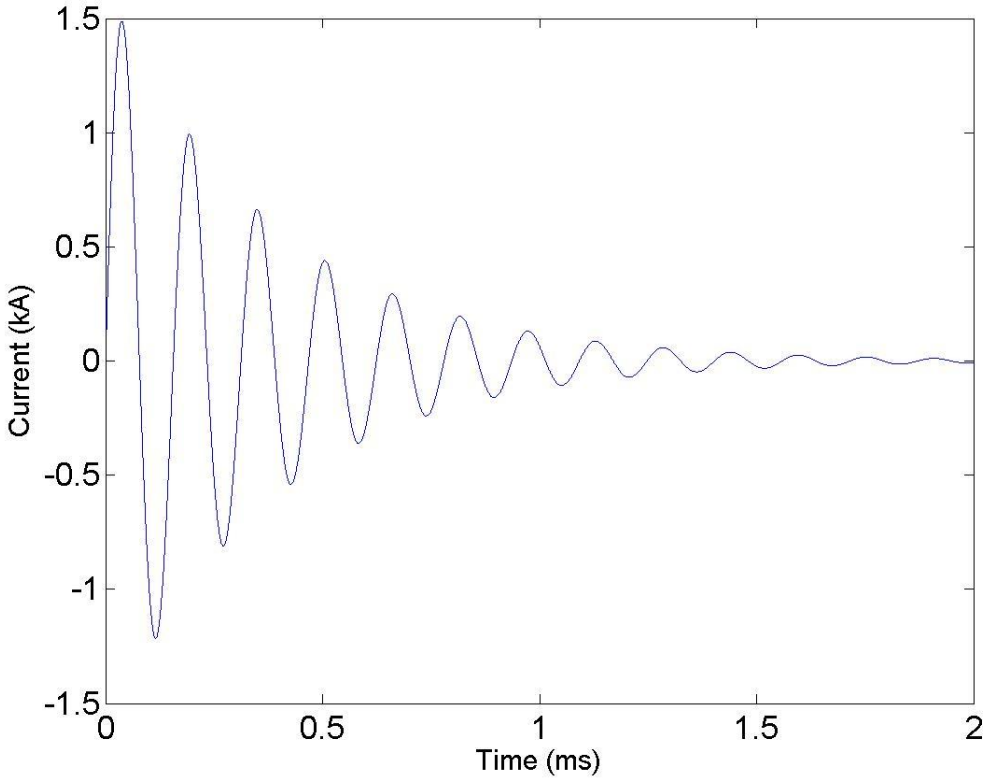

Figure 2-4: Railgun current with a capacitance of 8mF, inductance of 77μH, resistance of 100$m\Omega$, and charging voltage of 5.1kV.

This oscillation in the current supply will produce an inefficient system with a high chance of power supply failure. The current oscillations in the supply are eliminated by adding a high power diode into the circuit. The power supply is further divided into banks that can be fired at different times in order to produce a smoother current supply. Figure 2-5 shows a schematic of a railgun power supply.

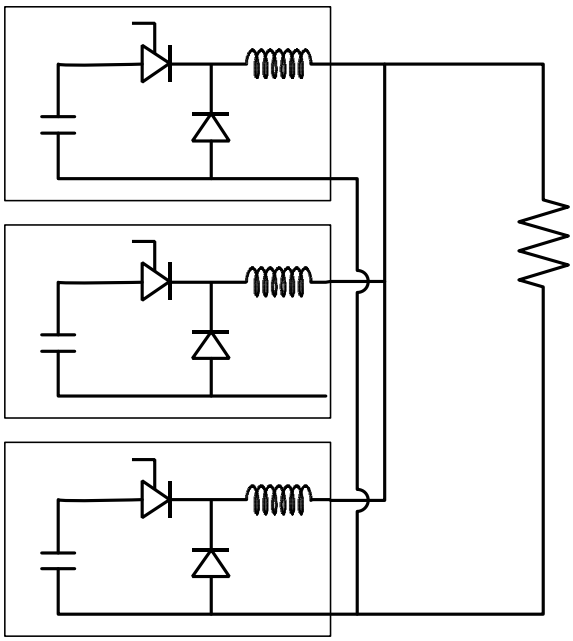

Figure 2-5: Railgun power supply schematic

When the switch is closed, the capacitor supplies current to the railgun. However, the current is limited by the inductor. When all of the energy stored in the capacitor is transferred to the inductor, then the diode switches to its 'on' state, essentially removing the capacitor from the circuit. The inductor then supplies the current to the railgun. When the diode switches 'on' the circuit becomes an RL circuit rather than an RLC circuit.

Figure 2-6 shows a simplified simulation of the current supplied to the railgun. Notice how the supply produces a ramp-up in the current supplied. The limited change in the current

supply is caused by the inductor. The figure below illustrates how the voltage across the capacitor, which starts high, discharges and creates a current. The current ramps up, and, if it were not for the diode, it would begin to oscillate with the voltage. However, when the voltage across the capacitor is smaller than the turn-on voltage of the diode, the current is discharged into the railgun with a time constant of $\tau = R/L$.

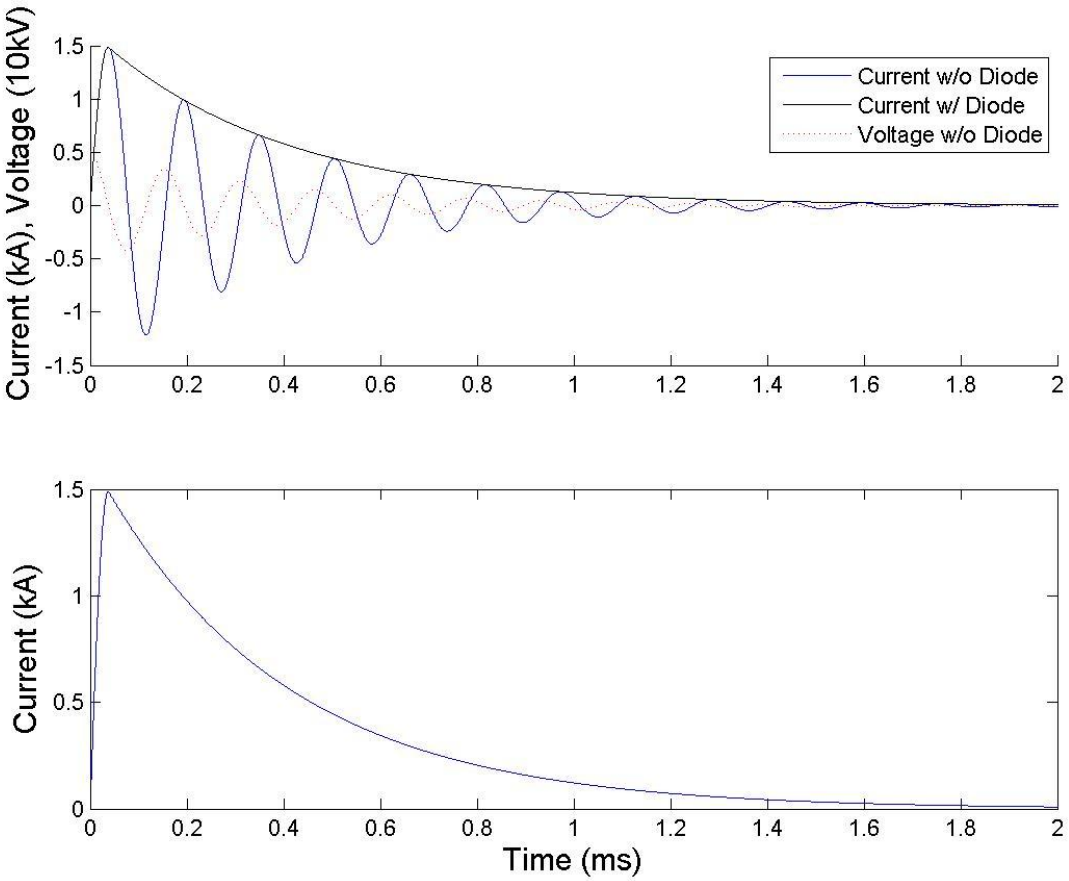

Figure 2-6: A simplified simulation of the current supplied to a railgun.

2.3 Form and Shape

While there are many shapes that a railgun can take, they all have several things in common. The primary components of the railgun are two conducting rails. Typically, these rails

are made of copper due to its conductivity and current carrying capacity. The rails are held apart from each other by insulating pieces.

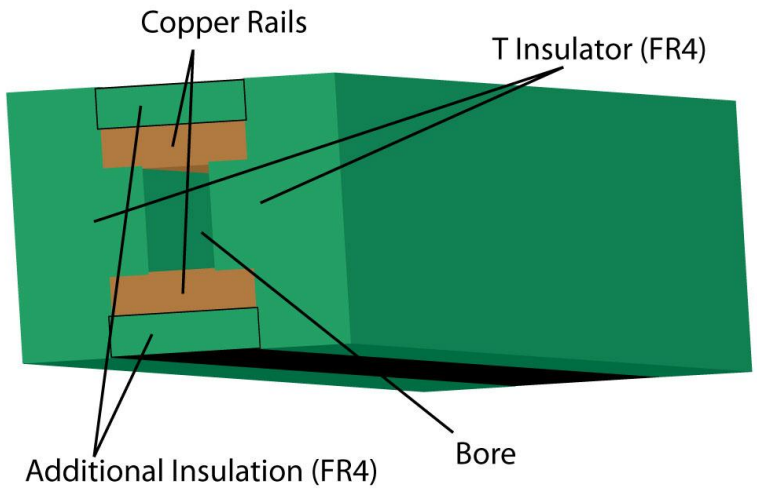

Figure 2-7: A simplified illustration of the cross section of the GA Tech railgun.

Figure 2-7 illustrates a cross section of a railgun. The insulating pieces are typically made of FR4 and in the case of a railgun with a rectangular bore are shaped like a 'T'. The distance between the two rails is equal to the size of the armature, illustrated by Figure 2-8, and is kept even for the entire length of the gun.

There are almost as many designs for containment as there are railguns currently in production. The containment of the railgun consists of everything on the railgun with the exception of the rails themselves and the firing system and is typically[1] the only portion of the railgun visible when completely assembled. One of the key design requirements when creating a containment unit for a railgun is the bore radial stiffness. A high stiffness prevents the radial

[1] At least one railgun has been assembled with a windowed side panel where the rails and armature are visible during the firing process [22].

displacement of the bore, which in turn, determines the firing accuracy of the railgun and contributes to extending the life of the gun [7].

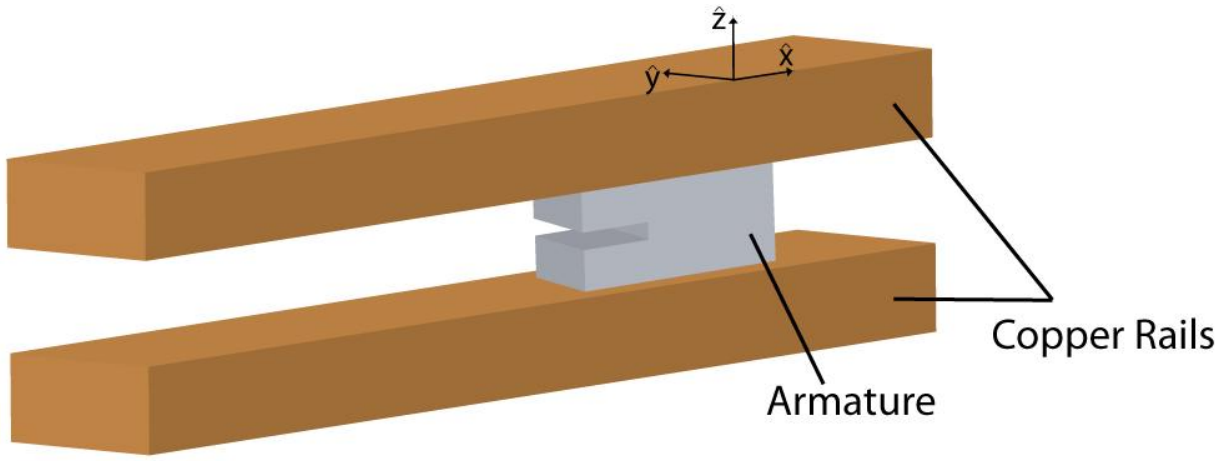

Figure 2-8: A side view of the railgun without the insulators.

The Figure 2-9 shows a picture of the railgun at Dahlgren and a picture of the railgun at the GA Tech. They both have a similar two layer design for containment, which provide sufficient bore radial stiffness. Directly surrounding the rails are insulators made out of FR4 as illustrated in Figure 2-7. These insulators surround the rails and prevent the arcing of electricity to the outer containment layer, which is shaped like a clamshell around the insulators. The outer clamshell is composed of a series of vertical plates of laminated steel. Steel is used to provide the strength requirements to stiffen the bore. The steel is laminated to decrease its effect on the electric fields produced by the gun. The clamshell is then held in place with a sequence of heavy duty bolts, which secure the components during firing.

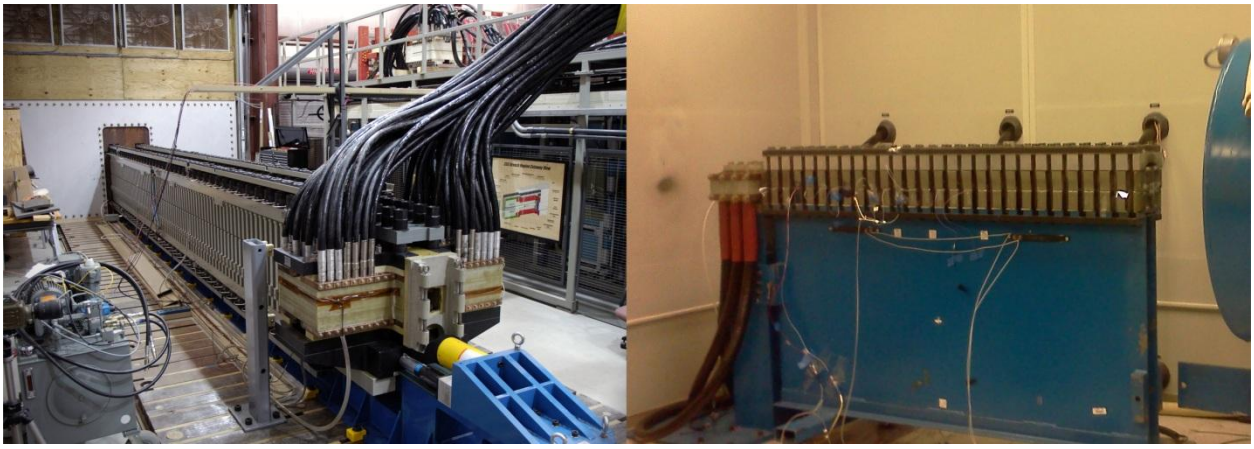

Figure 2-9: A picture of the NSWC Railgun at Dahlgren, VA (left) [5] and the railgun at GA Tech [5].

2.4 Railgun Complications

Despite the many advances in railgun development and application, actual field deployment of a railgun is still unattainable due to limitations in reusability. Each railgun, especially those which can obtain hypersonic velocities, has a limited number of shots that it can handle before the gun needs to be disassembled so that inner rails and insulators may be replaced. As the railgun is fired and the projectile is accelerated down the rails, the armature erodes and otherwise deforms the rail and insulators surfaces. The exact causes of this deformation are not fully understood, but are thought to be caused by frictional and resistive heating which causes melting and plasma erosion [4].

The frictional and resistive heating is primarily attributed to the concentration of current in the rails near the armature. This current concentration is known as the velocity skin effect (VSE) and has been observed in moving conductors. The VSE causes the majority of current to flow through the rear portion of the armature. This not only causes a non-uniform distribution of pressures over the armature from the electromagnetic forces, but it also causes the rear of the armature to heat up more rapidly than the front [8]. These two effects combined can cause the

deformation of the armature as it travels along the rails. Figure 2-10 shows a picture of an armature before and after being shot out of the railgun.

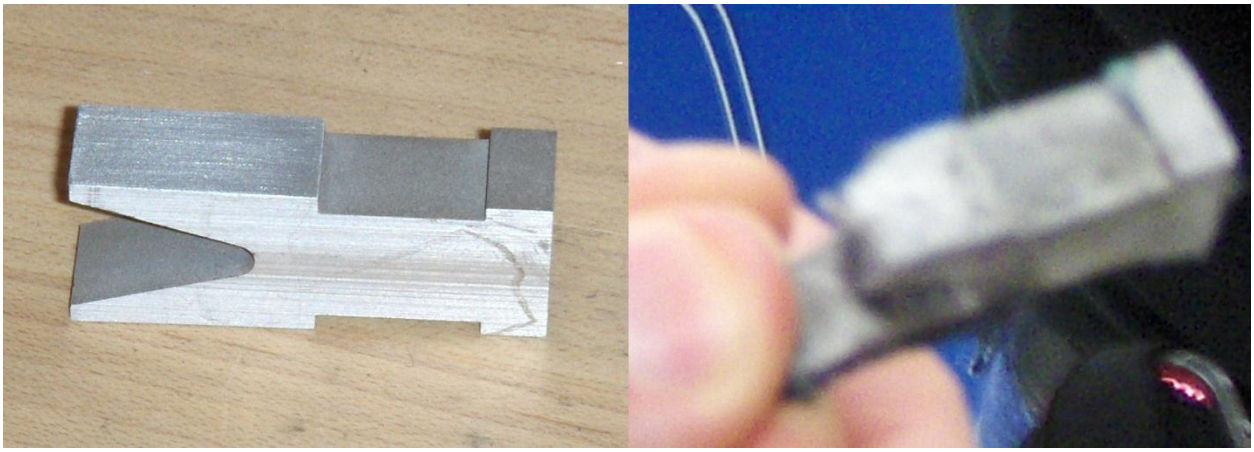

Figure 2-10: A before (left) and after (right) picture of an armature. (Notice the missing section of the leg.)

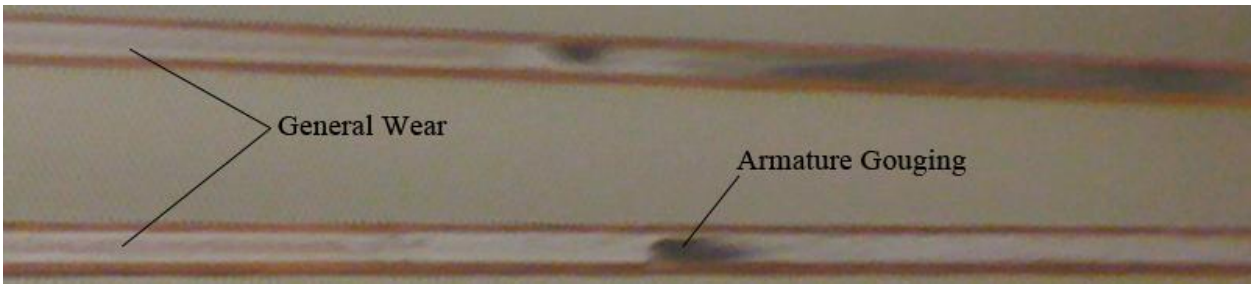

Figure 2-11: The wear on two copper rails after 8 consecutive shots at 4.3*kV* in the GA Tech railgun.

The armature is not the only portion of the system that suffers due to the VSE. In fact, if the only problem was armature deformation, the deformation would be immaterial as each test requires a new armature and deformations in the armature are unimportant after it leaves the gun. The more significant concern is that, due to the VSE through the armature, the rails themselves become damaged. Figure 2-11 shows the wear on two rails after 8 consecutive shots in the GA Tech railgun. The gouging in the rails by the armature is a critical problem that can progress to

the point where the armature is unable to pass that point, effectively jamming the gun. If the rails are not replaced, the containment of the gun could also be compromised.

A greater understanding of the actual VSE is necessary to be able to design a set of rails and an armature that will be immune to its effects. In order to characterize the VSE, a method to measure the current density rather than the voltage or total current is required. In order to measure the current density, we rely on Ohm's law as given by

$$\vec{J} = \sigma \vec{E}, \qquad [2\text{-}8]$$

where $\vec{J}$ is the current density at the surface of the conductor, σ is the conductivity of the conductor and $\vec{E}$ is the resulting electric field in the conductor. Since the electric field is tangential to the rail boundary, the electric field will be continuous across the boundary. Therefore, by measuring the electric field in the direction of the current flow, we can calculate an estimate of the current density.

Figure 2-12 shows computer estimation of the field magnitudes in the direction of the current flow on the rail ($\hat{x}$ field) and from rail to rail ($\hat{z}$ field) with respect to distance from the armature. Of particular note in this estimation is the order of magnitude difference in the $\hat{z}$ field and the x field. The $\hat{z}$ field is more than one order of magnitude higher than the $\hat{x}$ field, which makes it that much easier to detect. Given a bore width of $14mm$, the magnitude of the $\hat{z}$ electric field is approximately $8\frac{kV}{m}$ and the magnitude of the $\hat{x}$ electric field is $0.5\frac{kV}{m}$.

The railgun presents a unique challenge when trying to accurately measure the electric fields with the intent of determining the VSE. Two additional things are of particular note in Figure 2-12. First, the $\hat{x}$ field and the $\hat{z}$ field are significantly different in shape, which necessitates the use of a sensor that is able to distinguish between directions because on the $\hat{x}$ field is relevant when trying to measure the VSE. Second, both $\hat{x}$ and $\hat{z}$ fields vary greatly over a

relatively small distances. Therefore, sensor requirements include the need to have a small sensing area so that electric field can be recorded with a high resolution and placement as close as possible to the armature as it is being fired.

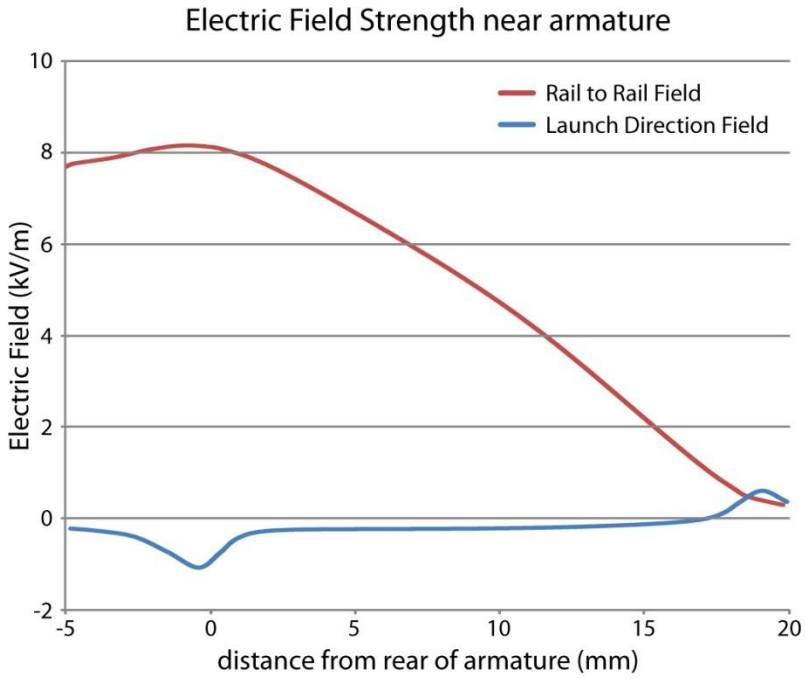

Figure 2-12: A comparison of the expected electric fields in the $\hat{z}$ (rail to rail) and $\hat{x}$ (launch direction) directions [9].

Due to the extreme conditions within the bore of the gun, a sensor cannot be placed within the inner layer of the containment if it is not dielectric. Figure 2-13 shows the results of a sensor that used a metal bar to steady itself within the insulator. The steel bar originally started inside the insulator as part of sensor. The steel bar was designed to minimize the stress on the sensor. During one of the shots the steel bar was pulled out of the insulator and shot partially down gun, destroying the sensor.

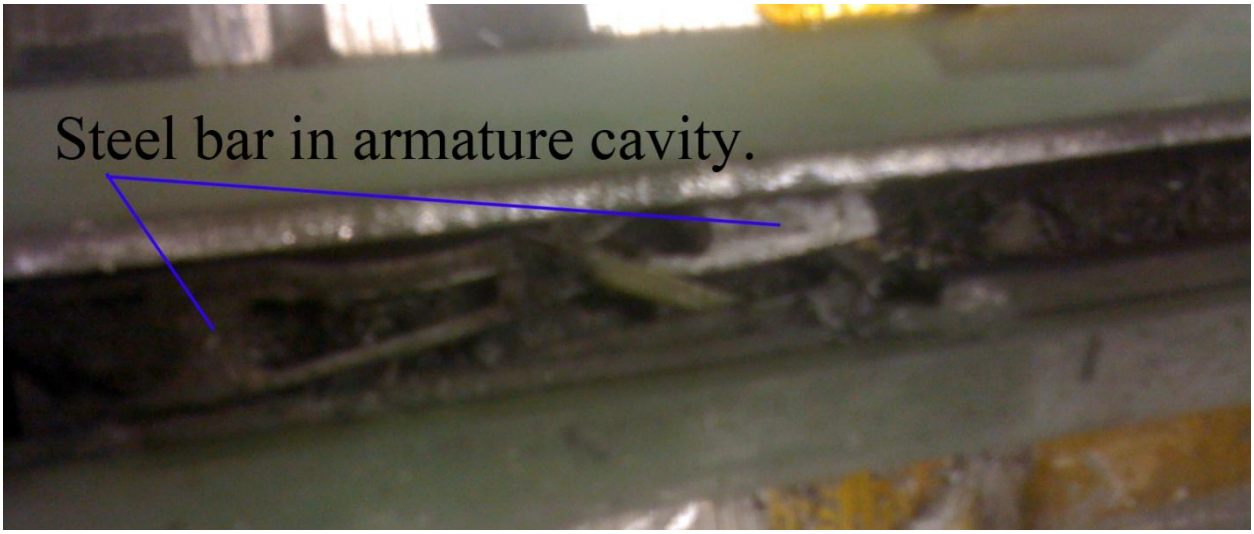

Figure 2-13: The remains of the steel bar backing used for one of the sensors.

2.5 Summary

There are many benefits to using a railgun over traditional weapons in the field. The benefits not only include both safety and cost, but greater overall defense capabilities. Unfortunately, the VSE causes the current railguns to have a limited life span due to wear on the rails. In order to develop better railguns and railgun armatures, the accurate detection of the VSE through measurement of the electric field is of paramount importance. Unfortunately, for many reasons, existing sensors are unsuitable for this application. For these same reasons, a small directionally precise dielectric sensor with a small sensing area is required to be able to measure the electric fields inside of the rail gun. Therefore, the application of the Slab Coupled Optical fiber Sensor (SCOS) to the railgun testing is the primary focus of my thesis.

3 SCOS BACKGROUND

3.1 General Concept

The general goal when creating a new sensor system is to create a system that is both non-intrusive and accurate. The actual definition of non-intrusive varies from application to application; however, in most applications, non-intrusive does not refer to the actual size of the sensor but to the idea that it does not interfere or change the subject of interrogation. There are a variety of applications that require this particular definition of nonintrusive sensor systems [10] [11] [12] [13] [14]. In particular, when the subject of interrogation is an electric field there are several applications that require a compact sensor that does not perturb the field. The solution to this problem lies in creating a sensor that is completely dielectric.

The need for a compact dielectric electric field sensor stems from several applications, such as the railgun, where there is a small localized electric field and where it is undesirable for the sensor to interact with the field in any way. In the case of the railgun, a non-dielectric sensor would not only be destroyed but also has the potential to cause harm to the gun itself. The rail gun also adds the additional requirement that the sensor be directional. In other words, the fields detected by the sensor lie along a single predictable axis. Typical electric field sensors, such as D-dots, while extremely sensitive, only detect the total electric field magnitude at a single point.

The sensor that we developed to meet these needs is a fiber based slab coupled optical sensor. The main advantages of a sensor being based on optical fiber is that it is not only

immune to outside electric and magnetic field interferences, but it will not cause electric or magnetic interference. The sensor involves attaching a nonlinear optical crystal to the surface of a D-shaped optical fiber and is simply referred to as a Slab Coupled Optical fiber Sensor (SCOS) [15] [16]. This sensor itself has dimensions of only $1.2mm$ X $0.2mm$ X $0.2mm$ and is routed to and from the subject of interrogation using optical fiber in order to minimize outside interference. The compact nature of this sensing element makes it nonintrusive (spatially) and enables localization of the measured field. Figure 3-1 shows a comparison between a SCOS and a standard ¼ watt resistor.

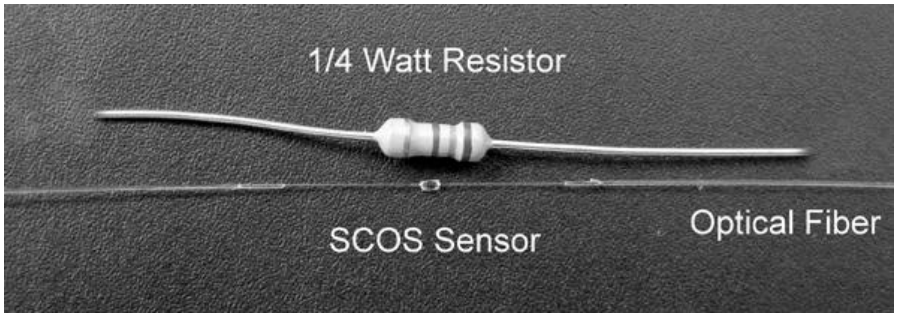

Figure 3-1: A SCOS compared to a standard ¼ watt resistor.

3.2 The Physics of SCOS

A SCOS can be modeled as two coupled waveguides that when combined give it the ability to act as a sensor: an electro-optic (EO) slab and a D-fiber. The EO slab is a material whose index of refraction changes in the presence of an electric field. Index of refraction changes vary depending on the material properties of the slab, as discussed in the Slab Materials section below. The D-fiber is simply a single mode polarization maintaining fiber that has a D shaped core as seen in Figure 3-2.

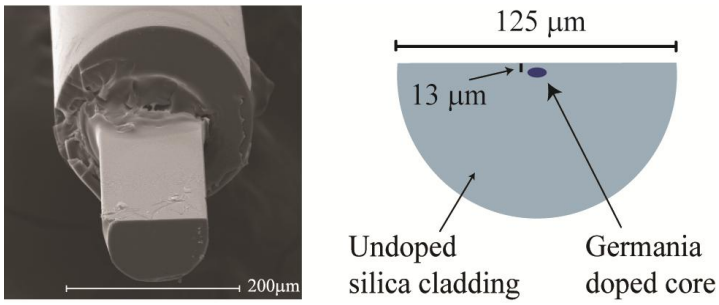

Figure 3-2: An end view of a D-fiber (left) and a cross-sectional profile illustration of the D-fiber (right).

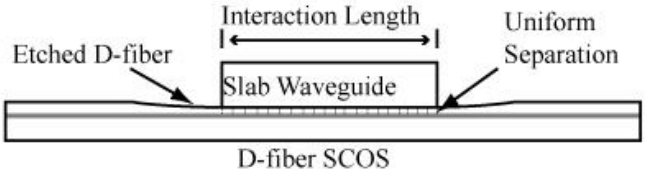

Figure 3-3: An illustration of the side profile of a SCOS that consists of a nonlinear optical crystal placed atop the etched region of a D-fiber.

The EO slab waveguide is placed on the D-fiber near the core, as illustrated in Figure 3-3, such that it lies within the evanescent field of the fiber. When the two waveguides are close enough that their evanescent fields overlap, the light in one waveguide may couple into the other.

The coupling of light from the fiber into the slab is not uniform across the optical spectrum. Instead, it occurs predictably at a several distinct frequencies called resonant dips when the effective index of a mode of the slab waveguide match the effective index of the D-fiber mode. A true and complete understanding of the mode coupling would require starting with Maxwell's equations for the system and using boundary conditions to determine the modal solutions. While this has been done, for simplicity, if weak coupling is assumed between the two waveguides, coupled-mode theory can be used to solve for the overlap location of the different modes. According to coupled-mode theory, it is assumed that only the amplitudes of the fields in

a waveguide are affected by the presence of another waveguide, and that mode coupling involves the scattering of light from the mode of one of the waveguides into the mode of the other, which accounts for the resonant dips [1].

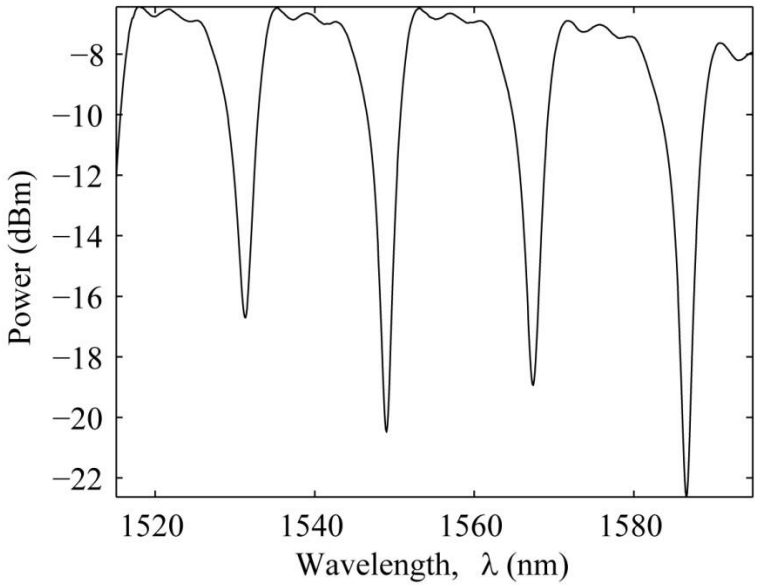

Figure 3-4: The spectral response of SCOS with a broadband source.

The resonant dips for a SCOS, which are caused by the constructive interference between the slab and the core of the fiber, are shown in Figure 3-4. The wavelength of the location of the resonant dips can be found to be [17] [18]

$$\lambda_m \cong \frac{2t}{m}\sqrt{\left(n_o^2 - n_{eff}^2\right)}, \qquad [3\text{-}1]$$

where t and n_0 are respectively the thickness and refractive index of the overlay material, n_{eff} is the effective index of the fiber mode, and m is the slab waveguide mode number. The distance

between the resonant dips is given by the free spectral range (FSR), which is conveniently approximated for higher order modes at a chosen wavelength as [1],

$$FSR \approx \frac{\lambda^2}{2t\sqrt{n_0^2 - n_{eff}^2}}. \quad [3\text{-}2]$$

Both of the previous equations are based on n_o, the refractive index of the slab. When the slab is placed in an electric field, its index of refraction will change proportionally to the electric field. The change in the index of refraction causes a shift in the resonance wavelengths. This shift in the resonance wavelengths is the foundation for the operation of the sensor. By detecting the size of the shift in the wavelength, as the slab is exposed to an electric field, the amplitude of the electric field can be measured.

The sensitivity of the sensor is directly correlated to the total change of the index of refraction, such that the greater the change of index of refraction correlates to a higher sensitivity. The total change in the index of refraction and subsequently the shift in the resonant wavelength, are proprieties of the EO slab material used to create the sensor. These factors combined create an equation that gives the transmission coefficient of a laser,

$$T = T_0 + \left(\frac{\Delta T}{\Delta \lambda}\right)\left(\frac{\Delta \lambda}{E}\right)E. \quad [3\text{-}3]$$

where T_0 is the DC power through the SCOS (measured), the term $\frac{\Delta T}{\Delta \lambda}$ represents the change in output power as a function of the shift in the wavelength, and the term $\frac{\Delta \lambda}{E}$ represents the shift in the wavelength as a function of the applied electric field E. Since these factors cannot truly be measured independently of each other, the equation is generally abbreviated by allowing ΔT to represent the total change in transmission through the SCOS as a function of electric field E as given by

$$T = T_0 + E(t)\Delta T. \quad [3\text{-}4]$$

3.3 Slab Materials

There are two distinct types of EO slabs that are used to make the SCOS fabricated for use in electric field sensing projects, polymer and potassium titanyl phosphate (KTP). The polymer has a higher EO coefficient and for this reason is used in the majority of cases. KTP, while it does have a weaker EO coefficient, is still used primarily when the direction of the field to be detected makes it difficult or impossible to use the polymer.

The polymer SCOS used for this research are made of 20/80 mix of AJL8 and amorphous polycarbonate (APC). These particular materials were chosen, designed, and synthesized at the University of Washington because of its high hyperpolarizability, which allows it to obtain large EO coefficients, on the order of ~100 pm/V [1]. The polymer is fabricated by spin coating a liquid polymer solution onto a smooth planar surface. The solution is then poled by inserting the resulting film between two electrodes in a nitrogen environment as the polymer is reheated to the glass transition temperature of the APC, while a large electric field (at least 100MV/m) is applied for at least 5 minutes [19].

There are several benefits of using a polymer slab. Benefits include the ability to vary the slab index and thickness through modifications to the fabrication process. Moreover, the polymer has high EO coefficients and a relatively low dielectric constant. Unfortunately, polymers also have two primary drawbacks which consist of thermal expansion [1], which causes resonance shifts, and, a limitation placed on the direction in poling due to physical constraints, such that poling can only be accomplished effectively in a direction that is normal to the surface of the polymer, which causes the direction of sensitivity of the polymer to be limited to the same direction.

The KTP SCOS refer to a single type of EO crystal which owes its EO properties to its crystal lattice. When in the presence of an electric field, the charges within the crystal lattice are redistributed in a non-uniform manner. This non-uniform change results in a slight physical deformation in the crystal lattice. This, in turn, translates to a change in the dielectric tensor and thus the index of refraction [1]. While there are several commercially available crystals which exhibit EO properties that could be used in the fabrication of SCOS devices, a combination of past research [1] and availability led to our selection of the KTP for use in this project. The KTP crystals with the desired thickness, crystal orientations and polish quality are purchased premade directly from the manufacturer. Compared to the polymer, the KTP crystals have the benefit of having a lower coefficient of thermal expansion, which results in more steady measurements because the spectrum shifts less with temperature. Additionally, the crystals can be cut to any desired orientation to allow a SCOS to measure electric fields oriented other than perpendicular to the face of the slab, which is the basis of multi-axis sensing [1].

4 SIGNAL MEASUREMENTS

4.1 SCOS Signal

As described in Chapter 3, the electric field can be measured by determining the location of the resonant dip, similar to the method often used with fiber Bragg grating interrogation. However, the frequency of the applied electric field is often too high for standard wavelength tracking systems. In addition, due to noise in the system, detection of very small wavelength shifts, which are typical of the SCOS, is difficult.

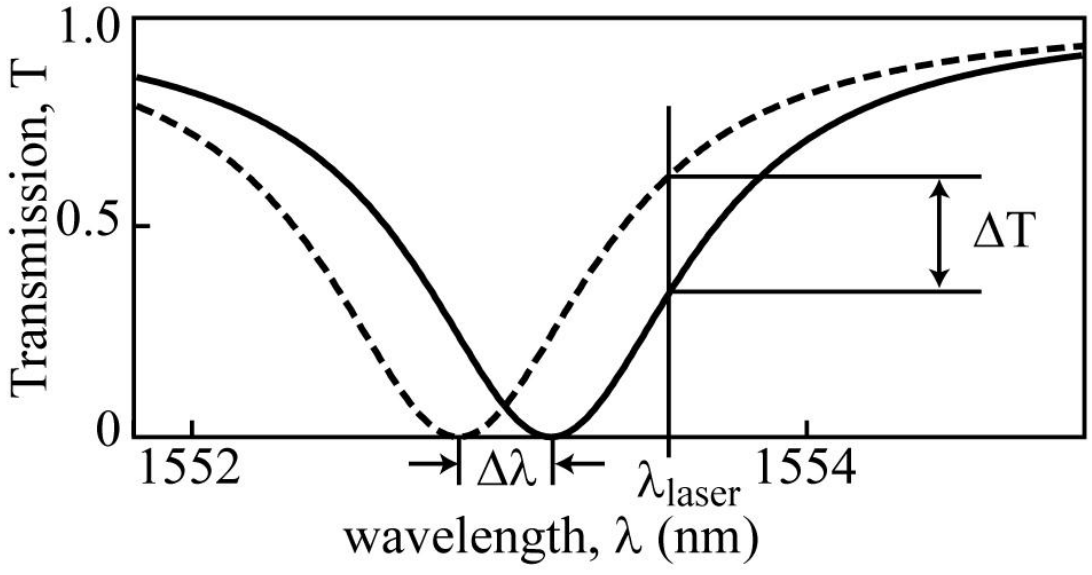

Figure 4-1: A graph of the transmission coefficient of a SCOS

Instead of tracking the wavelength dip, a detection system can be attained by coupling a laser into the optical fiber. The power transmitted through the SCOS is simply the incident laser power multiplied times the transmission coefficient of the SCOS. Figure 4-1 shows that by using a laser with a fixed wavelength that corresponds to the edge of a transmission dip, the shift in the resonant dip is converted into a change in the transmitted optical power.

Since the shift in the resonance is small for any practical electric field, the change in the transmission coefficient has a linear response as given by,

$$T_{scos}(t) = T_0 + E(t)\Delta T, \qquad [4\text{-}1]$$

where T_0 is the SCOS transmission with no applied electric field, $E(t)$ is the time varying applied electric field, and ΔT is the small signal approximation that depends on both the slope of the transmission dip and the amount of shift in the resonance with applied electric field.

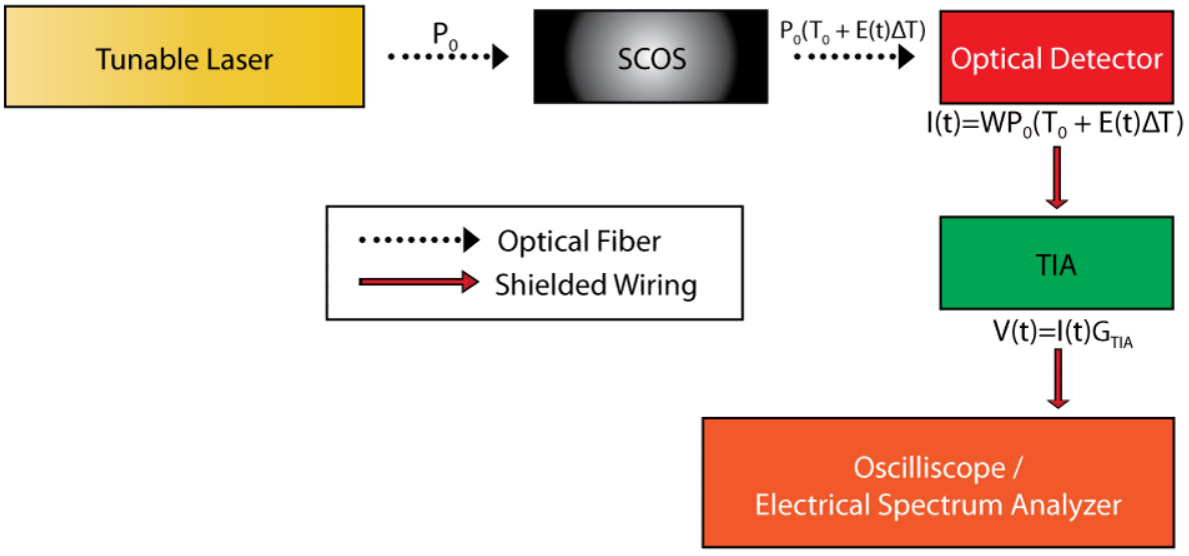

Figure 4-2: A block diagram of a simple detection system with the theoretical signal level at each point.

Figure 4-2 gives the block diagram of a basic SCOS detection system with the calculated signal strength without noise at each step. The laser is the first point in the system. It is tuned to a wavelength that corresponds to the side of a resonant dip as shown in Figure 4-1. The laser output is linearly polarized in the vertical, or TM, direction and has an output power of P_0 that is as stable as possible. The laser is coupled via optical fiber to the SCOS where the optical power is changed based on the transmission coefficient of the SCOS. The transmission coefficient, T_o, includes the transmission of the SCOS as well as any other transmission losses such as connector losses. The optical power after the SCOS is given by

$$P_{scos}(t) = P_0\, T_{SCOS} = P_0(T_0 + E(t)\Delta T). \quad [4\text{-}2]$$

The optical detector converts the optical signal to a current by a simple conversion ratio called the responsivity, W_{resp}, as given by

$$I(t) = W_{resp}P_0(T_0 + E(t)\Delta T). \quad [4\text{-}3]$$

It is converted into a voltage and amplified by terminating the optical detector with a transimpedance amplifier as described by

$$V(t) = G_{TIA}W_{resp}P_0(T_0 + E(t)\Delta T). \quad [4\text{-}4]$$

The final voltage signal can be divided into two parts (1) the DC portion, which does not depend on the electric field and (2) the AC portion. The DC portion of the signal is blocked, resulting in an overall expected voltage signal given by

$$V_{ac}(t) = G_{TIA}W_{resp}P_0E(t)\Delta T. \quad [4\text{-}5]$$

All of the components of $V_{ac}(t)$ are known parameters of the system except one, the sensitivity of the SCOS (ΔT), which has to be measured. In order to determine the sensitivity, ΔT, the SCOS is placed between two metal electrodes (the rails of the railgun) with a spacing of

$d = 14mm$. A sinusoidal voltage of amplitude $100V$ and frequency of approximately $8kHz$ is applied to the electrodes resulting in an applied electric field of $E(t) = 7.1\sin(2\pi\, 8 * 10^3 t\,)\frac{kV}{m}$.

Figure 4-3 shows the source signal (top) that is applied to the rails divided by 50, as well as the resulting signal (bottom) captured by the oscilloscope. For this measurement, vertically polarized (TM) light was coupled into the SCOS, and from the SCOS back into a photo-detector as illustrated by Figure 4-2.

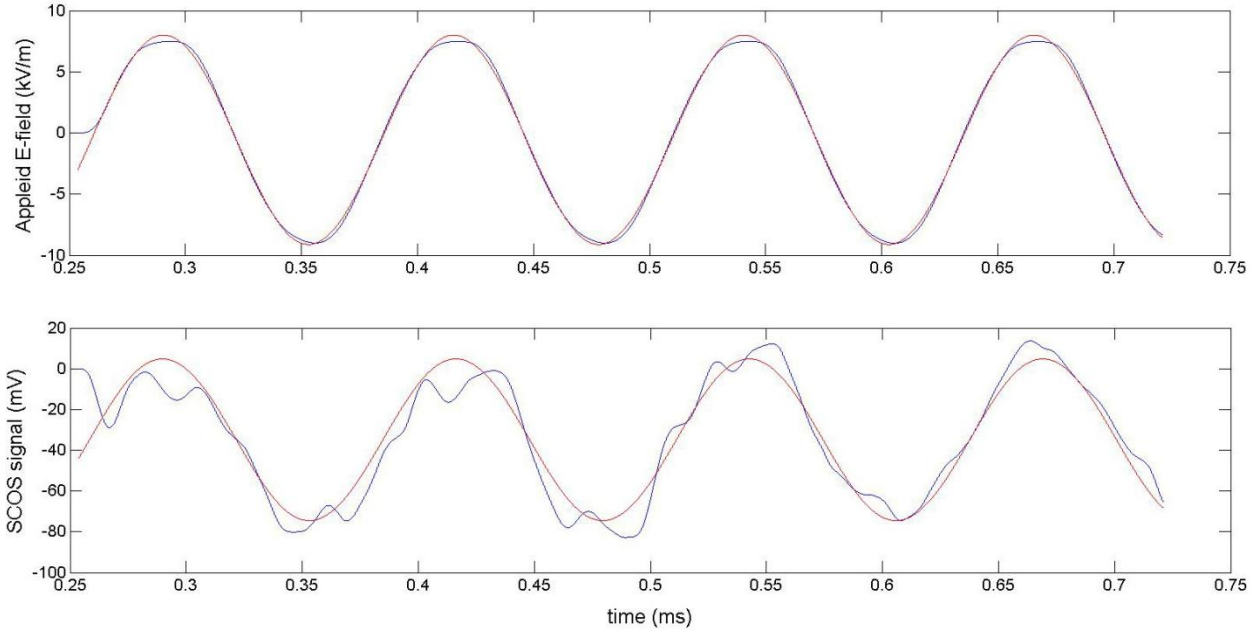

Figure 4-3: The source signal (top) applied to a SCOS and the resulting SCOS signal (bottom).

The power at the photo-detector was measured to have a magnitude of $218\mu W$. The optical detector had a responsivity of $1\ A/W$ and the total transimpedance gain was about $30dB$ or about $1000\ V/V$. From the oscilloscope, the final ac voltage amplitude was measured to be $80mV$. Using the measured characteristics, and equation for $V_{ac}(t)$ given above, the sensitivity

of the SCOS was found to be $\Delta T = 5.2 * 10^{-6} \frac{m}{V}$. The final SCOS signal using this configuration is thus given by

$$V_{ac}(t) = \left(1000 \frac{V}{A}\right)\left(1 \frac{A}{W}\right)(218\mu W)\left(5.2 * 10^{-6} \frac{m}{V}\right)\left(E \frac{V}{m}\right) \quad [4\text{-}6]$$

or

$$V_{ac}(t) = 1.1 * 10^{-3} E \frac{mV}{V/m}. \quad [4\text{-}7]$$

4.2 Theoretical Limit

There are many varying sources of noise in the SCOS system. More attention to those noise sources is provided in the following section. This section focuses on the two most common noise sources in optoelectronic systems, namely shot noise and thermal noise. The theoretical derivations of these noise sources in combination with the signal strength derivation are used to determine the theoretical sensing limit for the current SCOS sensors.

4.2.1 Shot Noise

The first electrical element encountered after the return fiber is the photodiode. The noise associated with the conversion of photons to electrons is called shot noise. Shot noise is caused by randomness of the quantized states of electrons and photons. The shot noise follows a Poisson distribution and is modeled by,

$$I_{sh} = \sqrt{2qW_{resp}P_0\Delta f}, \quad [4\text{-}8]$$

where P_0 is the total power received by the photodiode, q is the charge of an electron, W_{resp} is the responsivity of the photodiode, and Δf is the total bandwidth of the received signal. Given

an input of $P_0 = 218\mu W$, a diode responsivity of $W_{resp} = 1\frac{A}{W}$, and a bandwidth of $\Delta f = 99\ kHz$, the shot noise has a magnitude of $I_{sh} = 2.6\ nA$. The noise current can be converted into noise voltage by multiplying the shot noise current by the gain of the TIA resulting in $V_{sh} = 2.6\ \mu V$.

4.2.2 Thermal Noise

Thermal noise is inherent in any system that includes any type of resistance. Thermal noise is caused by the agitation due to temperature of the charge carriers in wires, traces, and resistors. While it is impossible to entirely eliminate thermal noise, by inspection of the models, it is clearly evident that the greater the resistance, the greater the voltage noise. Therefore, wires and traces will have negligible amounts of thermal noise.

The transimpedance amplifier is the next element after the photodiode. This is the first element in the signal path that includes a resistance of notable size. In general, when an amplifier of any kind is purchased, a noise figure is included in the datasheet of the amplifier. This noise figure includes a summation of all of the different noises inside the amplifier, including the thermal noise. In order to calculate the theoretic SNR limit we will use a simplified, ideal amplifier with a given resistance, as opposed to the noise figure included with the TIA. The voltage fluctuations in a resistor due to thermal noise is modeled using by,

$$V_{th} = \sqrt{4k_b T R \Delta f}, \qquad [4\text{-}9]$$

where k_b is the Boltzmann constant, T is the temperature of the resistor in Kelvin, R is the value of the resistance, and Δf is the bandwidth of the signal through the resistor.

Figure 4-4 models a simplified transimpedance amplifier using an ideal operational amplifier and a known resistance. Using the virtual short assumption, the gain of this amplifier

is equal to the resistance of the feedback path. In the field, we generally use a gain on the TIA of 1000, which would result in the theoretical resistor in the feedback loop being equal to $1k\Omega$. The bandwidth of the TIA used in tests is 99 kHz. Using this information, the thermal noise, when the system as at room temperature ($300°K$), is $V_{th} = 1.3\mu V$.

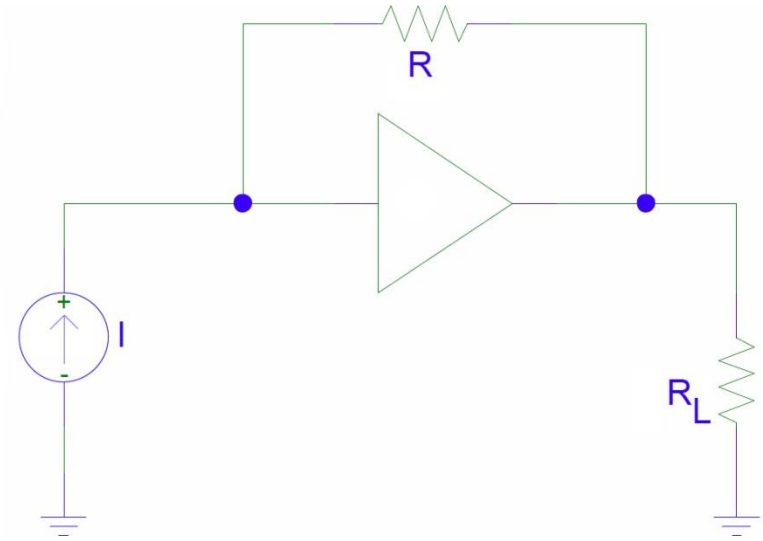

Figure 4-4: A simplified schematic of a transimpedance amplifier.

4.2.3 Detection Limit

The theoretical detection/sensitivity limit can be derived by calculating and then setting the $SNR = 1$ and solving for the electric field. Based upon the belief that the shot noise and the thermal noise are the main electrical dominating noise sources in the detection system, we will set all of the other noise sources to zero. Using this assumption the revised SNR equation is given by

$$SNR = \frac{\left(G_{TIA} W_{resp} P_0 \, E(t) \, \Delta T\right)^2}{\left(2q \, P_o W_{resp} \, G_{\mathrm{TIA}}^2 + 4 \, k_b \, T \, R\right) \Delta f} . \qquad [4\text{-}10]$$

The theoretical detection limit is determined by solving for the electric field that would produce $SNR = 1$ resulting in

$$\frac{E_{min}}{\sqrt{\Delta f}} = \sqrt{\frac{2\ q\ P_o\ W_{resp}\ G_{TIA}^2 + 4\ k_b\ T\ R}{G_{TIA}^2 W_{resp}^2\ P_o^2\ (\Delta T)^2}}. \quad [4\text{-}11]$$

Using the parameters given in Table 1 the resulting theoretical detection limit is given by

$$\frac{E_{min}}{\sqrt{\Delta f}} = 0.50 \frac{V/m}{\sqrt{Hz}}. \quad [4\text{-}12]$$

Table 1: Measurement parameters

Parameter	Value
Optical power, P_o	218 μW
Detector responsivity, W_{resp}	1.0 A/W
Thermal noise resistance, R	1 kΩ
TIA gain, G_{TIA}	1000 V/V
SCOS sensitivity, ΔT	$5.2 * 10^{-6} \frac{m}{V}$

4.3 Other Noise Sources

The previous section only took into account two noise sources, thermal and shot, when calculating the minimum detectable field because these are the two types of noise that are the most difficult to eliminate or reduce. The actual current minimum detectible field is much higher than the one derived at the conclusion of Section 4.2 due to other noise sources in the system. Figure 4-5 illustrates the basic SCOS detection system with potential sources of noise labeled. (The label numbers in the figure correspond to the subsection which describes the noise in greater detail.) The sources of noise in the simple system shown above are sorted into three categories depending on where they are generated. The three categories of noise include laser noise, fiber line/SCOS noise, and electronic detection noise. This section will briefly discuss each of these noise sources.

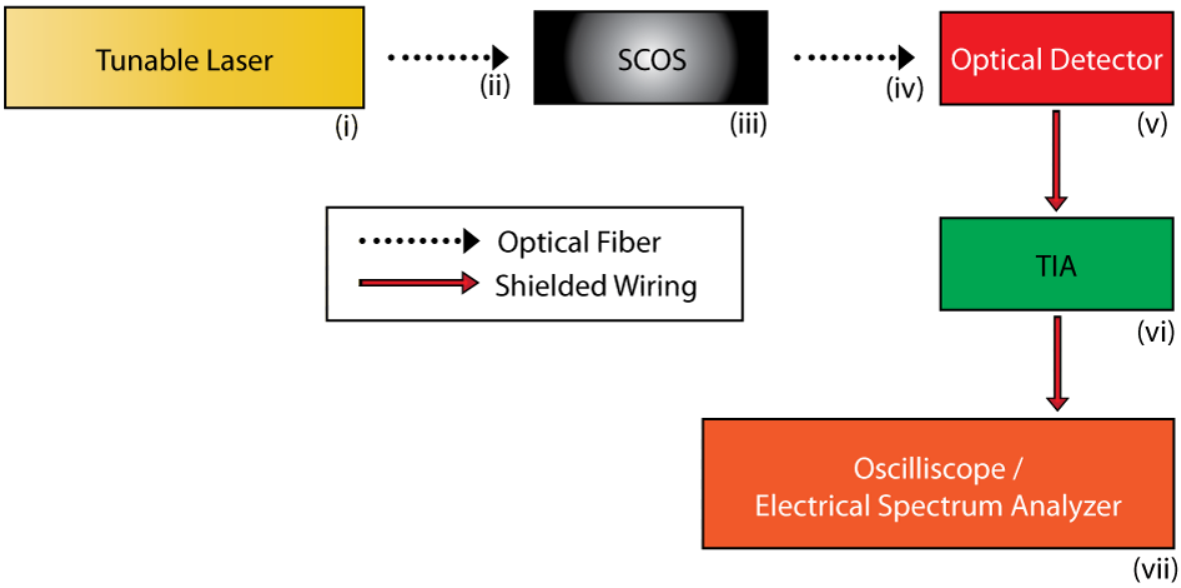

Figure 4-5: A block diagram of a simple detection system with numbered noise sources.
i) Power and noise from the tunable laser.
ii) Noise and attenuation from the fiber.
iii) SCOS signal, attenuation, and noise.
iv) Noise and attenuation from the fiber.
v) Conversion to current and shot noise.
vi) Conversion to a voltage, thermal and amplifier noise.

4.3.1 Laser Noise

The first place we detect noise is at the source laser itself. The laser's output power is not constant, and it varies with both time and temperature. This noise is often called relative intensity noise (RIN). In addition to the random fluctuations known as RIN, lasers tend to drift slowly in time for a variety of other reasons, including temperature, humidity, and electrical power variations, to name a few. Also, depending on the environment, the laser can also be subjected to RF pickup that is then translated into optical power noise. Many packaged lasers include feedback mechanisms that attempt to correct for these effects. Regardless, they are not always fast enough to keep the power stable. In addition, the feedback mechanisms cause the

output power to oscillate at a certain frequency w_f that looks like noise when the system output is captured by an optical detector.

4.3.2 Fiber Noise

While the polarized light travels down the fiber to the SCOS, it is subjected to mode mixing and attenuation. This attenuation of light simply reduces the overall magnitude of the power in the system.

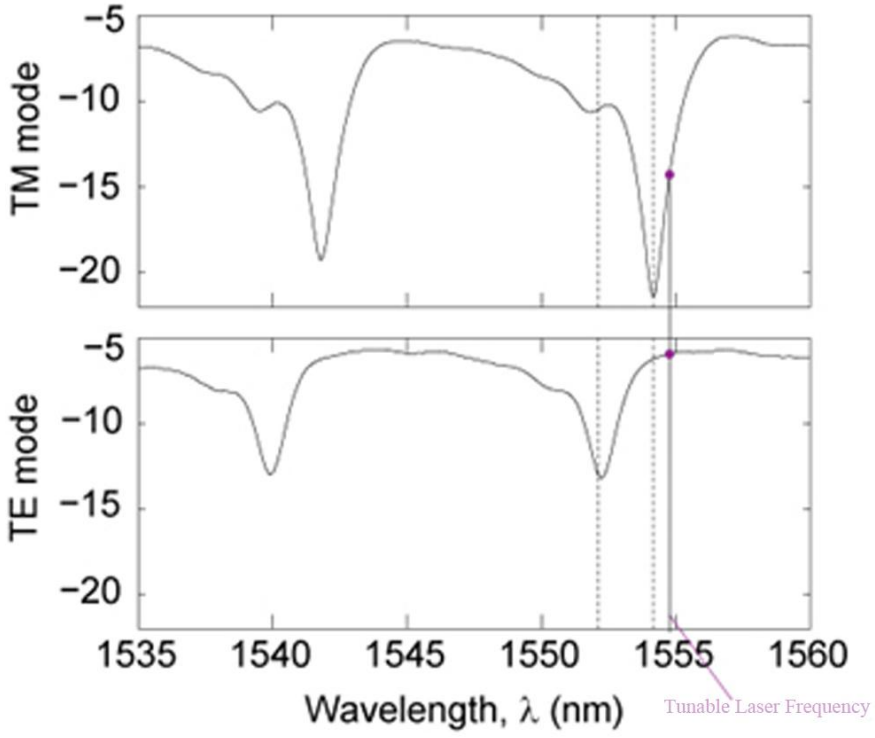

Figure 4-6: Illustrates the mode dependence of the SCOS spectral response.

Polarization maintaining fiber allows for two modes, the TM and TE mode. Figure 4-6 shows the spectral content of a SCOS with the source polarized to be TM mode and then the TE mode. Figure 4-6 shows that the response of the SCOS is dependent on the polarization. In

other words, TM polarized light gives a different spectral response than TE polarized light. Unfortunately, polarization maintaining (PM) fiber is not perfect at maintaining polarization. Random mode mixing, perhaps due to movement or vibration of the fiber, will result in a noise signal. The dominant polarization sensitivity in the system is the SCOS itself. Figure 4-6 shows the resonance for both TM and TE polarized light. Since the resonant dips for the two polarization states occur at different wavelengths, a variation in the polarization state of the light results in seemingly random fluctuation in the transmitted optical power.

In most general applications, we can safely ignore the effects of the second mode due to the fact that it is so very much smaller than the mode of interest. However, in these electric field sensing applications where the return SCOS signal of interest has been shown to be around 30dB less than the supplied optical power, even a miniscule mode mixing can damage the visibility of our signal.

4.3.3 SCOS Noise

When the light reaches the SCOS at the proper wavelength (tuned to a resonant dip), it couples out of the fiber and is lost. The amount of power that remains in the fiber depends on the position of the resonant dip which shifts with a change in the refractive index of the slab waveguide. The signal is produced when the electric field causes the change in the index of refraction. Other stimuli such as temperature vibration, strain, etc. also result in a shift in the resonance and thus produce noise [20].

When using the SCOS for electric field sensing, the temperature effects on a SCOS become a source of noise because temperature changes have an effect on the resonance locations. In order to characterize this noise source, a SCOS was placed on a hotplate and the temperature was varied. Figure 4-7a is a graphic showing how the test was setup, and Figure 4-7b shows the

results of this test. Eventually, the resonances appear to be completely destroyed, but while the resonances do remain they shift at a rate of 3 $nm/(C°)$ [1]. Under most conditions, the effects of temperature can be ignored because the SCOS is calibrated and measurements are taken immediately, before the temperature has time to change. However, during periods of long electric field capture, the change in temperature must be taken into account.

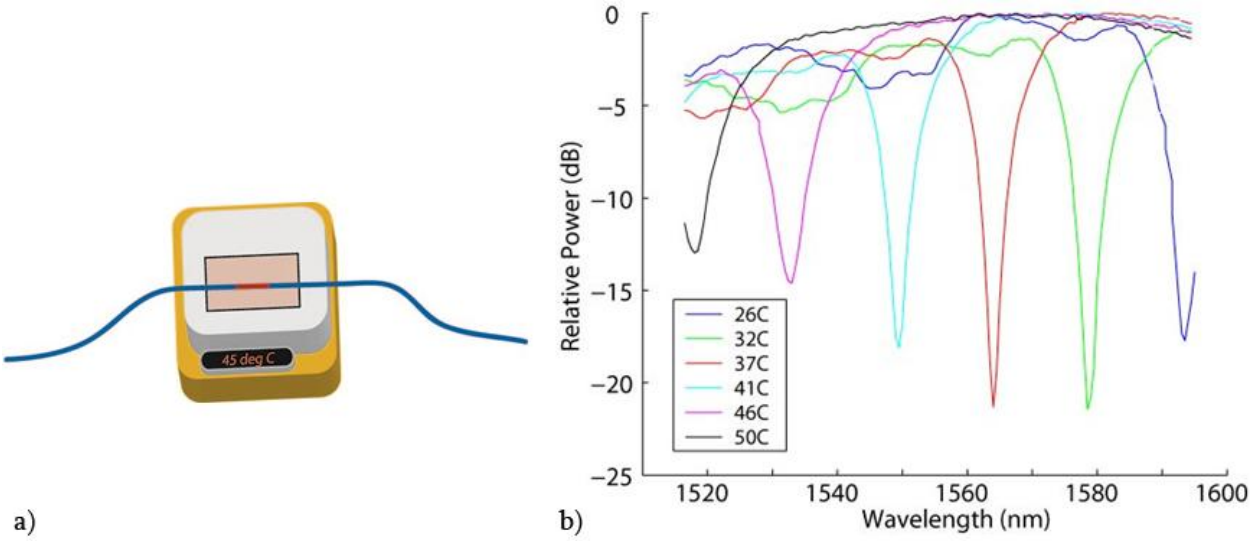

Figure 4-7: The setup (a) and results (b) of an experiment showing temperature effects on the SCOS [1].

When using polymer SCOS we have observed that the optical spectrum will shift over time as the amount of optical power passing through the SCOS is increased. The exact cause of this phenomenon is not completely understood, but its effects have been demonstrated to be very similar to that of a temperature change. Regardless of why, the increase in optical power causes a change in the index of refraction in the SCOS, which in turn causes a shift in the optical spectra.

Another external force that has an effect on the optical spectrum of the SCOS is strain or vibration. Even though the SCOS used in the field are well packaged, the strain forces still cause

minute changes in the way the SCOS is coupled to the fiber, which also results in a shift similar to that of temperature and power. In the lab, we created a way to simulate the strain experience by the SCOS in the railgun by impacting the SCOS package with a steal rod as shown in Figure 4-8. Tests using fiber brag gratings in both the lab and the railgun at GA Tech validate our setup by showing the magnitudes to be similar. In the case of the railgun, this strain noise can easily be 10 or 100 times greater in magnitude then that of the signal if steps are not taken to reduce this noise. The actual steps used to reduce this noise in the field are discussed in greater detail Section 4.4.3.

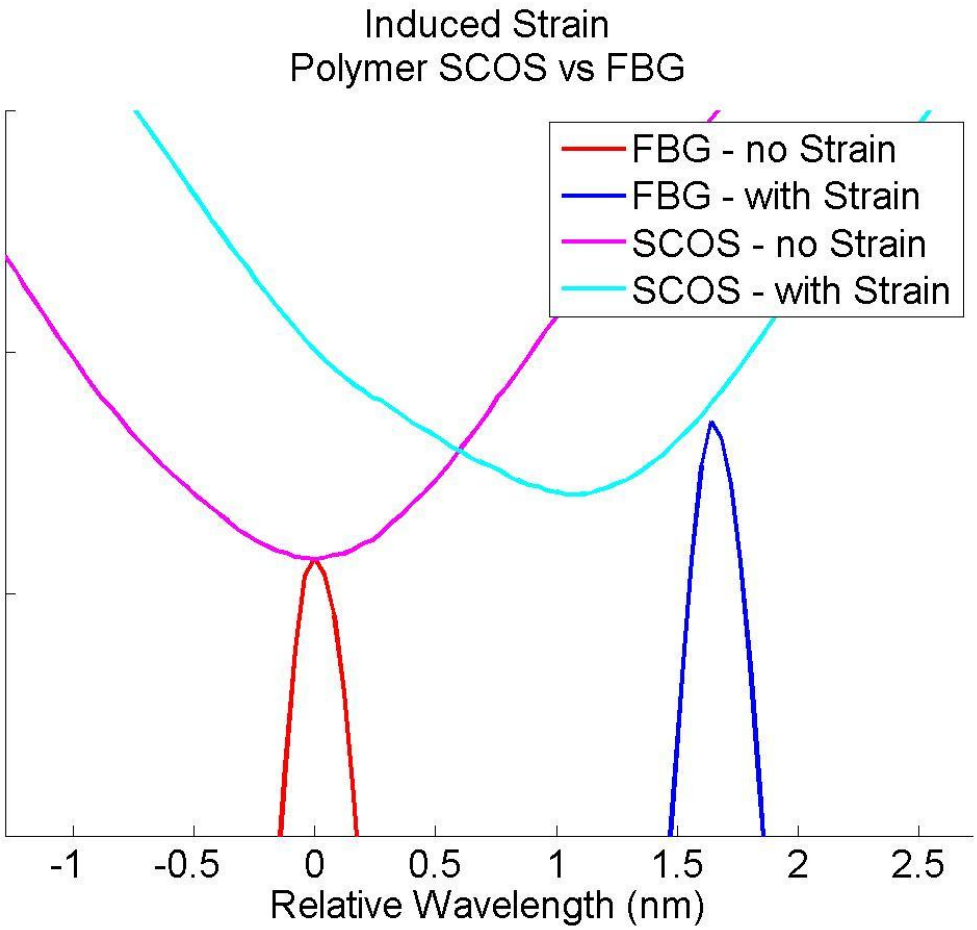

Figure 4-8: A graph that compares the effects of strain on a SCOS and a FBG.

4.3.4 Phase Noise

The return fiber path suffers from the same problems that are seen in the outgoing fiber path, namely mode mixing and attenuation. Another noise source that is prevalent in optical fibers is phase noise. Phase noise is primarily caused by back reflections within the fiber itself or at the fiber ends that cause sporadic destructive interference on the signal. Signals that are subjected to phase noise have significant high frequency noise and extreme sensitivity to movement on the fiber. Figure 4-9 shows a fiber that is subjected to phase noise.

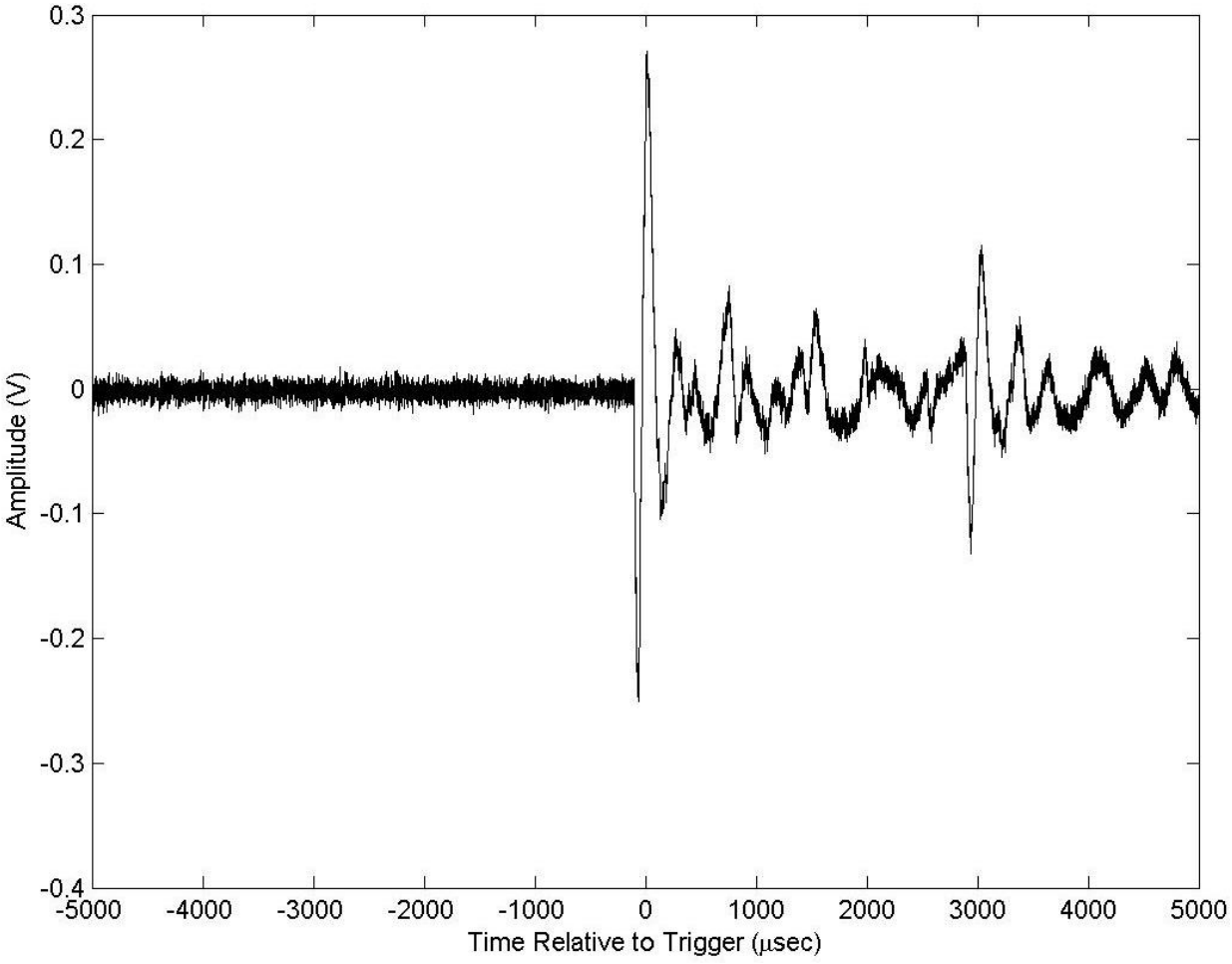

Figure 4-9: An illustration of phase noise on a fiber. The fiber is flicked at time T=0.

4.4 Noise Reduction & Compensation

The three largest sources of noise in the SCOS detection system have been shown to be the laser noise, the phase noise, and the strain noise. For this reason we have focused our efforts on reducing the noise in these areas. The following sections discuss reduction of each type of noise.

4.4.1 Laser Noise

If the laser power is not reliable, the rest of the system has no hope of being reliable. The best way to compensate for laser noise is to measure and record the laser noise by tapping off a small portion of the laser output before the SCOS. Figure 4-10 shows the captured laser signal that was tapped off a railgun shot. Without the laser tap, the oscillation at the beginning near time $T = 0$ would have been incorrectly regarded as strain. With the laser tap information, that particular noise can be compensated for using a MATLAB script.

4.4.2 Phase Noise

As mentioned previously, phase noise is typified by two things: high frequency white noise and fibers that are extremely sensitive to touch. After assembly, each fiber should be tested by flicking each fiber segment while watching the oscilloscope for resultant voltage fluctuations. The only effective way to reduce phase noise, that we have seen, has been to clean and re-clean each of the fiber connections carefully. Additionally, fibers that are terminated with APC connectors instead of the regular UPS connectors appear to be generally less susceptible to phase nose.

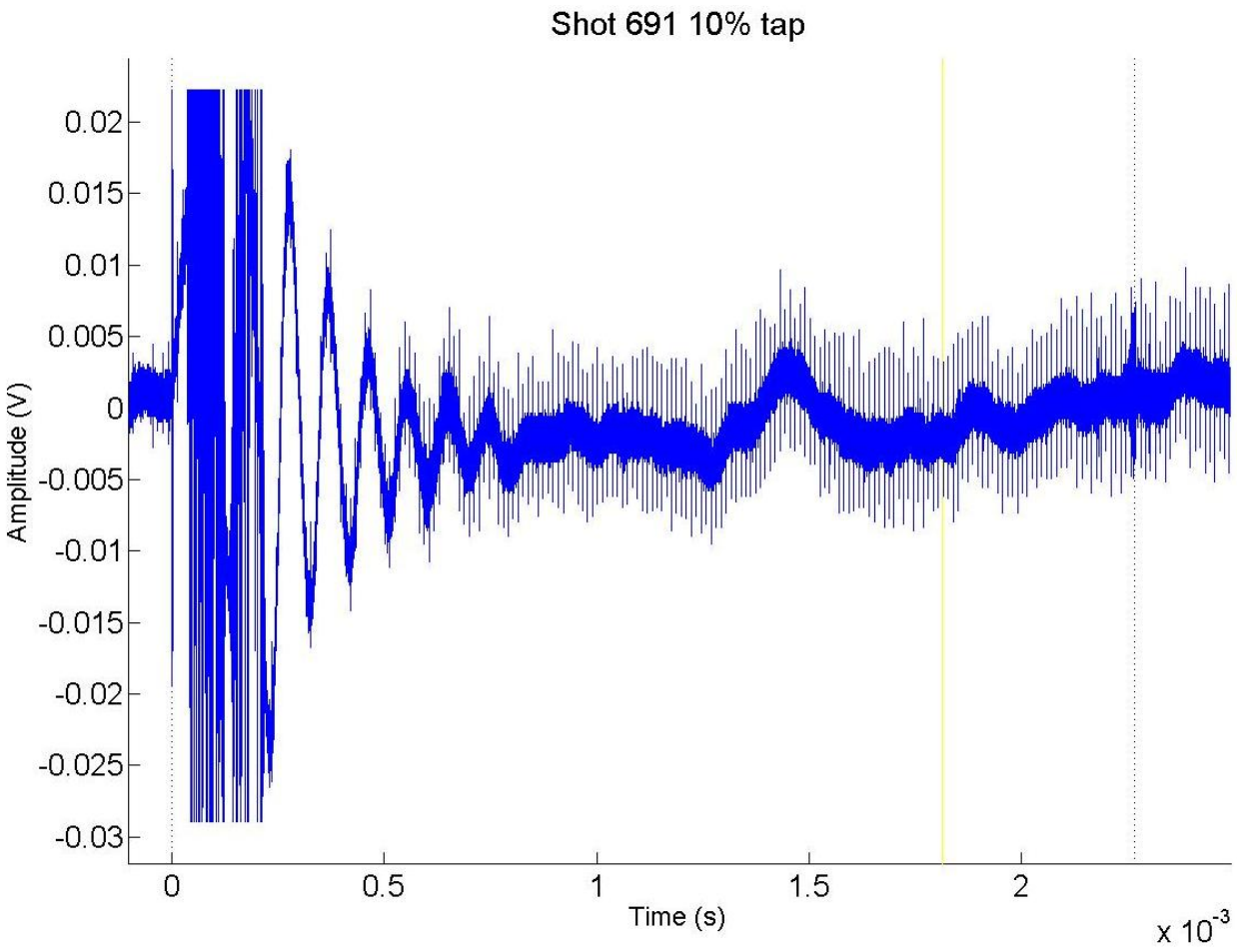

Figure 4-10: The recorded signal from a 10% laser tap during a railgun shot.

4.4.3 Strain Noise

As illustrated in Figure 4-8, strain on the SCOS will have similar effects to that of an electric field on the SCOS. Unfortunately, when placed in the railgun (or other similar environments), the amount of strain placed on the SCOS overshadows the electric field signal rendering it impossible to recover. To combat the effects of strain, we have placed the SCOS in a cartridge, suspended by the edges, so that SCOS has a little contact with the gun as possible. Figure 4-11 illustrates a SCOS that has been mounted using this suspension mounting technique.

Figure 4-11: A suspension mounted SCOS in an FR4 cartridge.

4.5 Actual Measurement Limit

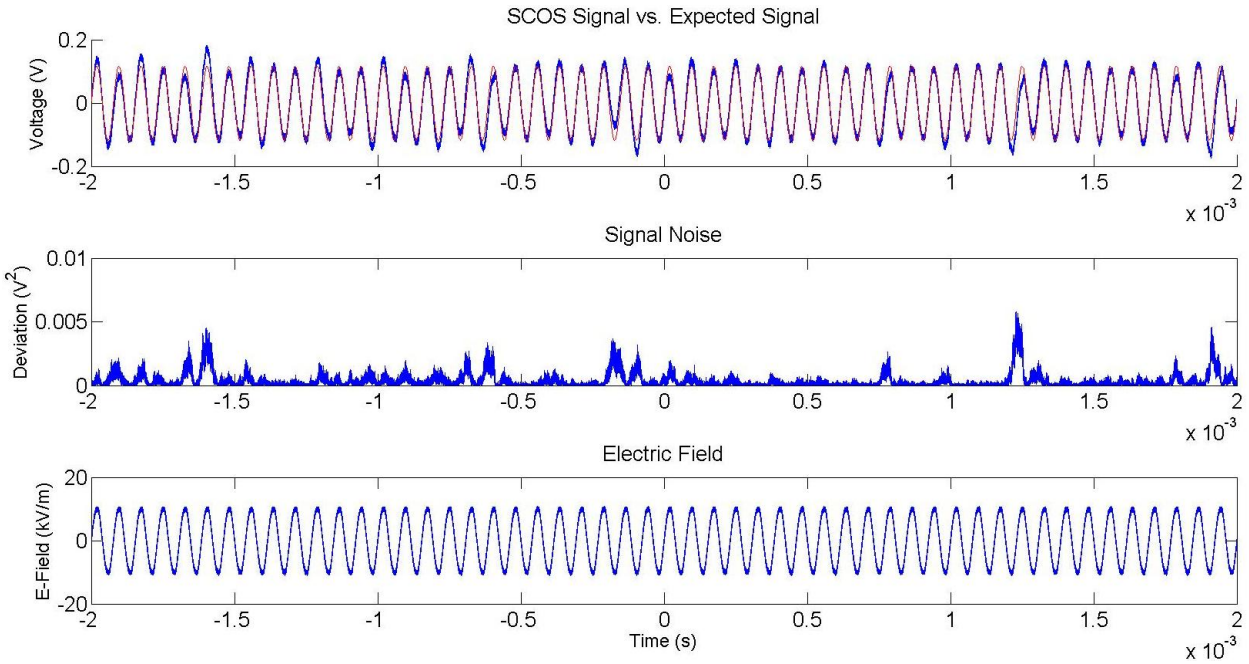

Figure 4-12: SCOS calibration signal (top), the noise deviation (middle), and the reference e-field (bottom).

The theoretical measurement limit provides a good basis for understanding the expected SNR of a measured signal. However, it does not provide a completely accurate model because it does not include the various noise sources in the system in the SNR calculation. To gain a better idea of the actual measurement limits data must be used from an actual test. Unfortunately due to the fact that the electric field pulse in a railgun that is the subject of interrogation has never

been confidently measured in this project the actual measurement limits of the SCOS sensor in a railgun cannot be determined.

While it is true that the actual measurement limits inside the active railgun cannot be precisely determined, it is possible using data gathered from the calibration of the SCOS to get a better estimate of the actual measurement limit. This is done by taking the calibration information of the SCOS shown in Figure 4-12 and finding the expected calibration signal also shown in Figure 4-12.

By assuming that the noise is uncorrelated, the SNR can be derived by taking the square of the recorded voltage peak (V_p^2) and dividing it by the mean of the noise power. We get the noise power by subtracting the expected signal from the actual one and then squaring it resulting in the signal shown in Figure 4-12. Using this approach the recorded voltage peak was found to be $118mV$ and the average noise power was found to be $3.36 * 10^{-3}\ V^2$. The SNR of the actual measurement shown in Figure 4-12 is calculated to be

$$SNR = \frac{\mathrm{V_p}^2}{mean(\sigma^2)} = 41.2\ . \qquad [4\text{-}13]$$

In order to determine the minimum detectable electric field, we need to relate the SNR in terms of electric field for a given bandwidth rather than voltage, resulting in

$$SNR = 41.2 = C\frac{\mathrm{E}(t)^2}{\Delta f}\ . \qquad [4\text{-}14]$$

By solving for *C* using the known parameters of the electric field strength and bandwidth, the SNR can be calculated for any combination of the field strength and bandwidth. The electric field strength, which is shown in Figure 4-12, is derived from the known voltage that was put on the rails and the known separation between the rails. The electric field amplitude is found to be

$\mathrm{E_{amp}} = 10.3\frac{kV}{m}$. The bandwidth ($\Delta f$) of the calibration system was $99kHz$. Combining all of the information about the calibration test together gives $C = 0.0385\frac{\mathrm{Hz}}{(\mathrm{V/m})^2}$.

The detection limit is determined by solving for the electric field that would produce $SNR = 1$ resulting in

$$\frac{E_{min}}{\sqrt{\Delta f}} = \frac{1}{\sqrt{C}} = 5.10\frac{V/m}{\sqrt{Hz}}, \quad [4\text{-}15]$$

which is larger than the theoretical limit derived earlier by around a factor of 10. When compared to theoretical limit using a system bandwidth of $50kHz$, which is more than large enough to sense the expected electric fields in the railgun, the theoretical minimum detectable field is found to be $112\frac{V}{m}$ and the measured minimum detectable field is $1.14\frac{kV}{m}$. While this is still smaller than expected electric field, there is still plenty of room for improvement.

5 RAILGUN TESTING

The main focus of my thesis has been the application of SCOS technology to the measurement of railguns. All of my contributions can therefore be tied to actual railgun testing. All of the railgun testing, which has spanned several years, has taken place at Georgia Institute of Technology located in Atlanta, GA.

In order to describe my contributions, I first provide a description of the specific railgun system used for all of the testing. Then I provide a brief description of the various tests that were performed, followed by a description of specific accomplishments.

5.1 GA Tech Setup

The firing portion of the railgun at GA Tech is in a sealed room that is placed on rollers to absorb the shock of the railgun. Figure 5-1 is a picture of the room with the gun. During firing, at the end of the muzzle of the gun there is a large blue canister that is reinforced in order to receive the fired armature. The blue canister is filled with wet rags to slow the projectile down and decrease the chance of fire. In spite of being frequently soaked with water, the rags do catch on fire owing to the energy of the projectile and have to be changed often. Figure 5-2 shows lab personnel changing the rags between shots.

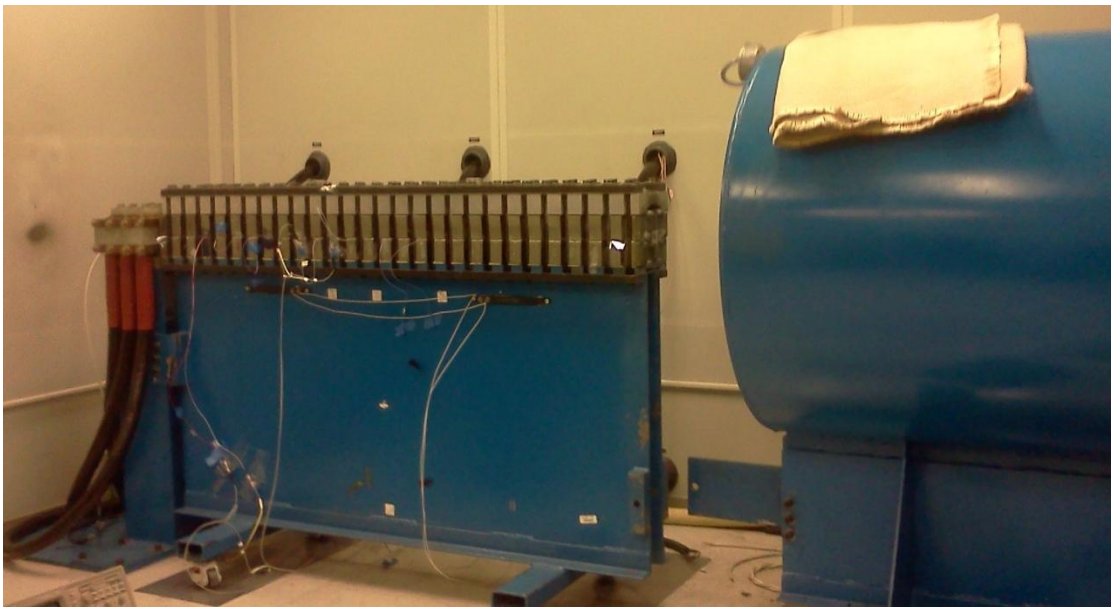

Figure 5-1: A picture of the railgun room at GA Tech.

Figure 5-2: Lab personnel changing the rags between shots.

At the opposite end of the gun from the muzzle and the blue canister is the breach. The breach end of the gun includes the interface between the rails and the capacitors that supply the current for each shot. Figure 5-3 shows this interface without the presence of the rail

containment unit. When the gun is ready to be fired the, the containment unit is bolted to this interface.

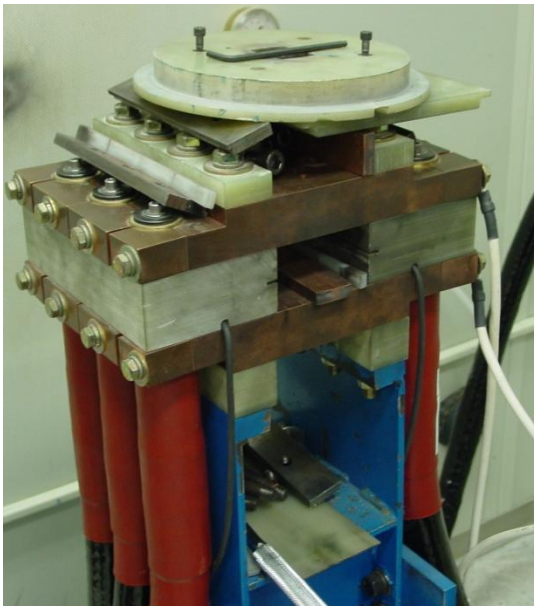

Figure 5-3: The interface between the capacitor bank and the gun rails.

All of the power supply electronics are in a room that is located to the side of the railgun. The supporting electronics include storage capacitors, shown in Figure 5-4, that provide the current necessary to fire the gun, as well as the firing timers, that dump the current from the storage capacitors into the gun at specified intervals in order to fire the projectile. The storage capacitors are attached to the railgun through heavy duty cables, which are visible poking through the wall just above the railgun containment in Figure 5-1, that are capable of handling the large amounts of current to fire the gun.

Figure 5-4: Two of the three capacitor banks (a) that power the railgun and single capacitor (b).

As mentioned in Section 2.3, the railgun itself consists of two rails that conduct the electricity that passes through the armature and causes the gun to fire. The rails are held apart by two "T" shaped insulators that hold them the proper distances apart. The insulators used in our testing are shorter segments of about 0.5 meters in length such that it takes three segments per side to correctly insulate the gun.

The green pieces shown in Figure 5-5 are the "T" insulators. The copper bar is also barely visible in this picture below the two "T" insulators. The steel material located below and on the outside of the copper rail and "T" insulators is the containment unit. Figure 5-5 also shows the fiber leads that are passed safely through the containment.

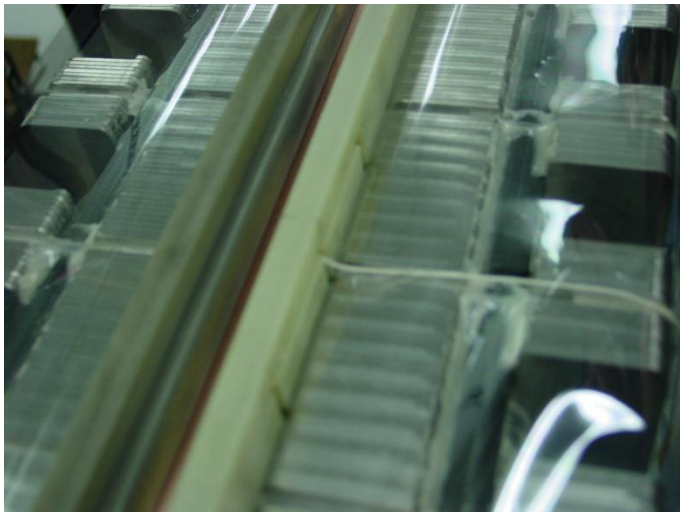

Figure 5-5: An insulator with a SCOS and one of its fiber leads secured in the bottom containment half.

The top rail is then placed on top of the "T" insulators and the top half of the containment is lowered over the rails and insulators. Figure 5-6 shows the top half of the containment being lowered onto the bottom half of the containment.

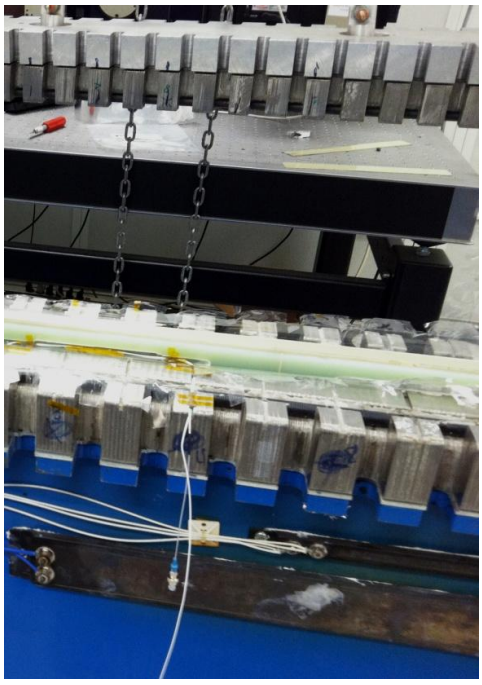

Figure 5-6: A completed sensor setup that is ready for the upper containment half to be placed atop.

The top and bottom containment parts are then secured together by a series of vertical bolts that are attached along each side of the railgun. Figure 5-7 shows the containment unit properly secured and ready to be move into place for firing. After securing the containment halves, the railgun, which is on wheels for easier assembly, is moved over to the capacitor bank interface unit and secured in place for the shots.

Figure 5-7: A picture of the secured rail containment unit.

For several reasons, including safety, the diagnostic and control electronics have been kept in a third room, shown in Figure 5-8, connected to both the room with the railgun and the room with the power supply electronics. This room has computers that allow for the selection of at what voltage level each shot is fired and what information is recorded about each shot. This room also has screens that allow the monitoring of the other two rooms while firing.

Figure 5-8: The room where the measurement electronics are kept.

5.2 Test Chronology

On site testing has been done at intervals over several years. Each subsequent test has seen some improvement in techniques than previous tests. Improvements in several areas including packaging, calibration, and sensing were observed. This section details the changes in techniques throughout the testing process.

5.2.1 February 2010

In February 2010, the initial set of tests for this project began on the GA Tech railgun. In this test, the sensors consisted entirely of KTP sensors. Each sensor was glued firmly into an etched section of the insulator. By carving out a space for the sensor in the insulator, shown in Figure 5-9, the sensor could be placed very close to the rail at the tip of the insulator. The insulator was the full 1.5m long and very cumbersome to transport. Additionally, due to the

stiffness of the sensor mountings and the TSA, several sensors broke during transport, which were impossible to replace upon arrival in the field.

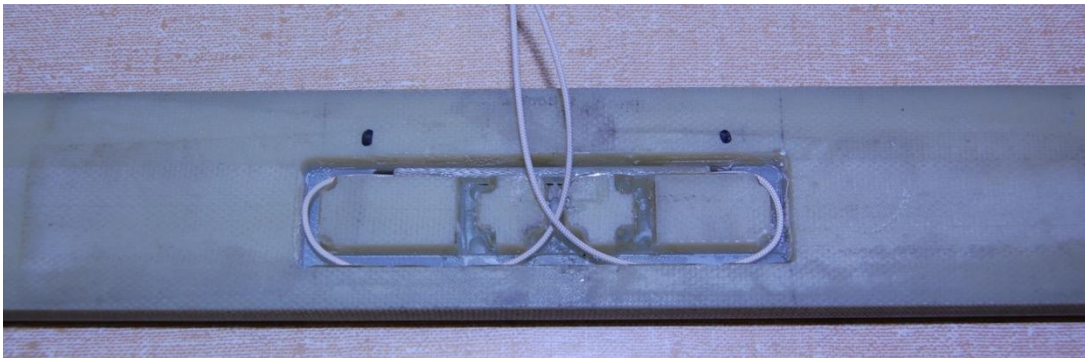

Figure 5-9: A sensor glued into the back of an insulator.

Figure 5-12 is an oscilloscope capture of a GA Tech railgun shot. The raw recorded signal is in green. The figure also has two additional lines representing filtered data: the red line is low pass filtered at 7MHz and the blue line is band pass filtered between 10 kHz and 7 MHz. The pulse occurring at approximately 0.9ms in Figure 5-12 was initially thought to be electric field. However, upon further examination, the pulse in question was eventually discarded due to the implausibility of what it represented. According to our calculations, the field that should be detected by the sensors should have been several orders of magnitude smaller than the peak detected. For this reason, the peak was classified as a kind of vibration noise on the sensor itself as the projectile made its way down the gun. The timing of the peak was ascribed to the fact that the point of greatest physical perturbation on the rails is when the armature is right next to the sensor. During this test, no actual field was visibly measured.

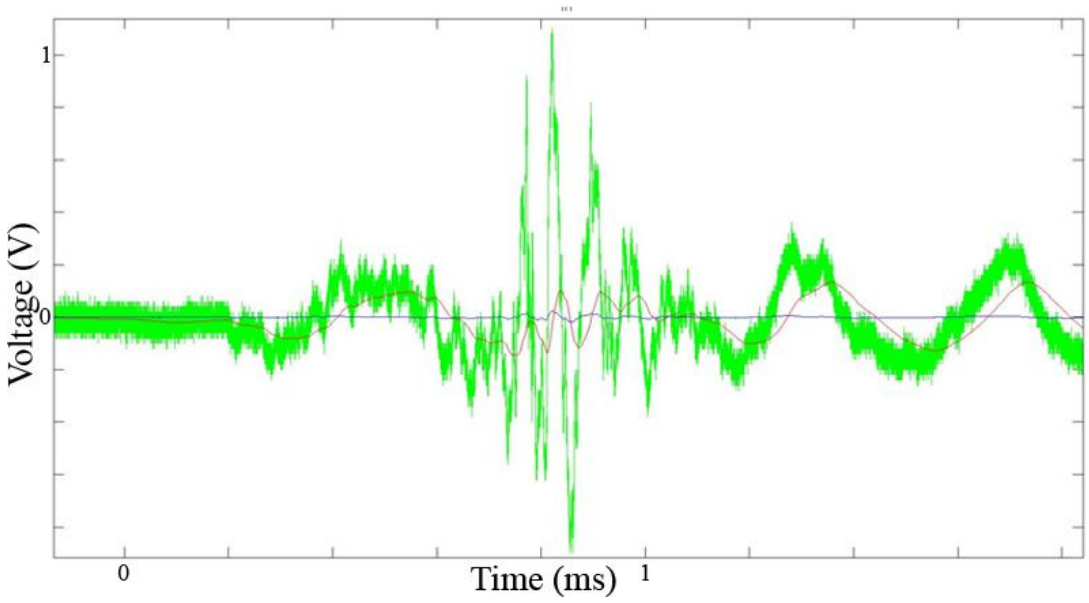

Figure 5-10: A sample of shot data. (Green: w/o filter; Red: filtered DC-7MHz; Blue: filtered 10kHz-7MHz)

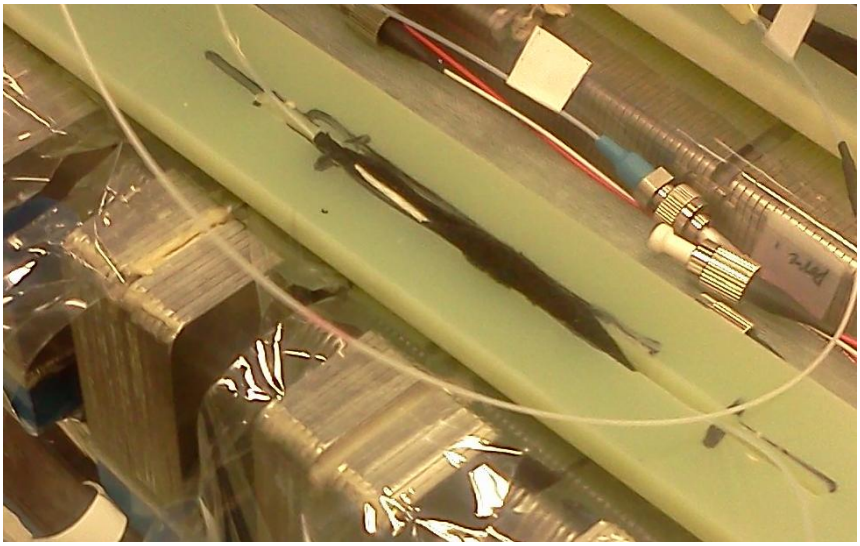

Figure 5-11: A SCOS sensor placed inside of an insulator using foam.

5.2.2 January 2011

Eleven months later, another test at GA Tech yielded better results in the survivability of the sensors. The single long 1.5m insulator for each side of the rail was still used, but the sensors were not glued into the cavities prior to shipping. The sensors slid into slots created for that

purpose right before gun assembly. Figure 5-11 shows an example of a sensor being slid into a slot in the insulator. During this test, the majority of the sensors were still KTP sensors, but at least one polymer was tested.

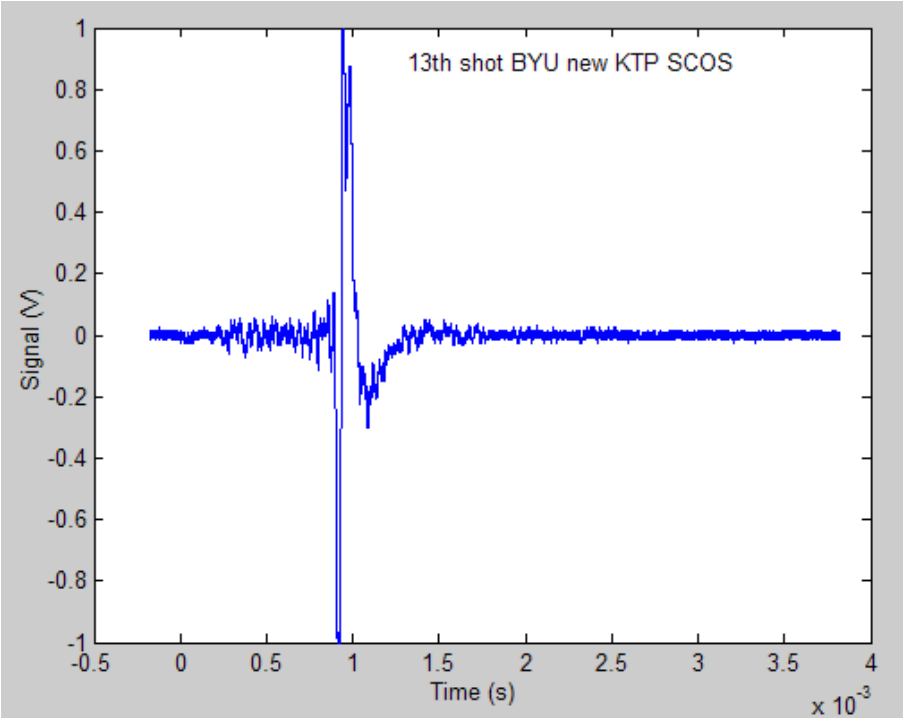

Figure 5-12: Data sample collected from the January 2010 trip.

Figure 5-12 shows a sample of the data that was collected during the January 2011 testing. This data also showed the same large dip and rise that was present in the February 2010 test. Unfortunately, strain noise was still too large to correctly sense any fields.

5.2.3 May 2011

The main focus of these tests was to reduce the noise due to strain by experimenting with various packaging techniques. Additionally, these tests showed the most dramatic change in testing techniques when compared with other interval test results. Prior to this test, the 1.5m

long insulator sections were cut into three equally sized sections of 0.5m. This allowed for easier transport to and from the GA Tech facility. Furthermore, it decreased the cost of replacing the insulator because the individual worn out sections could be replaced without having to replace the entire insulator.

The packaging or mounting techniques that we used during this test included placing the sensor in the rails with three different materials: putty, cotton, and foam. In addition to experimenting with the various packaging materials, the type of SCOS sensor was changed from KTP to polymer due to better sensing potential of the rail-to-rail electric fields.

It was during this test that we first experimented with calibrating the SCOS field while on the rails. Prior to this trip, all calibration was done in the lab and it was assumed that the SCOS was not changed in any way by being placed in the railgun. Calibration is done after the railgun is connected to the capacitor interface by connecting a high voltage sinusoidal signal on the rails. While continuing to apply the voltage to the rails, both the voltage on the rails and the converted voltage were measured in time using an oscilloscope in order to gather better data regarding the size of the field.

In spite of the calibration and other improvements that were made, the data, shown in Figure 5-13, still had too much strain to guarantee that an electric field was shown. Using data provided by researchers at Lawrence Livermore National Laboratory, we were able to also make plots of what the theoretical models predicted the electric field should look like [9]. This knowledge, combined with sensors inside the gun which determined the location of the projectile in time, made it possible to plot the theoretical field on top of the recorded signal for comparison.

The most promising of all the shots, shown in Figure 5-13, did have a spike at the proper time. The spike appeared to be the negative of the theoretical signal. This lead to the discovery,

which was confirmed by lab tests, that SCOS slab is directionally sensitive meaning that a SCOS oriented right side up will give a signal exactly negative that of the same SCOS oriented upside down. In spite of the fact that the peak looked the same as it should look and occurred at the same point, we determined that we were still measuring strain as the magnitude of the peak was still much too large to be the field.

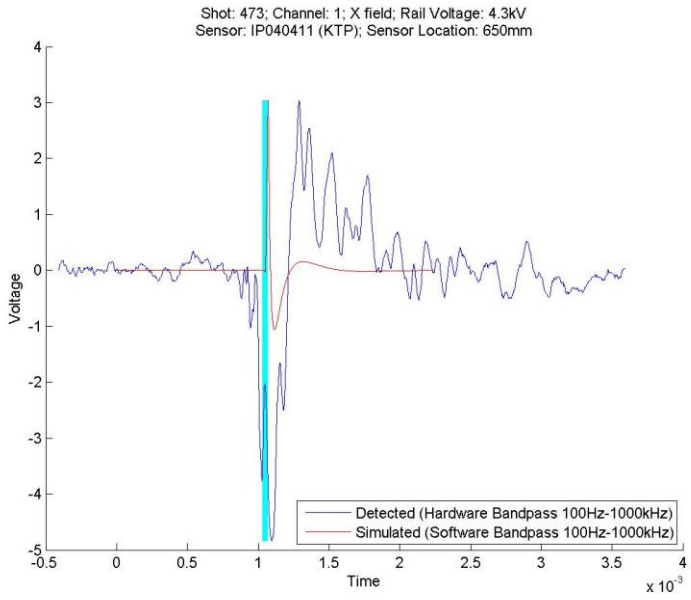

Figure 5-13: A plot showing both the simulated and detected field (note that they appear to be inverted).

5.2.4 August 2011

The August 2011 testing spanned the entire month and was primarily focused on reducing the strain noise detected in the previous tests. This testing utilized a combination of FBGs and Polymer SCOS; KTP SCOS were not used during this trip due to their decreased sensitivity. During the first half of the testing, a series of FBGs was utilized to test the effectiveness of the various packaging techniques in more detail than was possible in the shorter, previous tests. Figure 5-14 is a plot of the results of one of the more promising FBG tests.

While testing of the FBG on the railgun, it was discovered that the glue currently being used to secure the sensors to the substrate, a generic five minute epoxy, was ineffective at holding the sensor. The glue was allowing the motions of the gun to actually move the sensors themselves. This discovery led to the use of a new type of glue, M-bond, that holds the fiber much more securely to the package.

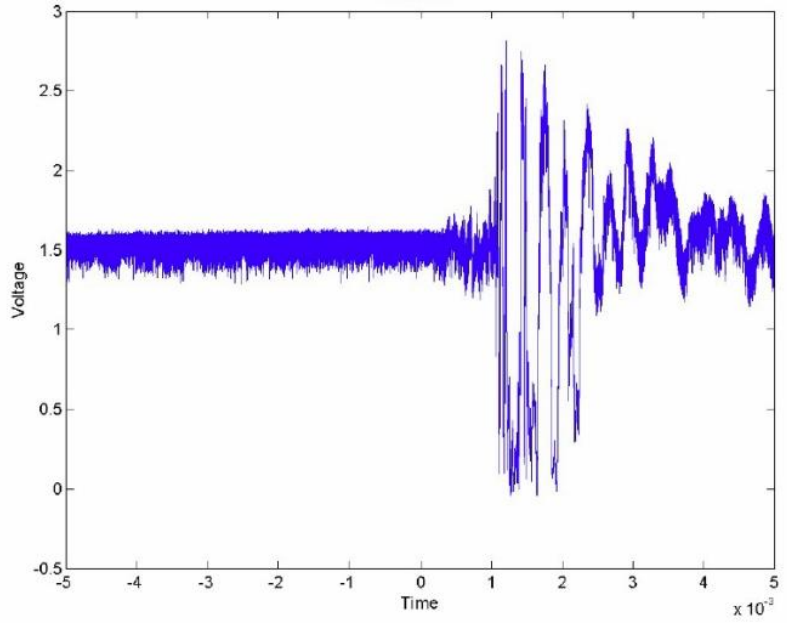

Figure 5-14: The results of a FBG mounted on FR4 placed surround with foam.

Also during the August 2011 testing, the method of calibration was greatly improved. As mentioned in the description of the May 2011 tests, calibration is done after the railgun is connected to the capacitor interface by connecting a high voltage signal to the rails. While applying a high voltage to the rails, both the voltage on the rails and the converted voltage were measured and recorded in time using an oscilloscope. During these tests, we preserved those plots and returned to the lab to determine a more exact idea of field strength. Figure 5-15 shows a side by side comparison of the two captured channels along with fitted sinusoid used to detect

the true amplitude through the noise. Using this information, along with the known distance between the rails, we were able to compute which voltage levels corresponded to which amplitude of electric field. This knowledge enabled the creation of plots that would show the strength of the field in comparison to the voltage level recorded.

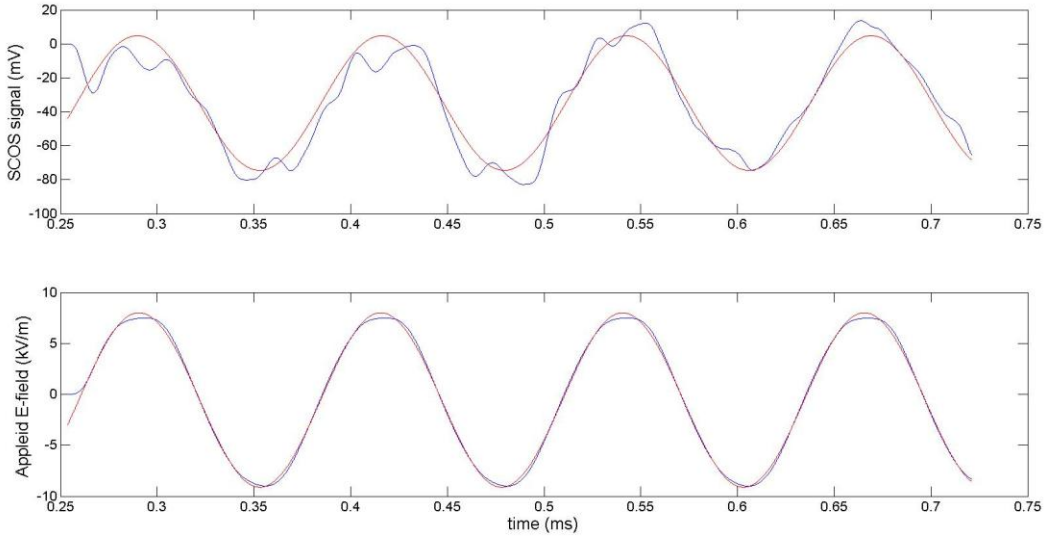

Figure 5-15: The calibration data for one of the SCOS sensors.

Figure 5-16 shows a SCOS capture along with the appropriate voltage level corresponding to a $10\frac{kV}{m}$ field. The field levels, like previous tests, were expected to be under $10\frac{kV}{m}$. This meant that in spite of the improved glue and packaging methods used, the information detected was still primarily, if not entirely, strain pickup. This is especially true of the oscillations that begin to occur after the armature had passed approximately$0.6ms$.

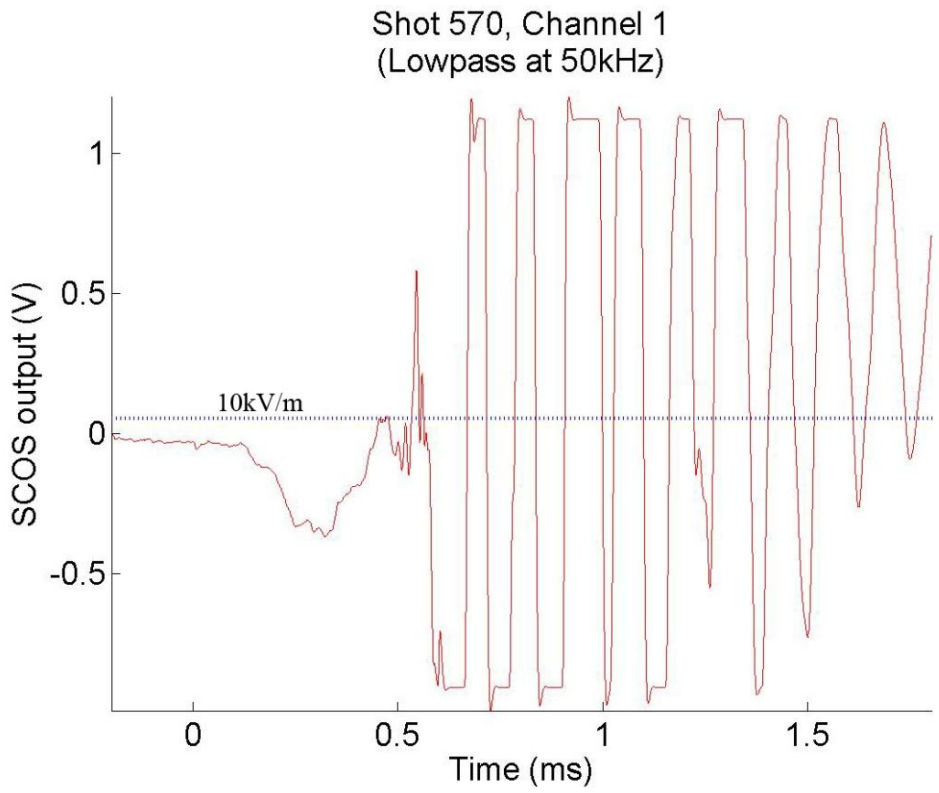

Figure 5-16: A captured, filtered SCOS plot with the electric filed calibration displayed.

Some of the final shots done during the August 2011 tests included gluing a metal bar to the bottom of the FR4 of the SCOS in order to help decrease the flexing of the FR4. This seemed to reduce the strain noise picked up by both the SCOS and the FBG until the magnetic forces in the gun pulled the metal bar through the insulator wall and into the barrel of the gun, destroying the sensor shown in Figure 2-13.

5.2.5 December 2011

After analyzing the data from the August 2011 tests, a new packaging technique was born, the cartridge. The cartridge consists of a hard outer shell, made of FR4, with the SCOS properly packaged inside. The cartridge was first envisioned to help speed the installation and take down of SCOS into the insulator and to decrease the number of SCOS broken in the

process. The cartridge was to be installed directly into the insulators with minimal effort using a foam pad surrounding it to both dampen the vibration effects and to ease the ability to remove it. Figure 5-17 shows a picture of a SCOS inside a cartridge.

Figure 5-17: A SCOS inside of a three sided cartridge.

Also evident in Figure 5-17 is the concept of suspension mounting a SCOS. After the previous test of August 2011, it was theorized that suspending the sensor in air inside the insulator might provide a greater strain reduction than the previous attempts using foam, putty, or cotton. Also, up to this point, all of the tests had the SCOS mounted on an FR4 board, which is quite springy and not at all resistant to strain. In addition to the suspension mounting, the FR4 was changed out in favor of stiffer materials namely: sapphire and ceramic. To test this hypothesis, a series of FBGs mounted in the cartridges were sent to GA Tech to be tested.

The graphs in Figure 5-18 show the results with the cartridge. The wavelength shift due to strain was reduced to approximately a $.08nm$ maximum shift in wavelength. This wavelength shift due to strain was dramatically less than with the FR4 mount FBGs in which the wavelength shift was larger than the FBG reflection band.

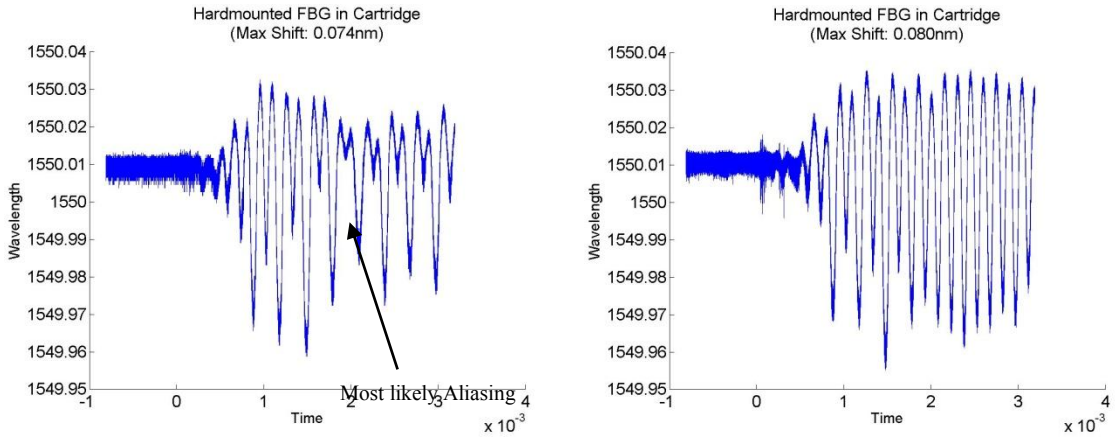

Figure 5-18: The results of two FBGs hard mounted and suspended in a cartridge.

In addition to the reduction in strain amplitude, the strain now has a single dominant frequency. The graphs in Figure 5-19 are the frequency response of the FBG for the two tests. Unlike previous FBG tests without using the cartridge, the frequency response of the two tests appears to be correlated between shots. They both have pronounced spectral content around 7kHz. (The graph on the left shows an additional peak at around 3.5 kHz.) Due to the spectral correlation between shots, it is now possible to use a carefully designed notch filter to reduce the strain and to determine the electric field signal as long as the SCOS has the same strain resonance.

The two tests performed on the FBG illustrate advancements in the area of strain reduction. In previous tests, not shown, the wavelength shift of the FBG was beyond the range of the FBG to detect. Additionally, each shot using a FBG without the cartridge has had a completely different frequency and time response that appeared to have no correlation between shots.

The wavelength shift of an electric field SCOS is on the order of 10pm which is still smaller than the strain noise. So, while the results show that a great deal of progress was made,

still more progress was required in order to actually see electric field. This testing also allowed us to validate our lab experiments. These experiments correctly predicted the decreased strain noise.

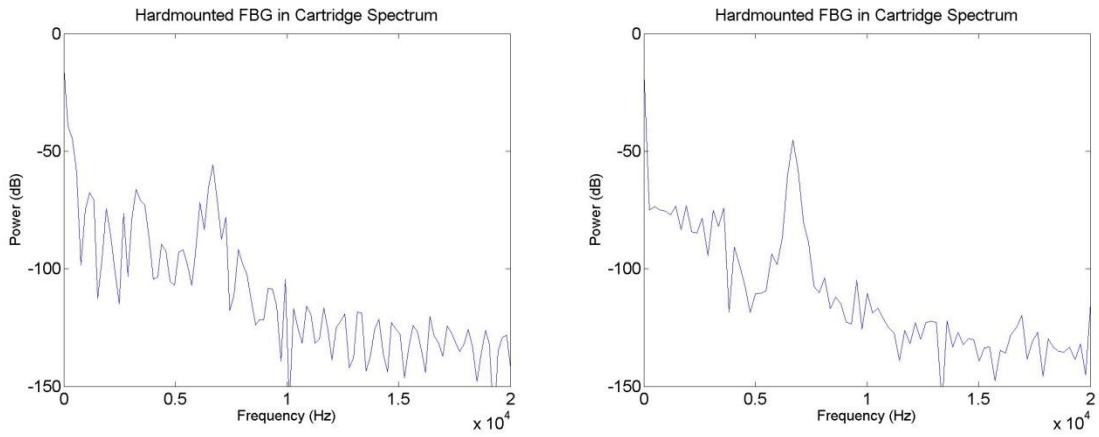

Figure 5-19: The spectral content of the same FBGs hard mounted in the gun using a suspension cartridge.

5.2.6 January 2012

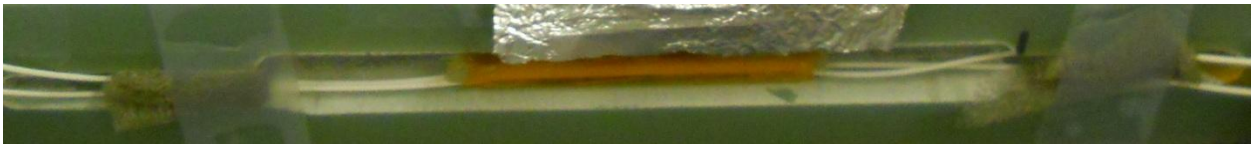

Figure 5-20: A dual sensor mounted into a rail for testing.

In the January 2012 tests, we attempted to apply our previous improvements and testing modifications in an effort to allow us to see electric field. In these tests, we used only dual sensors. These dual sensors, shown in Figure 5-20, were Polymer SCOS that were hard mounted alongside a FBG on a ceramic or sapphire substrate using M-Bond glue. Our test model was intended to monitor both field and strain. We concluded that if we received a strain signal on the FBG, we would then know that the corresponding signal on the Polymer SCOS was also strain

and not field. In addition to monitoring the FBG, we also monitored the laser source to determine which if any of the fluctuations were from imperfections in the laser source.

The Figure 5-21 shows the results of the test (note that the FBG and the laser source are normalized to the SCOS). There were several interesting observations of note from this figure. First the laser fluctuations, which we had never previously observed, were quite high in the beginning right after the shot was fired. This caused both the FBG and the SCOS to oscillate at the beginning. Fortunately, this oscillation died off before the armature made it to the location of the SCOS. The second thing of note is that we have the same shaped peak that we have experienced in previous trips that is similar in shape to what the theory tells us to expect. Unfortunately just like the previous trips, the amplitude of this peak is too large to actually be field. We must conclude that this peak is at least partially noise.

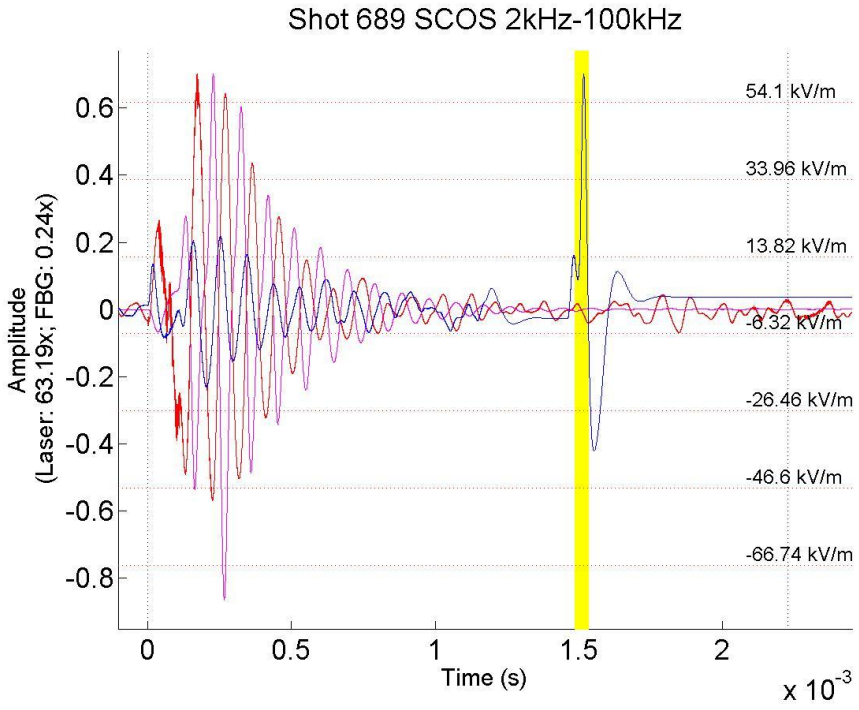

Figure 5-21: A plot of the SCOS (blue) and the normalized FBG (magenta) and laser source (red).

5.3 Accomplishments

The primary focus of my thesis has been the application of SCOS technology to the testing and evaluation of railguns. My contributions are detailed in four sections.

5.3.1 Oscilloscope Data Capture

The basic signal produced by a SCOS is given by

$$V(t) = V_0 + \Delta V\, E(t), \qquad [5\text{-}1]$$

where V_0 is the voltage detected with no applied electric field, ΔV is the change voltage as a function of applied electric field, E. As explained in Chapter 4, the voltage change is typically much smaller than the zero field voltage. For a sinusoidal varying applied electric field with amplitude $1\frac{kV}{m}$, the ratio between the DC component and the AC component is approximately

$$\frac{\Delta V\left(\frac{1kV}{m}\right)}{V_0} \approx 200. \qquad [5\text{-}2]$$

Since the received signal is essentially a small time varying component added to a larger DC component, an electric spectrum analyzer (ESA) is a good method to extract the desired portion of the signal. However, the ESA is only useful if the electric field is periodic. Since the railgun creates a pulsed signal, the ESA cannot be used effectively. One of my initial accomplishments has been to move from using an ESA to measure and record signals to using an oscilloscope.

The photodiode generates a current which, when using the SCOS, has a large DC component that is much larger than the desired AC signal of interest. Using standard amplifiers, this large DC current would cause the amplifiers to overload and rail which would distort our

signal and, given time, would likely harm the amplifier. Therefore, there is a need to block the DC portion of the signal before any significant amplification can be done.

To eliminate the most noise possible, the DC component of the photodiode current needs to be filtered out prior to conversion into voltage by the transimpedance amplifier (TIA). With the DC block placed before the transimpedance, special care needed to be taken to not upset the DC biasing of the photodiode.

The DC block of current is different than a voltage DC block, which can be accomplished using a single capacitor. A current DC block uses an inductor to shunt DC current signals to ground. The circuit diagram for the current DC block is shown in Figure 5-22. It consists of an inductor and a capacitor as well as a resistor. Theory would indicate that only an inductor is necessary, but when implemented testing showed that the inductor has a resistance that prevented all of the DC from being blocked. This DC voltage, which is directly proportional to the current delivered by the photodiode and the resistance of the inductor, can alter the biasing of the photodiode if special care is not taken. For this reason, the capacitor and the bleed resistor were introduced. The combination of the capacitor and the bleed resistor reduce the effects of the DC voltage on the photodiode and provide the correct frequency response. The DC block has a corner frequency of approximately 100Hz, as shown in Figure 5-23.

After introducing the DC block, we were able to more aptly measure electric fields on the oscilloscope. To further increase our ability to see the signal, I implemented several hardware filters that we have used during some of our measurements to improve our SNR.

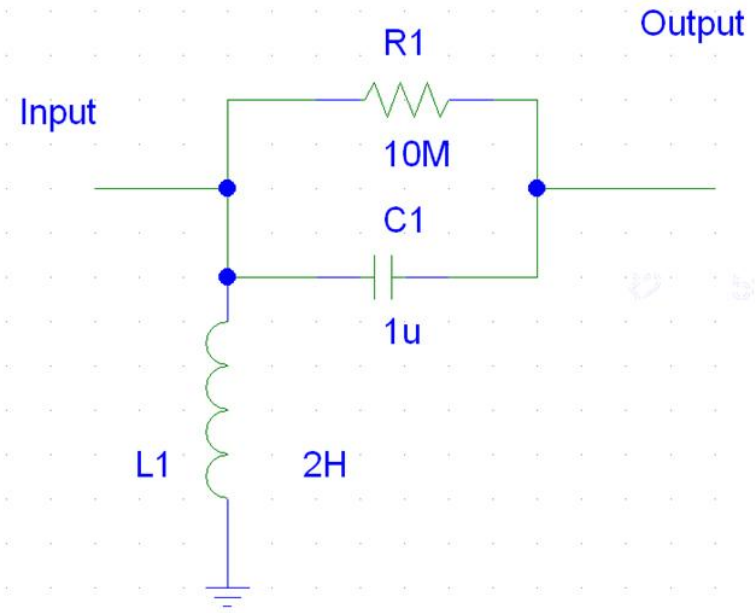

Figure 5-22: A current DC block with a corner frequency of approximately 100Hz.

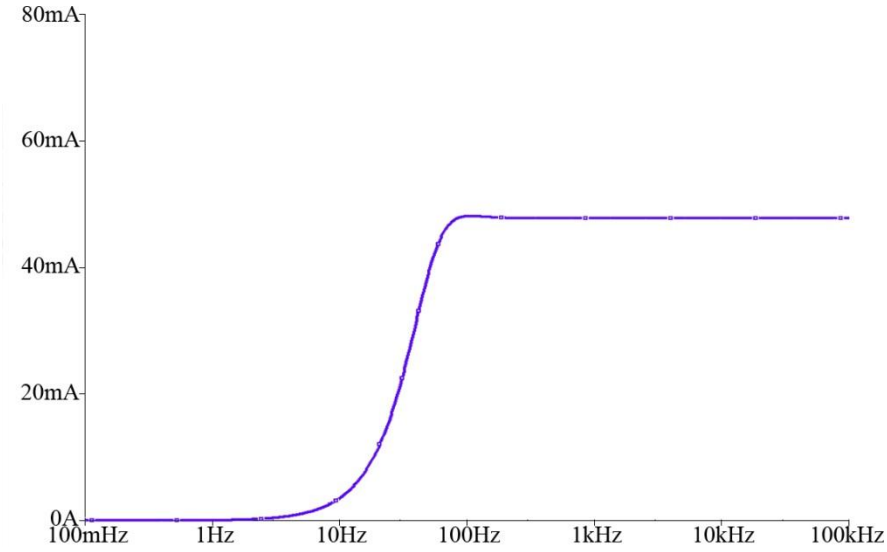

Figure 5-23: Simulated frequency response of the DC block.

5.3.2 SCOS Packaging

In order to place the sensors close enough to be able to see the desired fields, the sensors are actually placed within the "T" shaped insulators. The packaging includes both the routing of

the optical fiber leads out of the railgun containment and the specific attachment between the SCOS and the "T" insulator.

Routing the fiber leads out of the gun must be done with care to avoid damaging the leads when the containment is secured in place. The railgun at GA Tech has small groves that allow for the passing of the fiber from the "T" insulator to the outside of the gun. Experience shows that placing foam on top of the fiber while in the grove and then tapping the foam down flush with the surface provides the greatest assurance that the fiber will not be damaged when the containment is closed.

Original installations of the SCOS in the gun were done by hard gluing the fibers into the insulator as shown in Figure 5-9. As mentioned previously, that had several disadvantages including the fact that the SCOS could not be reused for other purposes or changed if damaged. By reengineering the holes in the insulators where the SCOS goes we were able to simply insert the packaged SCOS using foam to secure it in place. The new holes were milled from the back of the "T" insulator (away from the bore) toward the rails. This new technique allowed for a much greater flexibility in placing and removing sensors. Figure 5-11 shows a SCOS mounted into the insulator rails using foam.

While the foam technique provided a great improvement in the portability and reusability of the sensors, it still required someone with experience to correctly place and secure the sensors. To combat this, we developed a new method for inserting the SCOS sensors by using a cartridge. The cartridge has a variety of advantages both in terms of ease of inserting the sensor into the gun and reducing the noise. The idea behind the cartridge is that the slot in the back of the "T" insulator is enlarged to the point that cartridge fits snuggly into place and will remain correctly in place simply due to its placement.

The cartridge system was also expanded as a method to combat the noise generated by the strain of the gun. Lab tests showed that by suspending the SCOS between two points reduces the noise generated by strain on the SCOS when impacted. The cartridge allows us to use the lab to correctly mount the SCOS, to minimize noise, and then easily place the mounted SCOS into the gun.

5.3.3 SCOS Calibration

As can be seen in Section 5.2, the measured signal contains features that are not caused entirely by electric field. Therefore, to gain confidence in the measured signal it is necessary to get an estimate of the electric field sensitivity in the actual testing environment. This calibration is even more relevant when we switch from SCOS fabricated using KTP to electro-optic polymer because the resonance of polymer-SCOS tends to change with time and temperature. The SCOS calibration process that I developed can be divided into two separate parts. The first part involves determining the optimum wavelength for operation, or calibration laser tuning. The second part of the SCOS calibration is determining the factor that relates the voltage change to applied electric field. This coefficient is labeled as $\Delta \boldsymbol{V}$ in Equation 5-1.

Calibrating the wavelength of the laser to the optimum spot was originally done by hand. After connecting the SCOS to the laser source, it was necessary to choose an appropriate wavelength to optimize the signal produced by the SCOS. The optimal wavelength for a SCOS is determined by a combination of factors. The first consideration is the steepness of the slope. As shown in Section 4.1, the greater the slope of the SCOS optical response where the laser is the greater, the power swing will be in response to applied electric field. Therefore, it is optimal to choose a location that is as steep as possible. Another factor to consider is DC optical power. The lower the DC optical power after the SCOS, the more amplification that can be applied and

less signal processing due to the fact that the SCOS itself acts as a DC block. This is appealing because the desired AC signal is very small. Considering both of these factors leads to choosing a steep slope near the bottom of the resonant dip.

In the lab, choosing the exact wavelength to use involved applying a known electric field using electrodes and a function generator and then measuring the SCOS signal using an ESA to compare the signal of the SCOS at various wavelengths. Unfortunately, carrying large amounts of equipment is challenging for use in field calibration. I developed another method for calibration which has proven just as reliable as the ESA and function generator combination at a fraction of the cost, size, and weight.

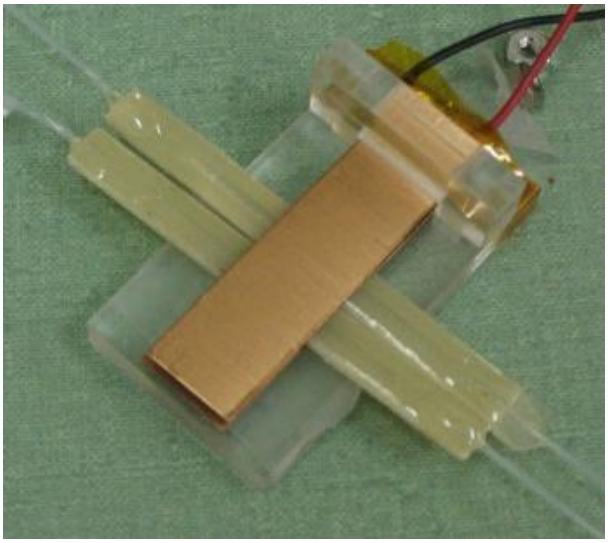

Figure 5-24: A pair of electrodes used for calibrating SCOS.

This method employs a USB sound card and Labview. The Labview program (described in detail in Appendix B) produces a pure sinusoidal tone in the audible frequency range. This tone is then fed into a high voltage amplifier which is connected to electrodes on both sides of the SCOS. In order to generate a large signal, closely spaced electrodes shown in Figure 5-24

were used. This initial approach required the SCOS to be calibrated prior to inserting it into the railgun. However, I found that the calibration can also be accomplished with the SCOS already inserted into the railgun by using the copper rails as the electrodes. This changes the electrode spacing from a few millimeters to 14 millimeters.

The Labview program records the response as it tunes the laser across a specified frequency band. Extensive filtering is employed to extract the amplitude of the response at the generated sinusoidal tone frequency. The wavelength whose response had the largest amplitude compared to the background noise is then recommended by the program. Figure 5-25 shows an example of the resulting laser tuning output. It is interesting to note that the results of the program correlated very well to the derivative of the SCOS spectrum.

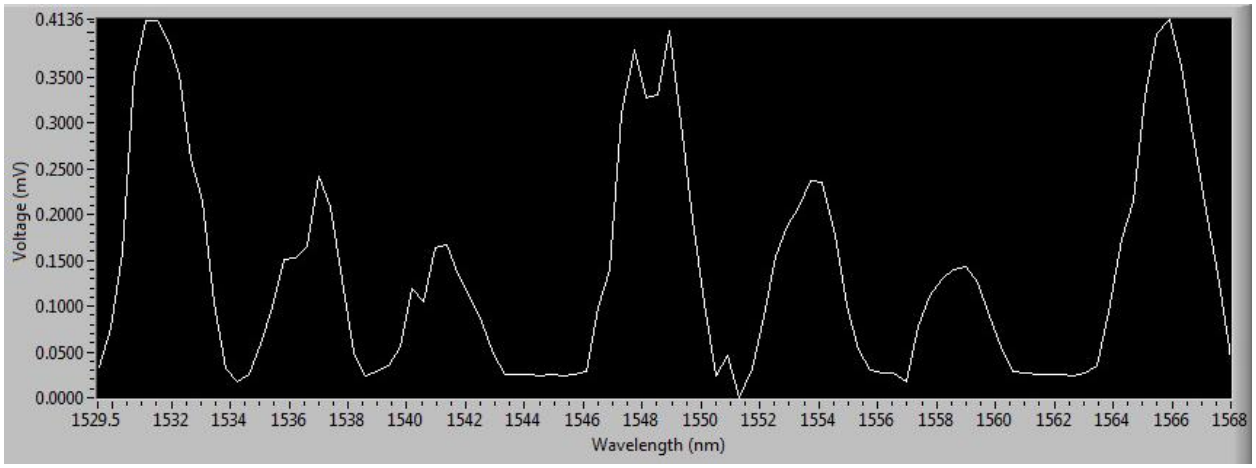

Figure 5-25: The front panel of the automatic calibrator displaying the results of a scan of a SCOS.

Not only is it necessary to correctly calibrate the wavelength of the SCOS, it is also necessary to calibrate the voltage recorded by the oscilloscope to the field strength sensed by the SCOS. This is done by placing a known sinusoidal voltage around the SCOS sensor, creating an electric field. In the case of the railgun, the calibration is done with the sensors in place by

introducing a known voltage on the actual rails of the gun. It is important to take into account during setup that the diodes used in the firing mechanism at GA Tech place a limit on the voltage that can be applied at around 70V. Additionally, calibration cannot be done after the gun is loaded with an armature which creates a short across the rails.

With the electric field applied to the SCOS, both the known voltage and the results from the SCOS are captured and recorded by the oscilloscope. Figure 5-15 shows both recorded signals. The voltage that corresponds to an electric field of $1\frac{V}{m}$ is given by,

$$V = d\frac{A_{scos}}{A_{fgen}}, \quad [5\text{-}3]$$

where A_{fgen} is the amplitude of the sinusoidal source voltage, A_{scos} is the amplitude of the SCOS measurements, and d is the separation of the electrodes or rails in meters.

5.3.4 SCOS Data Mining

Another area in which I have helped improve the measurements has been in the area of data mining. I have developed several MATLAB objects, included in Appendix C, which enable quick and easy generation of useful plots from raw data. These objects take the data and apply specified filters. The filters applied have come from an increased understanding of the expected field. The expected field bounds the majority of its spectral content between $100Hz$ and $10kHz$. This knowledge has allowed us to reduce the noise so prevalent in oscilloscope captures, thereby increasing the SNR for an improved chance at seeing the electric field.

Figure 5-26 shows three plots that employ different filters. The top plot is the original unfiltered data. At first glance the presence of high frequency noise is obvious. Since the expected electric field has very little spectral information above $10kHz$, a low pass filter

positioned at that point will help reduce the high frequency noise. The middle plot shows the effect of a low pass filter on the data.

After further examination of the data, the low pass filter is modified to be a band pass filter with a low corner of $100Hz$ while maintaining the previous high corner cutoff of $10kHz$. The bottom plot in Figure 5-26 shows the effects that the band pass filter had on the signal.

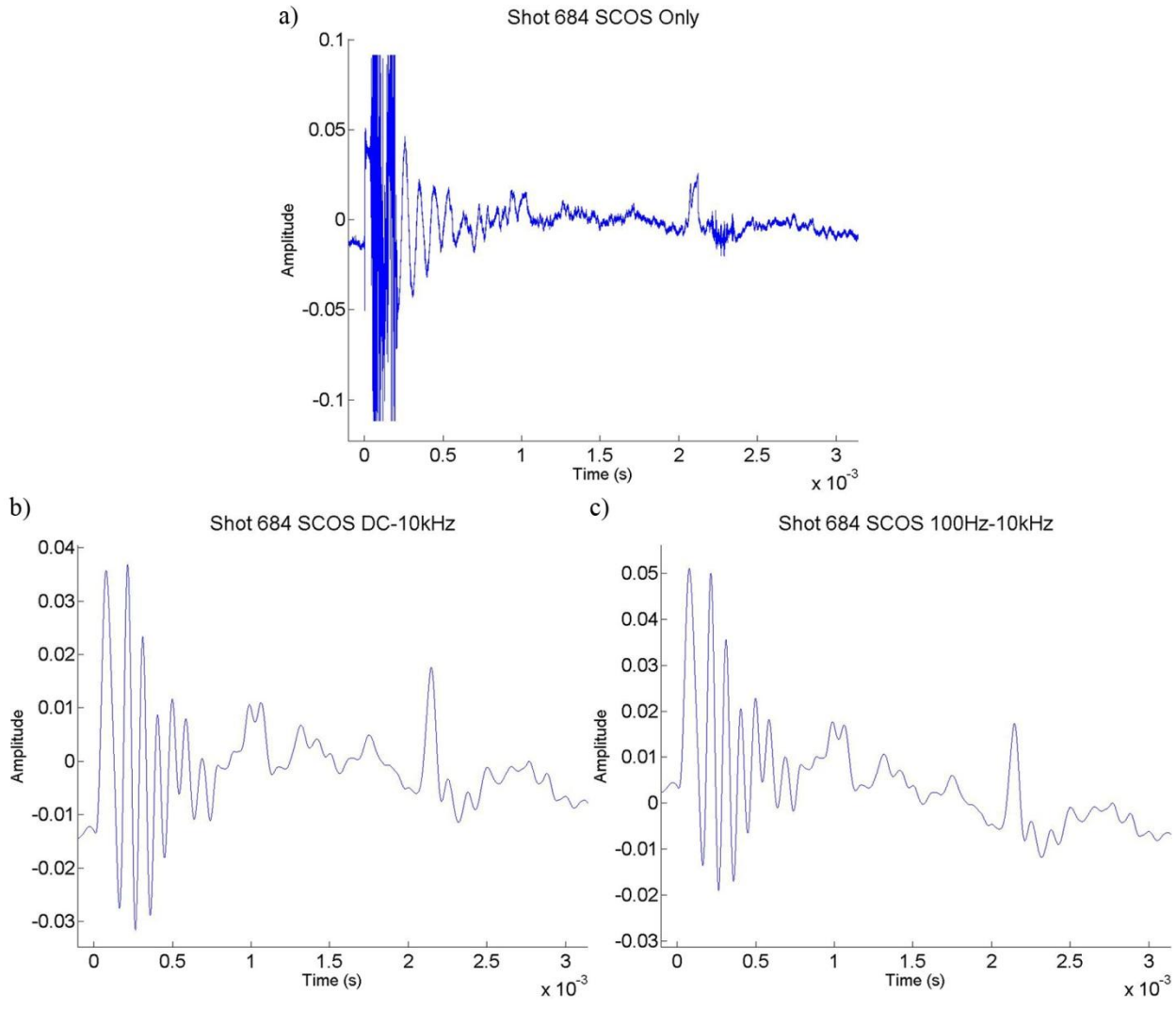

Figure 5-26: Three plots of the same shot using different filters to retrieve data.

Additionally, these MATLAB objects can also add useful information to the plot, such as electric field levels. They get the required data by automatically analyzing the relevant calibration data set files and calculating the field strength. They also have the ability to analyze the current profile and compare it to the B-Dots in order to achieve an idea of when the armature passes the sensor and when it leaves the gun. Figure 5-27 shows the annotations applied by these scripts including: armature timing and field strength levels.

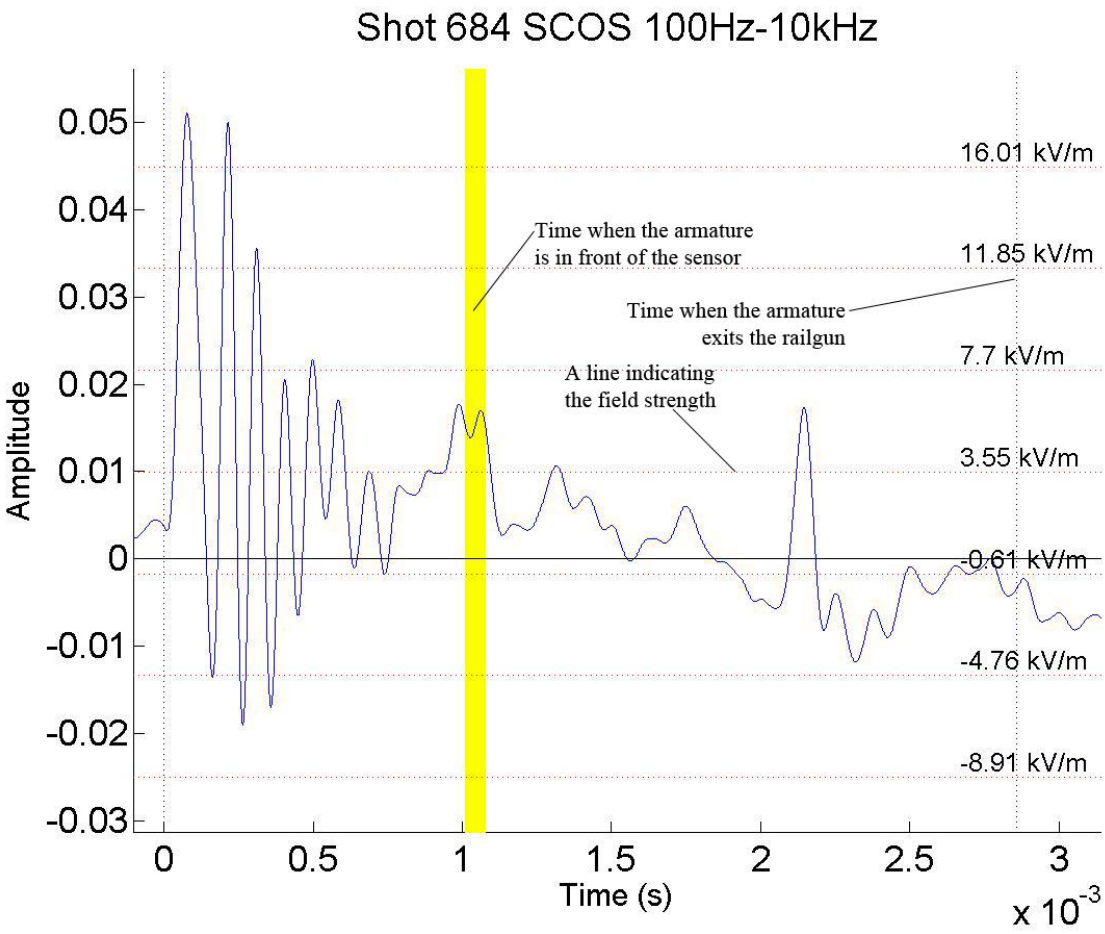

Figure 5-27: SCOS response with useful information about the armature times and field strengths.

6 CONCLUSION

There are quite a few advantages to using a railgun as a deployable weapon in war. Additionally, there are many applications beyond warfare for railgun technology. Unfortunately, the VSE causes modern railguns to be unreliable after a limited number of shots. The detection of the VSE within a railgun creates an interesting problem where a dielectric electric field sensor is required. The SCOS are suitable electric field sensors, which theoretically can be used to detect the desired electric fields without perturbing the field.

The actual usage of the SCOS within the railgun produces an additional set of challenges that are not encountered in the lab. The chief amongst these is noise from strain. The strain can be reduced by using proper mounting techniques. Moreover, the proper use of a DC block also helps increase the smallest detectable signal and with additional filtering it is possible to gather electric field strengths from an oscilloscope.

6.1 Contributions

6.1.1 Noise Characterization

One of my chief contributions to this project has been advancing our understanding of the noise in the SCOS sensing system and methods for reducing it.

6.1.2 Oscilloscope Capture

As part of my work on this project I have advanced the use of the oscilloscope over the electrical spectrum analyzer. I have done this by introducing the use of the DC block which allows for a greater amplification of the signal by existing amplifiers. Additionally, I began filtering the resulting oscilloscope capture to better retrieve the desired signal.

6.1.3 SCOS Packaging and Mounting

SCOS packaging and mounting has significantly improved during my tenure on this project. I have changed the SCOS packaging and mounting significantly such that instead of being mounted into the railgun without possibility of removal or alteration the SCOS is now mounted by means of easy to use cartridges. The cartridges also provide an excellent tool for reducing the noise pickup.

6.1.4 SCOS Calibration

Prior to my work with wavelength calibration, all wavelength calibrations were done by hand. Using the tools that I developed the wavelength calibration is now an automated hands-off procedure.

Not only did I automate the wavelength calibration, but I helped pioneer the calibration of the oscilloscope readings of the SCOS. By correctly calibrating the voltage beforehand, we are able to determine the exact field strength of the sensed electric field given the readings off of the oscilloscope.

6.1.5 SCOS Data Mining

As mentioned in a previous section, band limiting the SCOS signal response leads to a greater ability to detect the desired field. Using data provided by Lawrence Livermore National Laboratory, I was able to discover that for the railgun the majority of the desired field lies in the frequency band between 100Hz and 10kHz. Knowing this, filters can be used to reduce extraneous noise and improve the chance of detecting the electric field.

6.2 Future Work

There are several areas in which future work for sensing the VSE on a railgun should be concentrated in order to meet the desired objectives.

6.2.1 X-Cut SCOS

Tests have shown that while Polymer SCOS is quite sensitive to electric field, it is also quite sensitive to temperature, optical power, and strain. Preliminary work with X-Cut KTP SCOS shows that it has the potential to be almost as sensitive as the Polymer SCOS to electric field while being less sensitive to other noise effects.

6.2.2 SCOS Cartridges

Unfortunately at the time of writing, we have been unable to confidently measure an electric field on a railgun. More work is still required to perfect a cartridge that will minimize the strain on the SCOS while it is in the rail gun. We believe that minimizing the strain pickup on the SCOS will allow future test to accurately detect the electric field.

6.2.3 Calibration

The Labview calibration program that currently is used to calibrate the wavelength could also be expanded to simultaneously calibrate the electric field amplitude.

A new set of electrodes will need to be made to allow for the effective calibration of X-Cut SCOS in addition to the traditional Z-Cut sensors. The new electrodes should have the added benefit of being more rugged and portable in the field as well as being able to adapt to a variety of packaging configurations.

6.2.4 Data Mining

There are many options that are available for filtering data. Most frequently, I used a combination of Chebychev Type II filters and Butterworth filters. These filters, while very useful, are not always the best to use for every application. As more data is recorded and more methods are developed to sense electric fields, the types of filters used to process the data will need to be continuing evaluated and revised accordingly.

REFERENCES

[1] R. S. Gibson, "Slab coupled optical fiber sensors for electric field sensing applications," Ph.D. dissertation, Electrical Enginnering Dept., Brigham Young University, Utah, 2009.

[2] H. D. Fair, "Advances in Electromagnetic Launch Science Technology and Its Applications," *IEEE Transactions on Magnetics*, vol. 45, no. 1, pp. 225-230, January 2009.

[3] H. D. Fair, "The Science and Technology of Electric Launch," *IEEE Transactions on Megnetics*, vol. 37, pp. 25-32, January 2001.

[4] B. I. Machado, L. E. Murr, E. Martinez, S. M. Gaytan, and S. Satapathy, "Materials Characterization of Railgun Erosion Phenomena," *Materials Science and Engineering A*, pp. 7552-7559, 2011.

[5] Wikimedia Commons contributors. (2011, June) Wikimedia Commons. [Online]. http://commons.wikimedia.org/w/index.php?title=Railgun&oldid=55041471

[6] I. R. McNab and F. C. Beach, "Naval Railguns," *IEEE Transactions on Magnetics*, vol. 43, no. 1, pp. 463-468, January 2007.

[7] S. N. Rosenwasser, "Recent Advances in Large Railgun Structures and Materials Technology," *IEEE Transactions on Magnetics*, vol. 27, no. 1, pp. 444-451, January 1991.

[8] L. E. Thurmond, B. K. Ahrens, and J. P. Barber, "Measurement of the Velocity Skin Effect," *IEEE Transactions on Magnetics*, vol. 26, no. 1, pp. 326-328, January 1991.

[9] J. Solberg, "Temperature and Electric Field Mesaurement Requirements in Railguns," Lawrence Livermore National Laboratory, Presentation May 14, 2010.

[10] C. E. Baum, E. L. Breen, J. C. Giles, J. O'Neill, and G. D. Sower, "Sensors for Elecvtromagnetic Pulse Measurements Both Inside and Away from Nuclear Source Regions," *IEEE Transactions on Antennas and Propagation*, vol. 26, pp. 22-35, 1978.

[11] R. Forber, "Dielectric EM Field Probes for HPM Test & Evaluation," in *Annual ITEA Technology Review*, Cambridge, MA, 2006.

[12] S. Haishan et al., "All-Dielectric Electrooptic Sensor Based on a Polymer Microresonator Coupled Side-Polished Optical Fiber," *IEEE Sensors Journal*, vol. 7, pp. 515-524, 2007.

[13] W. C. Wang, W. Lin, H. Marshall, R. Skolnick, and D. Schaafsma, "All-dielectric miniature wideband rf receive antenna," *Optical Engineering*, vol. 43, pp. 673-677, 2004.

[14] H. Sun et al., "Broadband electric field sensor with electro-optic polymer micro-ring resonator on side-polished optical fiber," in *SPIE*, San Jose, CA, United States, 2006.

[15] S. A. Hamilton et al., "Polymer in-line fiber modulators for broadband radio-frequency optical links," *Journal of the Optical Society of America B: Optical Physics*, vol. 15, pp. 740-750, 1998.

[16] J. A. Deibel and J. F. Whitaker, "A fiber-mounted polymer electro-optic-sampling field sensor," in *2003 IEEE LEOS Annual Meeting Conference Proceedings*, Tucson, AZ, United States, 2003, pp. 786-787.

[17] A. Miller, M. C. Brierly, and S. R. Mallinson, "Exposed-core single-mode-fiber channel-dropping filter using a high index overlay waveguide," *Optics Letters*, vol. 12, pp. 284-286, 1987.

[18] K. T. Kim, D. S. Yoon, and G. I. Kwoen, "Optical properties of side-polished polarization maintaining fiber coupled with a high index planer waveguide," *Optics Communications*, vol. 230, pp. 137-144, 2004.

[19] J. Luo et al., "Recent progress in developing highly efficient and thermally stable nonlinear optical polymers for electro-optics," , San Jose, CA, 2004, pp. 36-43.

[20] S. M. Chandani and N. A. F. Jaeger, "Fiber-optic temperatuer sensor using evanescent fields in D fibers," *IEEE Photonics Thecnology Letters*, vol. 17, pp. 2706-2708, 2005.

[21] J. Noren, R. Selfridge, and S. Schultz, "Interrogation systems for slab coupled optical fiber sensors," in *Smart Sensor Phenomena, Technology, Networks, and Systems 2011*, vol. 7982, San Diego, CA, 2011.

[22] K. M. Chakravarthy, T. J. Watt, and D. L. Bourell, "The Use of High-Speed Video as an In-Bore Diagnostic for Electromagnetic Launchers," *IEEE Transactions on Plasma Science*, vol. 39, no. 2, pp. 809-814, February 2011.

APPENDIX A. RAILGUN SIMULATION, MATLAB CODE

This MATLAB script uses known parameters about a railgun to generate visual representations of the current and voltage profiles of the railgun. This script was used to generate Figure 2-4 and Figure 2-6. It is contained and explained below.

```
%% Railgun Current and Voltage Model
%% Setup Parameters

Vo=5.1e3;                    % The total voltage of the capacitor banks
R=100e-3;                    % The total resistance of the rails & armature
L=77e-6;                     % The total inductance of the rails & armature
C=8e-6;                      % The total capacitance of the rails & armature
tf = 2e-3;                   % The length of time to plot

%% Calculations
% Time field
t=linspace(0,tf,10000);

% E-Field
E=1/2*C*Vo^2;

% Decay Time Constant
tau=L/(2*R);

% Oscillation Decay frequency
w=sqrt(1/(L*C)-(R/(2*L))^2);

% Current through the rails
I=Vo/(w*L)*exp(-t/tau).*sin(w*t);

% Voltage on the rails
Vd=Vo/w*exp(-t/tau).*(w*cos(w*t)-1/tau*sin(w*t)+R/L*sin(w*t));

%% Create current with diode equivalent
% Find max current magnitude and time
df=abs(diff(sign(Vd)));
J=find(df==2);
to=interp1(Vd(J-3:J+3), t(J-3:J+3),0);
Io=interp1(Vd(J-3:J+3), I(J-3:J+3),0);
```

```
% Create decaying current plot
J=find(t>to);
J2=find(t<to);
tau2=L/R;
I2=Io*exp(-(t(J)-to)/tau);
II=[I(J2),I2];

%% Plot Figures
%Get & Setup Figure
h = figure(1);
clf;
set(gca,'FontSize',17);

% Plot current (w/ & w/o diode) & voltage
subplot(2,1,1)
hold on;
l1 = plot(t*1e3,I*1e-3);
l2 = plot(t*1e3,Vd*1e-4,'r:');
l3 = plot(t*1e3,II*1e-3,'k');
hold off;
ylabel('Current (kA), Voltage (10kV)','FontSize',15);
legend([l1,l3,l2],'Current w/o Diode','Current w/ Diode','Voltage w/o
Diode');

% Plot current only
subplot(2,1,2)
plot(t*1e3,II*1e-3)
ylabel('Current (kA)','FontSize',15);
xlabel('Time (ms)','FontSize',15);

% Save Plot
set(h, 'Position', get(0,'Screensize'));
saveas(h,['RLC_CurrentVoltagePlot.jpg'],'jpg');

%% Plot Figures
%Get & Setup Figure
h=figure(2);
clf;
set(gca,'FontSize',17);

% Plot current (w/ & w/o diode) & voltage
l1 = plot(t*1e3,I*1e-3);
ylabel('Current (kA)','FontSize',15);
xlabel('Time (ms)','FontSize',15);

% Save Plot
set(h, 'Position', get(0,'Screensize'));
saveas(h,['RLC_CurrentPlot.jpg'],'jpg');
```

APPENDIX B WAVELENGTH AUTOCALIBRATION MANUAL

B.1 Setup & First Use

In its current iteration, the auto calibration program requires some additional setup beyond the normal use of the SCOS. Use the following diagram as reference in the physical system setup.

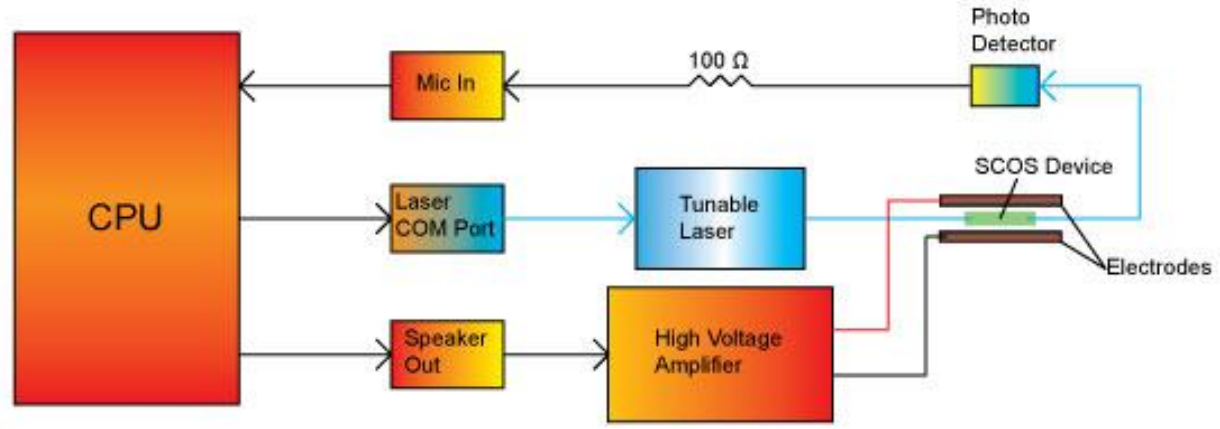

Figure B-1: A setup diagram for the auto calibration program

The *Mic In* and *Speaker Out* are both contained on the "Sound Blaster X-Fi Surround 5.1" external usb card, but the built-in speaker and microphone jack of any computer will also work. Use the provided cables, RCA to BNC to connect the speaker and microphone jacks to the rest of the system.

After the system has been physically setup, and everything has been plugged into the computer. Open the **AutoCalibration.exe** program. When the program starts up, you will be shown the **Graphs** panel as illustrated in the next section.

Click on the **Laser** tab to show the **Laser** panel. On the **Laser** panel, select the correct laser at the bottom left of the screen and then choose appropriate start/stop wavelengths as well as step size and input them in the top box of the screen.

Next, click on the **Sample** tab to show the **Sample** panel. On the **Sample** panel select correct input and output devices in the top area. If using the "Sound Blaster X-Fi Surround 5.1" external usb card, click on the number scroll until you see an item whose suffix contains *X-Fi Surround 5.1 Pro*.

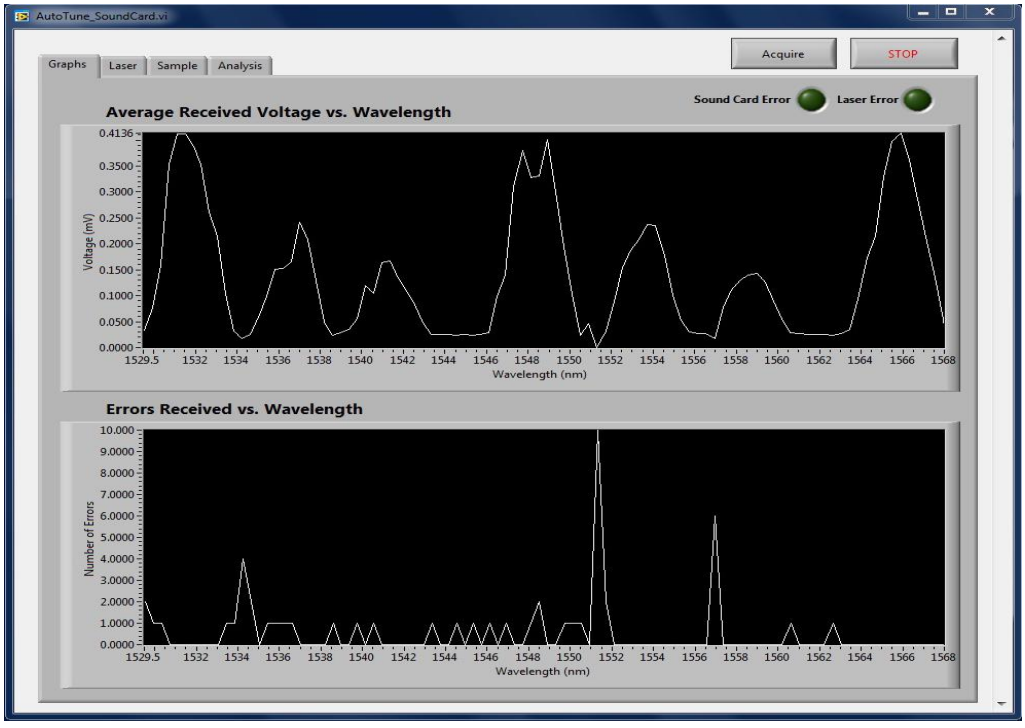

Figure B-2: The graphs panel of the auto-calibrator after a successful calibration.

After selecting the input and output device, all necessary setup steps are complete. Other items can be optionally adjusted, see the following section for more information on those items. Click the **Acquire** button, and wait. The **Graphs** panel will be updated throughout the calibration process and will allow you to see how things are going. In the end, the graphs panel should look similar to Figure B-2.

The final results will display on the **Analysis** panel.

B.2 Panels Description

B.2.1. Graphs Panel

Figure B-3: A screenshot of the graphs panel.

- **Active Panel Selector**: Allows you to select between the four control panels: **Graphs, Laser, Sample,** and **Analysis**.

- **Acquire**: This will start the calibration process. When the system is calibrating a progress bar will appear directly to the left of the **Acquire** button.
- **Stop**: This will stop the calibration process or if no calibration is currently running it will end the program.
- **Error Lights**: These indicators will light up when there is an error with the sound card or with the laser. You can go to either the **Laser**, **Sample**, or **Analysis** tabs to view more information about the errors.
- **Results Graph**: This graph shows the values of the acquired, filtered signal. Generally speaking, the wavelength that corresponds to the largest value on the graph will have the best sensitivity.
- **Errors Graph**: This graph shows how many errors are detected at each wavelength. The errors described here consist only of signal errors and does not include laser or sound card errors. Signal errors occur with the signal to noise is so low that the outgoing signal cannot be detected in the acquire sample.

B.2.1. Laser Panel

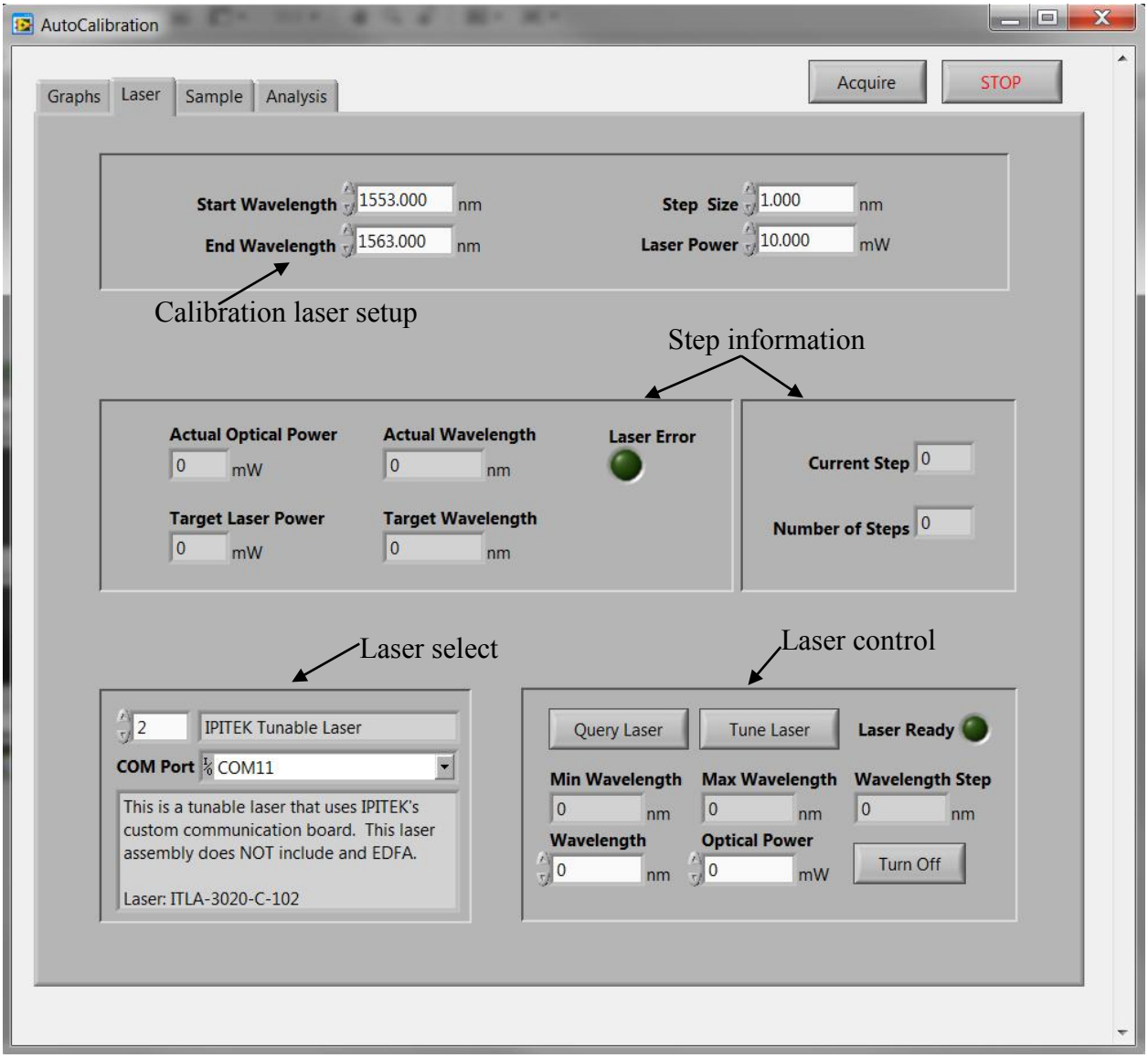

Figure B-4: A screenshot of the laser panel.

- **Calibration laser setup**: This box provides control over the start wavelength, stop wavelength, and step size of the calibration. It also provides control over the desired laser power.

- **Step information**: This box provides information on which wavelength the test is currently calibrating. It also indicates what the current step number is and how many total steps there are in the current calibration.
- **Laser Select**: Allows the user to select which laser to use by tuning the laser type number on the left. Each laser has a distinct set of drivers and so it is critical to make sure that the correct laser is selected. You must also select the correct port for communication with your laser.
- **Laser Control**: Allows the user direct control over the laser. The **Query Laser** button will send a request for information to the laser—user this button to test the connection to the laser. The **Tune Laser** button will cause the laser to tune to the wavelength and optical power specified.

B.2.3. Sample Panel

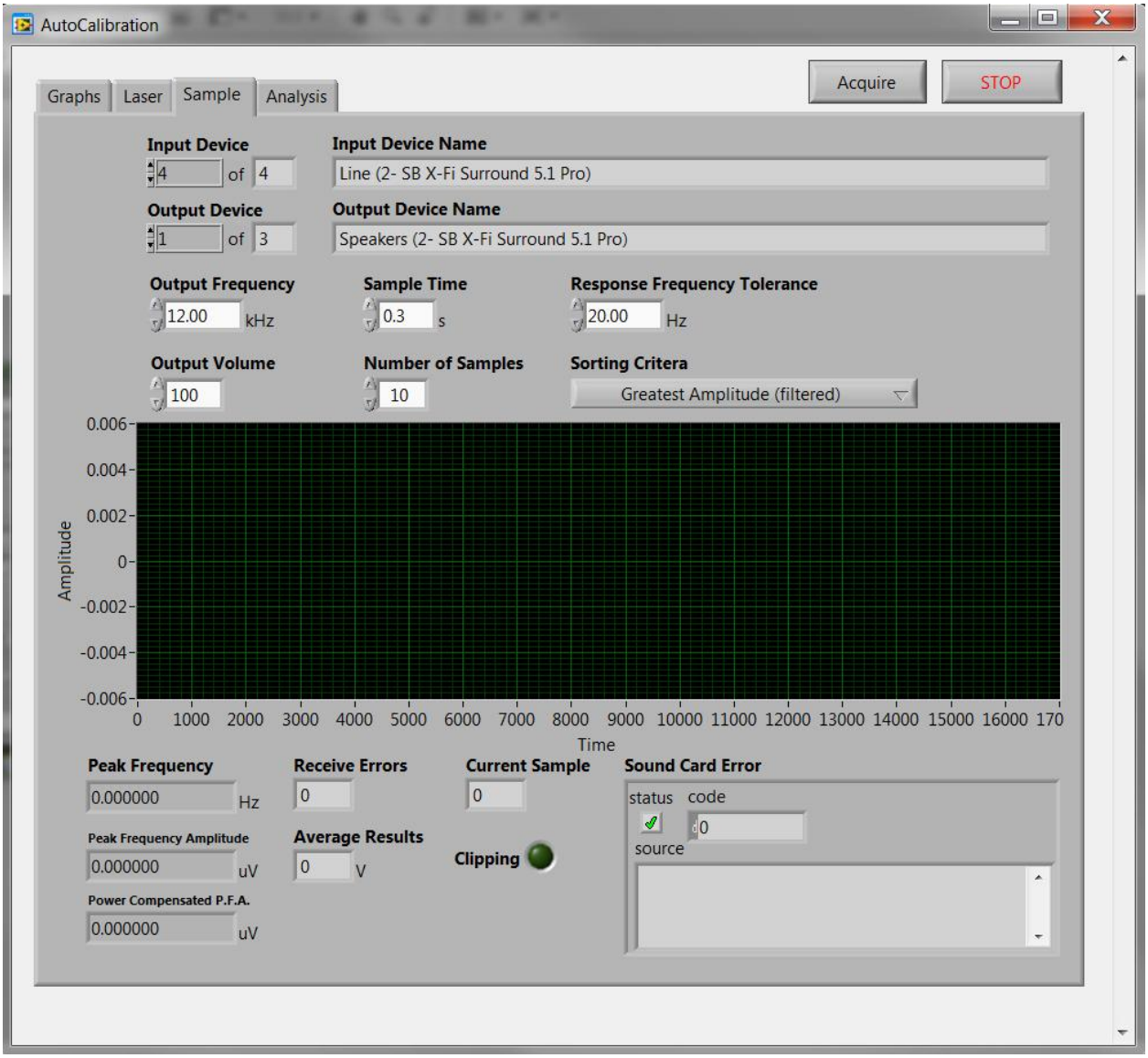

Figure B-5: A screenshot of the sample panel.

- **Input Device**: Use the number scroll to select the input device that will receive the incoming signal. The selected device name is displayed to the right. *The selected device should have as a suffix, as shown, "X-Fi Surround 5.1 Pro."*

- **Output Device:** Use the number scroll to select the output device that will receive the incoming signal. The selected device name is displayed to the right. *The selected device should have as a suffix, as shown, "X-Fi Surround 5.1 Pro."*
- **Output Frequency**: This is the frequency of the tone that will be sent to the high voltage amplifier and then applied to the SCOS. This should be much lower than the corner frequency of the high voltage amplifier.
- **Sample Time**: This is how long the system will listen for the response for each sample.
- **Response Frequency Tolerance**: In order to be counted as a valid response, the principle frequency of the filtered response must be within plus or minus this value of the target frequency.
- **Output Volume**: This value directly correlates to the amplitude of the source signal. *This value should always be at 100.*
- **Number of Samples:** The number of times each wavelength is tested. The greater this number the more accurate your calibrations will be.
- **Sorting Criteria:** There are various sorting criteria that dictate the algorithm for finding the optimal point for the SCOS. The one that should be used *always* is "Greatest Amplitude (filtered)."
- **Current Sample:** Displays which sample or test number the system is on. Each wavelength tested starts over at 0 on this value.
- **Receive Errors:** Displays how many tests for the current wavelength have resulted in an error due to the selected source frequency not being found in the return signal.
- **Sound Card Error:** Gives more information about whatever error may occur while trying to use the sound card to generate and receive signals.

B.2.3. Analysis Panel

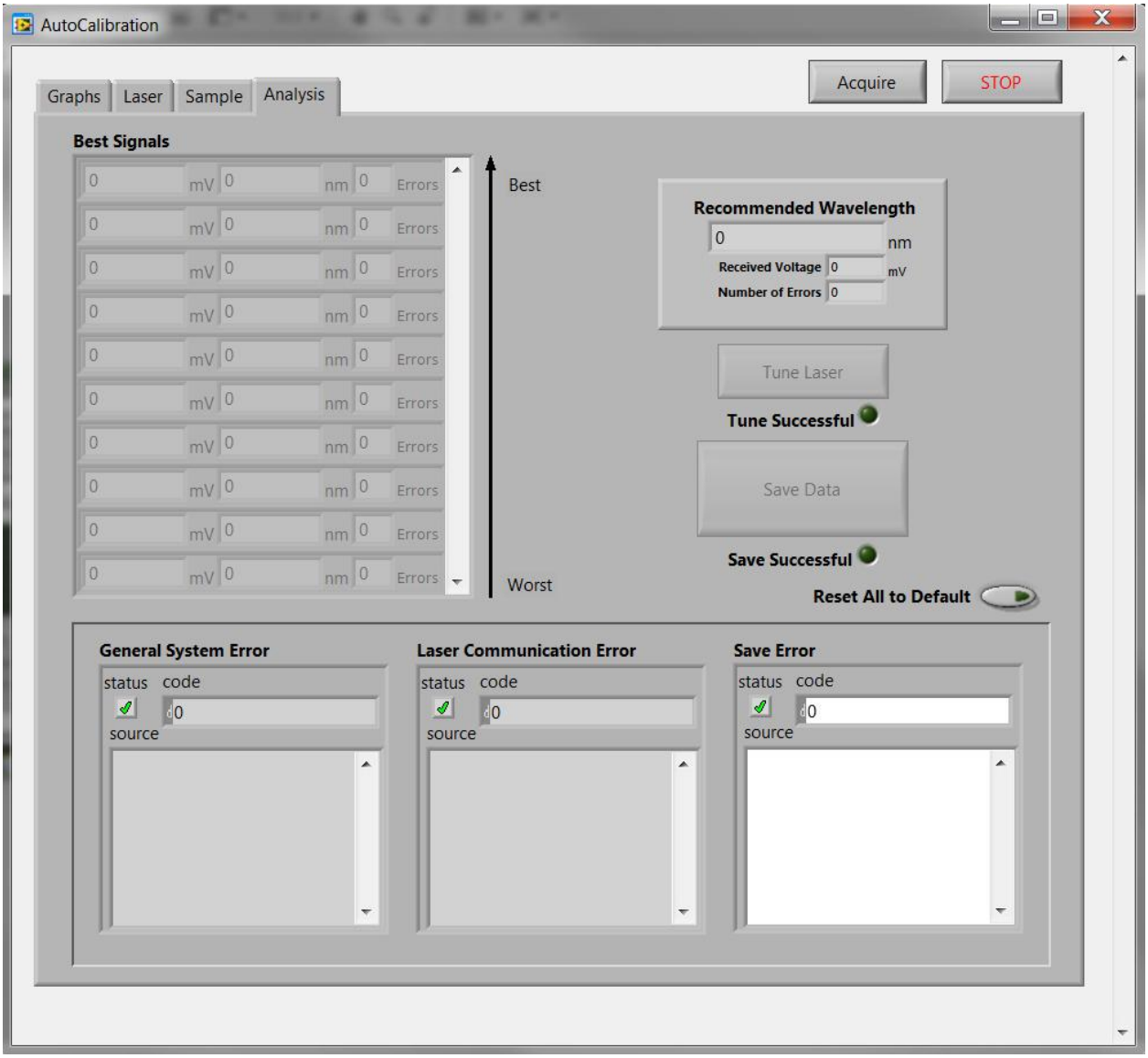

Figure B-6: A screenshot of the analysis panel.

- **Best Signals:** Displays the top 10 SCOS wavelengths that have been discovered in the calibration thus far. The top value from this area when the calibration is finished is the recommended wavelength for using the SCOS.

- **Recommended Wavelength:** This box displays the optimal SCOS wavelength discovered thus far in the current calibration, or if no calibration is currently running, it displays the optimal SCOS wavelength discovered in the last calibration.
- **Tune Laser:** After a calibration is complete and an optimal SCOS wavelength is found, this will allow you to tune the laser directly to that wavelength at the highest laser power.
- **Save Data:** This button allows you to save the list of the best SCOS signals and the recommended wavelength to a file in a comma separated format. *Make sure to include the fill suffix of ".csv" when selecting the name by which to save the file so that it opens properly with your spreadsheet program (Excel).*
- **Error Boxes:** Gives more information about whatever error may occur while trying to use the auto calibration program.

APPENDIX C. E-FIELD MAPPING, MATLAB CODE

This MATLAB script uses known parameters about a railgun shot to generate visual representations of the collected SCOS, FBG, laser tap, and armature data. Among others plots this script was used to generate Figure 5-21, Figure 5-26, and Figure 5-27. It is contained and explained in the following subsection.

C.1 Plot Formatted Data

This is the MATLAB script that ties all of the rest together. This script calls the other supporting objects as necessary to plot the formatted, filtered data. It has a great deal of flexibility including allowing you to queue a series of shots for processing.

```
%% plotData
%% Header
%   This matlab file will take a shot number and plot the
%   data measured from the shot. It will use the shot calibration
%   information to mark the field strength values. It will also
%   highlight the portion of the shot that corresponds to when
%   the projectile in the rail gun passed the sensor.
%% Setup
close all;
clear all;
clc;
%% Declarations
railgun.rail_seperation = 14e-3;    %14 mm
railgun.armature_length = 36.7e-3;  %36.7 mm
railgun.gun_length = 1.5;           %1.5 meters
file_info = 'ShotInfo.xlsx';        %Specifies the data file
file_bdot = 'BDOT_Data.xlsx';
data_folder = 'data/';              %Specifies the data directory
```

```
shot.channel = 'SCOS';              %Specify the channel that should be referenced
shot.channel_fbg = 'FBG';           %Specify the channel that FBG that should be referenced
shot.channel_laser = '10% tap';     %Specify the channel that tap that should be referenced

suffix = '_100Hz-10kHz';            %Specify the suffix for saving the file
shot_numbers = 684:684;             %Specify range of shot numbers

doSave = true;                      %Shot the shots be saved?

% Needed for Labels
if(ischar(shot.channel))
   shot.channel_txt = shot.channel;
else
   shot.channel_txt = ['CH' num2str(shot.channel)];
end

sa = SpectrumAnalysis;              %Object used to parse files
                                    %and store information as vectors

%% Load Reference Files

%   The BDot function will return an object that contains
%   the information from the BDot Excel file passed as the
%   parameter. This information gives the time at which
%   the armature passed certain locations on the rail gun
%   for a specific shot.
%   We need this information to calculate the speed and
%   acceleration of the armature so we can determine the
%   time at which it passed the SCOS sensor.
bdot = BDot(file_bdot);

%   The ParseShotInfo function iterates through the ShotInfo
%   Excel file passed as the parameter. This file has
%   information about the shot number, the time of shot,
%   the laser wavelength, the amplfier gain, the OScope
%   channel, the calibration file names, the sensor distance,
%   the sensor type, and other information about the SCOS device
%   used in the specific shot.
%   We need this information to calculate when the armature
%   passed the sensor. We will also use the information to
%   link shot data with calibration data so we can calculate
%   the strength of the electric fields.
%   The ParseShotInfo file has all information related to
%   the given shot..
shotinfo = ParseShotInfo(file_info);

%% Select the channel number

%   The rest of the code is included in this for loop and each
%   calculation is performed for every shot number given in the
%   Declarations section.

for shot_number = shot_numbers      %Iterates through every shot
%   The following line intentionally omits the semicolon ';'
%   in order to display in the command window the shot that
%   is currently being processed. It takes a while to work
```

```
%   through any given shot.
shot.number = shot_number          %Specifies shot number
%% Get Data

%   shotinfo.loadData() can be found in ParseShotInfo.m

%   'info' will contain information about any errors that
%   occured while gathering the data.

%   'data' is a struct that contains an X-vector and a Y-vector
%   with the information that the SCOS device measured
%   for a given shot and channel. (The channel is calculated
%   in ParseShotInfo in the Load Reference Files section.)
%   The X-Vector contains the time and the Y-Vector contains
%   the amplitude of the field the SCOS detected.
try
   data = shotinfo.loadData(data_folder, shot.number, shot.channel, '_bkup');
catch info
   continue;   %Start over with next shot if no shot data available.
end

%   laser is a struct that contains information about what we
%   measured as the output of the laser. We will use the
%   information to compensate for fluctuations in laser power
%   that would otherwise be read as field if we looked at
%   just the SCOS sensor.
try
   laser = shotinfo.loadData(data_folder, shot.number, shot.channel_laser, '_bkup');
catch info
   laser.x = zeros(10,1);  %If there is an error, we need to have dummy
   laser.y = zeros(10,1);  %information for the program to function.
end

%   fbg is a struct that contains information about what we
%   measured using the Fiber Bragg Grating. Both the SCOS device
%   and the FBG measure strain. However, only the SCOS measures
%   electric field. By subtracting the strain measurement obtained
%   using the FBG from the combined strain/field measurement
%   obtained using the SCOS, we will get a more accurate field
%   reading.
try
   fbg = shotinfo.loadData(data_folder, shot.number, shot.channel_fbg, '_bkup');
catch info
   fbg.x = zeros(10,1);    %If there is an error, we need to have dummy
   fbg.y = zeros(10,1);    %information for the program to function.
end


%% Center the data (along y-axis)

data.y = data.y - mean(data.y);
fbg.y = fbg.y - mean(fbg.y);
laser.y = laser.y - mean(laser.y);

%% Get Calibration information
```

```
%   This finds the correct calibration data. The parameters come from
%   the reference file (shotinfo) obtained previously. The shotinfo
%   struct has the names of the correct calibration files that can
%   be used to determine the field strength. In the calibration test,
%   a known sinusoidal voltage is applied across the rails. We divide
%   this by the distance across the rails to find the field strenght.
%   The calibration test is done using the same SCOS as will be used in
%   the shot, and allows us to measure the relationship between a shift
%   in the SCOS spectrum and the strength of the field.
CalibFGenFile = [data_folder '/' strrep(shotinfo.getAttribute('Calibration File FGen', shot.number,
                                shot.channel),'.isf','.mat')];
CalibSCOSFile = [data_folder '/' strrep(shotinfo.getAttribute('Calibration File SCOS', shot.number,
                                shot.channel),'.isf','.mat')];
calib = CalibrateSCOS(CalibSCOSFile, CalibFGenFile, shotinfo.getAttribute('Calibration FGen Gain', shot.number,
                                shot.channel), railgun.rail_seperation);

%   This calculates where the 1 kV/m field line as a function of
%   the SCOS sensitivity.
one_kV = calib.getV(1);

%% Get information on where the projectile is

%   This uses the reference files (bdot and shotinfo) obtained
%   earlier to calculate the location of the projectile. The BDOT
%   information tells the time at which the projectile passed
%   a certain marker, as well as the distance the projectile
%   travelled from time=0 to that marker. Using this data we can
%   interpolate the position of the armature at any time. As a
%   result, we can calculate when we expect the projectile to
%   pass the SCOS device, and keep that information to plot on
%   the SCOS graphs. We expect to see a peak in the electric
%   field as the armature passes the SCOS detector.

%load current profile
CurrentDataFile = [data_folder '/' strrep(shotinfo.getAttribute('Current Data', shot.number,
                                shot.channel),'.isf','.mat')];
armature = Armature(CurrentDataFile, bdot.getBDotStruct(shot.number), railgun.armature_length);

%get when the armature is passing the sensor
t = armature.getSensorWindow(.0254*shotinfo.getAttribute('Sensor Distance (in)', shot.number, shot.channel));
pass.start = t(1);
pass.end = t(2);
exit_time = armature.getTime(railgun.gun_length);

%% Data Processing
% Use only if you have 4 GB RAM or more on your system
%   This applies the lowpass and highpass filters that we need to clean up
%   the data.


% data.y = sa.cheby2_bandpass(data.x, data.y, 2, 30, 10, 5e3);
% laser.y = sa.cheby2_bandpass(laser.x, laser.y, 2, 30, 10, 5e3);
% fbg.y = sa.cheby2_bandpass(fbg.x, fbg.y, 2, 30, 10, 5e3);

% data.y = sa.cheby2_lowpass(data.x, data.y, 2, 25, 10e3);
% data.y = sa.butter_lowpass(data.x, data.y, 4, 10e3);
```

```
% data.y = sa.butter_highpass(data.x, data.y, 2, 100);
% laser.y = sa.cheby2_lowpass(laser.x, laser.y, 2, 30, 5e3);
% fbg.y = sa.cheby2_lowpass(fbg.x, fbg.y, 2, 30, 5e3);

%% Prepare & Data

%   This scales the laser data and the fbg data to fit the
%   graph windows defined by the SCOS data.

factor_laser = max(data.y)/max(laser.y);
factor_fbg = max(data.y)/max(fbg.y);
laser.y = factor_laser*laser.y;
fbg.y = factor_fbg*fbg.y;


%Calculate the window area
window.x.min = -0.1e-3;
window.x.max = exit_time*1.1;
window.y.min = min([min(data.y(data.x>=window.x.min & data.x<=window.x.max))
                    min(laser.y(laser.x>=window.x.min & laser.x<=window.x.max))
                    min(fbg.y(fbg.x>=window.x.min & fbg.x<=window.x.max))])*1.1;
window.y.max = max([max(data.y(data.x>=window.x.min & data.x<=window.x.max))
                    max(laser.y(laser.x>=window.x.min & laser.x<=window.x.max))
                    max(fbg.y(fbg.x>=window.x.min & fbg.x<=window.x.max))])*1.1;

%Select only the data that fits in the window area
data.y = data.y(data.x>=window.x.min & data.x<=window.x.max);
data.x = data.x(data.x>=window.x.min & data.x<=window.x.max);
laser.y = laser.y(laser.x>=window.x.min & laser.x<=window.x.max);
laser.x = laser.x(laser.x>=window.x.min & laser.x<=window.x.max);
fbg.y = fbg.y(fbg.x>=window.x.min & fbg.x<=window.x.max);
fbg.x = fbg.x(fbg.x>=window.x.min & fbg.x<=window.x.max);

%Create a horizontal line that maps to a 1 kV/m strength field
%for easy comparison.
one_kV_array = ones(length(data.x),1)*one_kV;

%% Plot
%Before we plot the actual shot data, we want to highlight the
%area of interest as well as plot the field strength reference
%lines. We want to plot these first so that they will be 'under'
%the actual data we plot.

%Set up figure
h = figure();
hold on;

%Highlight area of interest
pass.time = linspace(pass.start, pass.end, 3e2);
for i = 1:length(pass.time)
   plot([pass.time(i),pass.time(i)],[window.y.min,window.y.max],'y');
end

%Mark the time the projectile starts moving and leaves the gun
plot([0,0],[window.y.min, window.y.max],'k:');
plot([exit_time, exit_time],[window.y.min,window.y.max],'k:');
```

```
%Plot actual shot data
plot(fbg.x, fbg.y,'m');
plot(laser.x, laser.y,'r');
plot(data.x,data.y,'b');

%Plot Field Strength Reference Lines
plot(data.x,one_kV_array*0,'k');
rel_str = round(calib.getKV(linspace(window.y.min*.8,window.y.max*.8,7))*100)/100;
for i = 1:length(rel_str)
   plot(data.x,one_kV_array*rel_str(i),'r:');
   text(window.x.max*.85,one_kV*rel_str(i),[num2str(rel_str(i)) ' kV/m'],...
            'VerticalAlignment','Bottom','FontSize',12);
end

hold off;
axis([window.x.min window.x.max window.y.min window.y.max]); %Zoom into first 5 ms of shot

%formatting
set(gca,'FontSize',17);
title(['Shot ' num2str(shot.number) ' ' shot.channel_txt '' strrep(suffix,'_',' ')],'FontSize',18);
%ylabel({'Amplitude';['(Laser: ' num2str(round(factor_laser*100)/100) 'x; FBG: '
                              num2str(round(factor_fbg*100)/100) 'x)']},'FontSize',15);
ylabel({'Amplitude'},'FontSize',15);
xlabel('Time (s)','FontSize',15);

%Save Plot (if desired)
if(doSave)
   set(h, 'Position', get(0,'Screensize'));
   saveas(h,['plots/CalibratedShot' num2str(shot.number) '_' shot.channel_txt '' suffix '.jpg'],'jpg');
end;
if(doSave && length(shot_numbers)>1)
   close(h);
end;

end;
```

C.2 Armature Analysis

This is the MATLAB class that is responsible for analyzing the given B-Dot and current profiles and calculating where the armature is located at every point in time.

```
classdef Armature
   properties (Constant = false)
      armatureLength = 20e-3;
      time = zeros(0);
      velocity = zeros(0);
      position = zeros(0);
      acceleration = zeros(0);
```

```
        current = zeros(0);
    end

    methods (Static = false)
        function obj = Armature(CurrentDataFile, BDotDataStruct, armatureLength)
            % Armature Length
            obj.armatureLength = armatureLength;
            % Load Data
            data = csvread(CurrentDataFile, 1, 0);
            obj.time = data(:,1)/1e6;
            obj.current = data(:,2);

            % Get time information
            N = length(obj.time);
            h = (obj.time(end)-obj.time(1))/N; %Delta t

            % Calculate the acceleration
            obj.acceleration = obj.current.^2; %Acceleration

            % Calculate the velocity
            obj.velocity = zeros(N,1);
            for k=1:N
                obj.velocity(k) = sum(obj.acceleration(1:k))*h;
            end

            % Calculate the position
            obj.position = zeros(N,1);
            for k=1:N
                obj.position(k) = sum(obj.velocity(1:k))*h;
            end

            % Adjust for the BDot info
            bdotx = BDotDataStruct.t;
            bdoty = BDotDataStruct.x;

            ci = [find(obj.time>=bdotx(1),1) find(obj.time>=bdotx(2),1) find(obj.time>=bdotx(3),1)];
            cv = mean([(bdoty(1)/obj.position(ci(1))) (bdoty(2)/obj.position(ci(2))) (bdoty(3)/obj.position(ci(3)))]);
            obj.position = obj.position*cv;

        end
        function [times] = getSensorWindow(obj, sensorLocation)
            pos = [sensorLocation, sensorLocation + obj.armatureLength];
            times = interp1(obj.position,obj.time,pos,'spline');
        end
        function [times] = getTime(obj, location)
            times = interp1(obj.position,obj.time,location,'spline');
        end
    end
end
```

C.3 SCOS Voltage Calibration

This is the MATLAB class that is responsible for analyzing the given calibration data and calculating the voltage level that corresponds with a 1kV/m field. With this information, any arbitrary field level can be calculated and returned by this class.

```
classdef CalibrateSCOS
   properties (Constant = false)
      fgen = cell(0);
      scos = cell(0);
      stat = cell(0);
      one_kV = 0;
   end

   methods (Static = false)
      function obj = CalibrateSCOS(SCOS_filename, FGen_filename, FGen_Gain, Rail_Seperation)
         scos = load(SCOS_filename);
         fgen = load(FGen_filename);

         %Collect some data stats
         obj.stat.t.min = scos.x(1);
         obj.stat.t.min = scos.x(end);
         obj.stat.t.sampling_rate = 1/(scos.x(2) - scos.x(1));
         obj.stat.t.points = length(scos.x);
         obj.stat.FGen_Gain = FGen_Gain;
         obj.stat.Rail_Seperation = Rail_Seperation;

         %Make guesses
         amp = max(fgen.y);
         y_shift = 0;
         t_shift = 0;
         freq = obj.guessFreq(fgen.x, fgen.y);

         %Get time shift
         err_fit_T_fgen = @(N) obj.fit_TimeShift(fgen.x, fgen.y, freq, amp, y_shift, N);
         [data] = fminsearch(err_fit_T_fgen,[t_shift]);
         t_shift = data(1);

         %Correct Frequency
         err_fit_F_fgen = @(N) obj.fit_Frequency(fgen.x, fgen.y, y_shift, t_shift, amp, N);
         [data] = fminsearch(err_fit_F_fgen,[freq]);
         freq = data(1);

         %Get amplitude and shift
         err_fit_Y_fgen = @(N) obj.fit_Y(fgen.x, fgen.y, freq, t_shift, N);
         [data] = fminsearch(err_fit_Y_fgen,[amp y_shift]);
         amp = data(1);
         y_shift = data(2);

         %Pack FGen Data
```

```
        obj.fgen.amplitude = abs(amp);
        obj.fgen.shift.y = y_shift;
        obj.fgen.shift.t = t_shift;
        obj.fgen.frequency = freq;

        %Get amplitude and shift of SCOS
        err_fit_Y_scos = @(N) obj.fit_Y(scos.x, scos.y, freq, t_shift, N);
        [data] = fminsearch(err_fit_Y_scos,[amp y_shift]);
        amp = data(1);
        y_shift = data(2);

        %Pack SCOS Data
        obj.scos.amplitude = abs(amp);
        obj.scos.shift.y = y_shift;
        obj.scos.shift.t = t_shift;
        obj.scos.frequency = freq;

        %Figure out what level 1KV is
        obj.one_kV = obj.scos.amplitude/(obj.fgen.amplitude*FGen_Gain/(Rail_Seperation*1e3));
    end
    function V = getV(obj,kV)
        V = obj.one_kV*kV;
    end
    function kV = getKV(obj,V)
        kV = V/obj.one_kV;
    end
    function [x,y] = getPlotDataSCOS(obj,x)
        y=obj.scos.shift.y+obj.scos.amplitude*sin(2*pi*obj.scos.frequency*(x+obj.scos.shift.t));
    end
    function [x,y] = getPlotDataFGen(obj,x)
        y=obj.fgen.shift.y+obj.fgen.amplitude*sin(2*pi*obj.fgen.frequency*(x+obj.fgen.shift.t));
    end
end
methods (Static = true)
    function freq = guessFreq(x,y)
        %block DC
        y = y - mean(y);

        %guess frequency
         Fs = 1/(x(2) - x(1));
         Hs = spectrum.periodogram;
         hpsd = psd(Hs, y, 'Fs',Fs);
         [~,I]= max(hpsd.Data);
         freq = hpsd.frequencies(I);
    end
    function err=fit_Y(x,y,f,t_shift,N)
        amp=N(1); %amplitude
        y_shift=N(2); %y off-set

        val=y_shift+amp*sin(2*pi*f*(x+t_shift));

        err=sum(abs(val-y));
    end
    function err=fit_Frequency(x, y, y_shift, t_shift, amp, N)
        f=N; %frequency;
```

```
        val=y_shift+amp*sin(2*pi*f*(x+t_shift));

        err=sum(abs(val-y));
      end
      function err=fit_TimeShift(x, y, f, amp, y_shift, N)
        t_shift=N; %t off-set

        val=y_shift+amp*sin(2*pi*f*(x+t_shift));

        err=sum(abs(val-y));
      end
   end
end
```

C.4 Data Filter and Loading

This MATLAB class contains a series of static functions that allow the easy loading and filtering of data using a variety of different methods.

```
classdef SpectrumAnalysis
   properties (Constant = true)
      colors = {'b' 'g' 'r' 'c' 'y' 'k'};
   end
   methods (Static = true)
      function [X,Y] = loadOSFile(f)
         filename = f;
         M = dlmread(filename,'\t', 9,0);
         Y = M(:,2);
         X = M(:,3);
      end
      function [X,Y] = loadTOSFile(f)
         filename = f;
         M = dlmread(filename,',', 8,0);
         Y = M(:,5);
         X = M(:,4);
      end
      function [X,Y] = loadLOSFile(f)
         filename = f;
         M = dlmread(filename,' ', 0,0);
         Y = M(:,2);
         X = M(:,1);
      end
      function [X,Y] = loadSAFile(f)
         filename = f;
         M = dlmread(filename,',', [3,0,1001,1]);
         X = M(:,1) .* 1e-9;
         Y = M(:,2);
      end
      function [X,Y] = loadPCFile(f)
```

```
    filename = f;
    M = dlmread(filename,'\t', 14,0);
    Y = M(:,2);
    X = M(:,1);
end
function [X,Y,fs,h] = plotSpectrum(x, y, fig, graphTitle)
    ofig = gcf;
    h = 0;
    Fs = 1/(x(2) - x(1));
    Hs = spectrum.periodogram;
    hpsd = psd(Hs, y, 'Fs',Fs);
    X = hpsd.frequencies;
    Y = hpsd.Data;
    fs = hpsd.Fs;
    if fig >= 0
        if(exist('fig','var') ~= 0 && fig > 0)
            h = figure(fig);
        else
            h = figure();
        end;
        %clf;
        plot(hpsd);
        if(exist('graphTitle','var') == 1)
            title(graphTitle);
        end
        if(exist('fig','var') ~= 0 && fig > 0)
            figure(ofig);
        end;
    end;
end
function [X,Y,fs,h] = plotSpectrumFFT(x, y, fig, graphTitle)
    ofig = gcf;
    h = 0;
    fs = 1/(x(2) - x(1));
    L = length(y);
    NFFT = 2^nextpow2(L); % Next power of 2 from length of y
    Y = fft(y,NFFT)/L;
    X = fs/2*linspace(0,1,NFFT/2+1);

    if fig >= 0
        if(exist('fig','var') ~= 0 && fig > 0)
            h = figure(fig);
        else
            h = figure();
        end;
        clf;
        plot(X,20.*log(abs(Y(1:NFFT/2+1))));
        xlabel('Frequency (Hz)','FontSize',15);
        ylabel('Power (dB)','FontSize',15);
        if(exist('graphTitle','var') == 1)
            set(gca,'FontSize',17);
            title(graphTitle);
        end
        if(exist('fig','var') ~= 0 && fig > 0)
            figure(ofig);
        end;
```

```
    end;
end
function [X,Y1,Y2,fs,h] = plotDualSpectrumFFT(x, y1, y2, fig, graphTitle)
    if(length(y1) ~= length(y2))
        error('The lengths of the two data strings must be the same.');
    end;

    ofig = gcf;
    h = 0;
    fs = 1/(x(2) - x(1));

    L = length(y1);
    NFFT1 = 2^nextpow2(L); % Next power of 2 from length of y
    Y1 = fft(y1,NFFT1)/L;

    L = length(y2);
    NFFT2 = 2^nextpow2(L); % Next power of 2 from length of y
    Y2 = fft(y2,NFFT2)/L;

    NFFT = min(NFFT1,NFFT2);
    X = fs/2*linspace(0,1,NFFT/2+1);

    if fig >= 0
        if(exist('fig','var') ~= 0 && fig > 0)
            h = figure(fig);
        else
            h = figure();
        end;
        clf;
        hold on;
        plot(X,20.*log(abs(Y1(1:NFFT/2+1))),'b');
        plot(X,20.*log(abs(Y2(1:NFFT/2+1))),'r');
        hold off;
        xlabel('Frequency (Hz)','FontSize',15);
        ylabel('Power (dB)','FontSize',15);
        if(exist('graphTitle','var') == 1)
            set(gca,'FontSize',17);
            title(graphTitle);
        end
        if(exist('fig','var') ~= 0 && fig > 0)
            figure(ofig);
        end;
    end;
end
function [W] = convertFreq(x, y, f)
    Fs = 1/(x(2) - x(1));
    Hs = spectrum.periodogram;
    hpsd = psd(Hs, y, 'Fs',Fs);
    W = f./max(hpsd.frequencies);
    for n=1:length(W)
        if W(n) >= 1
            W(n) = 1-1e-6;
        end
        if W(n) <= 0
            W(n) = 1e-6;
        end
```

```
    end
end
function [y,h] = cheby_bandstop(x, y, ord, db, f1, f2)
    [z,p,k] = cheby1(ord, db, SpectrumAnalysis.convertFreq(x,y,[f1 f2]), 'stop');
    [sos,g] = zp2sos(z,p,k);
    Hd = dfilt.df2tsos(sos,g);
    h = Hd;
    y = filter(Hd, y);
end
function [y,h] = cheby_highpass(x, y, ord, db, f)
    [z,p,k] = cheby1(ord, db, SpectrumAnalysis.convertFreq(x,y,f), 'high');
    [sos,g] = zp2sos(z,p,k);
    Hd = dfilt.df2tsos(sos,g);
    h = Hd;
    y = filter(Hd, y);
end
function [y,h] = cheby_lowpass(x, y, ord, db, f)
    [z,p,k] = cheby1(ord, db, SpectrumAnalysis.convertFreq(x,y,f), 'low');
    [sos,g] = zp2sos(z,p,k);
    Hd = dfilt.df2tsos(sos,g);
    h = Hd;
    y = filter(Hd, y);
end
function [y,h] = cheby_bandpass(x, y, ord, db, f1, f2)
    [z,p,k] = cheby1(ord, db, SpectrumAnalysis.convertFreq(x,y,[f1 f2]), 'bandpass');
    [sos,g] = zp2sos(z,p,k);
    Hd = dfilt.df2tsos(sos,g);
    h = Hd;
    y = filter(Hd, y);
end
function [y,h] = cheby2_bandstop(x, y, ord, db, f1, f2)
    [z,p,k] = cheby2(ord, db, SpectrumAnalysis.convertFreq(x,y,[f1 f2]), 'stop');
    [sos,g] = zp2sos(z,p,k);
    Hd = dfilt.df2tsos(sos,g);
    h = Hd;
    y = filter(Hd, y);
end
function [y,h] = cheby2_highpass(x, y, ord, db, f)
    [z,p,k] = cheby2(ord, db, SpectrumAnalysis.convertFreq(x,y,f), 'high');
    [sos,g] = zp2sos(z,p,k);
    Hd = dfilt.df2tsos(sos,g);
    h = Hd;
    y = filter(Hd, y);
end
function [y,h] = cheby2_lowpass(x, y, ord, db, f)
    [z,p,k] = cheby2(ord, db, SpectrumAnalysis.convertFreq(x,y,f), 'low');
    [sos,g] = zp2sos(z,p,k);
    Hd = dfilt.df2tsos(sos,g);
    h = Hd;
    y = filter(Hd, y);
end
function [y,h] = cheby2_bandpass(x, y, ord, db, f1, f2)
    [z,p,k] = cheby2(ord, db, SpectrumAnalysis.convertFreq(x,y,[f1 f2]), 'bandpass');
    [sos,g] = zp2sos(z,p,k);
    Hd = dfilt.df2tsos(sos,g);
    h = Hd;
```

```
    y = filter(Hd, y);
end
function [y,h] = butter_bandstop(x, y, ord, f1, f2)
    [z,p,k] = butter(ord,SpectrumAnalysis.convertFreq(x,y,[f1 f2]),'stop');
    [sos,g] = zp2sos(z,p,k);
    Hd = dfilt.df2tsos(sos,g);
    h = Hd;
    y = filter(Hd, y);
end
function [y,h] = butter_highpass(x, y, ord, f)
    [z,p,k] = butter(ord,SpectrumAnalysis.convertFreq(x,y,f),'high');
    [sos,g] = zp2sos(z,p,k);
    Hd = dfilt.df2tsos(sos,g);
    h = Hd;
    y = filter(Hd, y);
end
function [y,h] = butter_lowpass(x, y, ord, f)
    [z,p,k] = butter(ord,SpectrumAnalysis.convertFreq(x,y,f),'low');
    [sos,g] = zp2sos(z,p,k);
    Hd = dfilt.df2tsos(sos,g);
    h = Hd;
    y = filter(Hd, y);
end
function [y] = butter_bandpass(x, y, ord, f1, f2)
    y = SpectrumAnalysis.butter_lowpass(x,y,ord,f2);
    y = SpectrumAnalysis.butter_highpass(x,y,ord,f1);
end
function [y,h] = generic_bandstop(type, x, y, db, f1, f2)
    Fpass = f1;              % Stopband Start Frequency (Hz)
    Fstop = f2;              % Stopband Stop Frequency (Hz)
    Apass = 1;               % Passband Ripple (dB)
    Astop = db;              % Stopband Attenuation (dB)
    Fs    = 1/abs(x(1)-x(2));   % Sampling Frequency (Hz)


    h = fdesign.bandstop('Fp1,Fst1,Fst2,Fp2,Ap1,Ast,Ap2', Fpass*.95, Fpass, Fstop, Fstop*1.05, Apass, Astop,
                         Apass, Fs);

    Hd = design(h, type);
    h = Hd;
    y = filter(Hd,y);
end
function [y,h] = generic_lowpass(type, x, y, db, f)
    Fpass = .1;              % Passband Frequency (Hz)
    Fstop = f;               % Stopband Frequency (Hz)
    Apass = 1;               % Passband Ripple (dB)
    Astop = db;              % Stopband Attenuation (dB)
    Fs    = 1/abs(x(1)-x(2));   % Sampling Frequency (Hz)


    h = fdesign.lowpass('fp,fst,ap,ast', Fpass, Fstop, Apass, Astop, Fs);

    Hd = design(h, type);
    h = Hd;
    y = filter(Hd,y);
end
```

```
        function [y] = filter_movingaverage(x, y, windowSize)
            y = filter(ones(1,windowSize)/windowSize,1,y);
        end
        function [y,h] = cheby_notch(x, y, ord, Q, f)
            Fs    = 1/abs(x(1)-x(2));   % Sampling Frequency (Hz)
            d = fdesign.notch('N,F0,Q,Ap',ord, ceil(f/2)*2, Q, 1,Fs,'dB');
            h = design(d, 'cheby1');
            y = filter(h,y);
        end
    end
end
```

C.5 B-Dot Data Loader

This MATLAB class is responsible for loading the information about B-Dot times and locations from an excel file. This class expects an excel file that is formatted similarly to the excel file in Figure C-1.

	A	B	C	D	E	F	G
1		Location (mm)	Time (ms)				
2	Shot #		678	679	680	681	682
4	B-DOT2	241	0.908	0.92	1.194	0.906	0.896
5	B-DOT4	482	1.078	1.09	1.494	1.062	1.062
6	B-DOT5	540	1.16	1.178	1.63	1.148	1.144
7	B-DOT6	680	1.314	1.338	1.924	1.304	1.304
8							

Figure C-1: An example Excel file describing the B-Dot setup and times for use with the MATLAB program

```
classdef BDot
    properties (Constant = false)
        data = 0;
    end
    properties (Constant = true)
        bdots = {'B-DOT2','B-DOT5','B-DOT6'};
        col_title = 1; %This is the column where the bdot titles are located
        col_location = 2; %This is the column number where the location can be found
        row_shot = 2; %This is the row where the shot number can be found
    end
    methods (Static = false)
        function obj = BDot(BDotDataFile)
          obj.data = ParseExcel(BDotDataFile, [1,1], [0,0]);
```

```
    end
    function out = getBDotStruct(obj,shot)
      out = struct('x',zeros(length(obj.bdots),1),'t',zeros(length(obj.bdots),1));

      shot_col = obj.data.findCol(shot,obj.row_shot);

      for n = 1:length(obj.bdots)
        row = obj.data.findRow(obj.bdots{n},obj.col_title);
        out.x(n) = obj.data.getValue(obj.col_location,row)/1e3;
        out.t(n) = obj.data.getValue(shot_col,row)/1e3;
      end
    end
  end
end
```

C.6 Parse Shot Information

This MATLAB class is responsible for loading the information about the various shots including the filenames of the shot and calibration data along with other pertinent information. This class expects an excel file that is formatted similarly to the excel file in Figure C-2.

```
classdef ParseShotInfo
  properties (Constant = true)
    row_shot = 'Shot Number'; %Left hand heading in Excel file for row that contains shot info
    row_channel = 'OScope Channel';
    row_sensor = 'Sensor Type';
    row_oscopefile = 'OScope File Name';
    offset = struct('data',[2,1],'text',[1,0]);
    col_header = 1;
  end
  properties (Constant = false)
    data = cell(0);
    text = cell(0);
    cache = cell(0);
  end
  methods (Static = false)
    function obj = ParseShotInfo(filename)
      [~,sheets] = xlsfinfo(filename);
      [obj.data, obj.text, ~] = xlsread(filename,sheets{1});

      obj.cache.shot = obj.findRow(obj.row_shot,obj.col_header);
      obj.cache.channel = obj.findRow(obj.row_channel,obj.col_header);
      obj.cache.sensor = obj.findRow(obj.row_sensor,obj.col_header);
    end
    function val = findRow(obj, rowname, col)
      if(ischar(rowname))
        val = find(strcmp(obj.text(:,col-obj.offset.text(2)),rowname)==1)+obj.offset.text(1);
      else
        val = find(obj.data(:,col-obj.offset.data(2)) == rowname)+obj.offset.data(1);
```

```
        end
    end
    function val = findCol(obj, colname, row)
        if(ischar(colname))
            val = find(strcmp(obj.text(row-obj.offset.text(1),:),colname)==1)+obj.offset.text(2);
        else
            val = find(obj.data(row-obj.offset.data(1),:) == colname)+obj.offset.data(2);
        end
    end
    function val = getValue(obj, col, row)
        if(strcmp(obj.text(row-obj.offset.text(1),col-obj.offset.text(2)),''))
            val = obj.data(row-obj.offset.data(1),col-obj.offset.data(2));
        else
            val = obj.text(row-obj.offset.text(1),col-obj.offset.text(2));
            val = val{1};
        end;
    end
    function val = getAttribute(obj, key, shot, channel_sensor) %Can pass channel number or sensor type to
                                function in channel_sensor
        if(ischar(channel_sensor))
            col = obj.findCol(channel_sensor,obj.cache.sensor);
            col = intersect(obj.findCol(shot,obj.cache.shot), col)';
            if(isempty(col))
                throw(MException('Attribute:NotFound',['Unable to find the selected shot/sensor combination: '
                                num2str(shot) ', ' channel_sensor]));
            end
        else
            col = obj.findCol(channel_sensor,obj.cache.channel);
            col = intersect(obj.findCol(shot,obj.cache.shot), col)';
            if(isempty(col))
                throw(MException('Attribute:NotFound',['Unable to find the selected shot/channel combination.'
                                num2str(shot) ', ' channel_sensor]));
            end
        end
        col = col(1,1);
        row = obj.findRow(key, obj.col_header);
        val = obj.getValue(col, row);
    end
    function data = loadData(obj, data_folder, shot, channel_sensor, suffix)
        filename = [data_folder '/' strrep(obj.getAttribute(obj.row_oscopefile, shot, channel_sensor),'.isf',[suffix
                                '.mat'])];
        data = load(filename);
        data.shot = shot;
        data.filename = filename;
    end
  end
end)
```

	A	AF	AG	AH
1				
2	Date	1/20/2012	1/20/2012	1/20/2012
3	Time	9:20	9:20	9:20
4	Shot Number	690	690	690
5	Voltage Discharged (kV)	5.1	5.1	5.1
7	Sensor	Ceramic A	Ceramic A	none
8	Mounting	fishing line rubber cement to insulator	fishing line rubber cement to insulator	none
9	Sensor Type	FBG	SCOS	10% tap
10	Sensor Position	L4	L4	---
11	Sensor Distance (in)	35.25	35.25	---
13	Laser	SANTEC	IPITEK	IPITEK
14	Laser Power (mW)	---	20	20
15	Laser Wavelength (nm)	1549.218	1554.540	1554.540
16	EDFA	No	No	No
17	Return Power (uW)	---	218.0	---
19	Amplifier Gain	1000.00	1000.00	1000.00
20	Filter (L) (kHz)	0.00	1.00	1.00
21	Filter (H) (kHz)	1000.00	100.00	100.00
23	OScope Channel	3	2	1
24	OScope Time (ms/div)	4	4	4
25	OScope preTrigger (div)	1	1	1
26	OScope Voltage (mV/div)	500	200	5
27	OScope File Name	Shot690_CH3.isf	Shot690_CH2.isf	Shot690_CH1.isf
29	Calibration File SCOS	---	Calibration688_CH2.isf	---
30	Calibration File FGen	---	Calibration688_CH4.isf	---
31	Calibration File Laser	---	Calibration688_CH1.isf	---
32	Calibration FGen Gain	---	50	---
33	Calibration TIA Gain	---	1000	---
34	Calibration Filter (L) (kHz)	---	1.0	---
35	Calibration Filter (H) (kHz)	---	100	---
37	Calibration Wavelength (H) (nm)	1549.24	---	---
38	Calibration Voltage (H) (mV)	1960.00	---	---
39	Calibration Wavelength (M) (nm	1549.23	---	---
40	Calibration Voltage (M) (mV)	910.00	---	---
41	Calibration Wavelength (L) (nm)	1549.22	---	---
42	Calibration Voltage (L) (mV)	430.00	---	---
44	Current Data	Shot690_Current.csv	Shot690_Current.csv	Shot690_Current.csv
45	General Notes			

Figure C-2: An example Excel file the plotting program expects to see detailing the shot information.

C.7 Parse Microsoft Excel File

This MATLAB class is a generic tool for reading Microsoft Excel files. It compensates for the data mismatch between numeric and non-numeric values allowing the use of both seamlessly through a project.

```
classdef ParseExcel
   properties (Constant = false)
      data = cell(0);
      text = cell(0);
      offset = struct('data',[2,1],'text',[1,0]);
   end
   methods (Static = false)
      function obj = ParseExcel(filename, data_offset, text_offset)%[row, col]
         [~,sheets] = xlsfinfo(filename);
         [obj.data, obj.text, ~] = xlsread(filename,sheets{1});

         obj.offset.data = data_offset;
         obj.offset.text = text_offset;
      end
      function val = findRow(obj, rowname, col)
         if(ischar(rowname))
            val = find(strcmp(obj.text(:,col-obj.offset.text(2)),rowname)==1)+obj.offset.text(1);
         else
            val = find(obj.data(:,col-obj.offset.data(2)) == rowname)+obj.offset.data(1);
         end
      end
      function val = findCol(obj, colname, row)
         if(ischar(colname))
            val = find(strcmp(obj.text(row-obj.offset.text(1),:),colname)==1)+obj.offset.text(2);
         else
            val = find(obj.data(row-obj.offset.data(1),:) == colname)+obj.offset.data(2);
         end
      end
      function val = getValue(obj, col, row)
         if(strcmp(obj.text(row-obj.offset.text(1),col-obj.offset.text(2)),''))
            val = obj.data(row-obj.offset.data(1),col-obj.offset.data(2));
         else
            val = obj.text(row-obj.offset.text(1),col-obj.offset.text(2));
            val = val{1};
         end;
      end
   end
end
```